On the Characterization and Modeling of Interfaces in Fiber Reinforced Polymer Structures

Zur Erlangung des akademischen Grades eines
Doktors der Ingenieurwissenschaften (Dr.-Ing.)

von der KIT-Fakultät für Maschinenbau des
Karlsruher Instituts für Technologie (KIT)

angenommene
Dissertation
von

Michael Schober, M. Sc.

Tag der mündlichen Prüfung:	18. Januar 2019
Hauptreferent:	Prof. Dr. rer. nat Peter Gumbsch
Korreferenten:	PD Dr.-Ing. habil. Jörg Hohe
	Prof. Dr. Takashi Kuboki

Kurzfassung

Faserverstärkte Kunststoffe bieten insbesondere mit kontinuierlicher Faserverstärkung ein enormes Potential, um leichte und gleichzeitig steife und feste Strukturen zu erzeugen, weswegen sie in der Fahrzeugbranche in hochbelasteten Bauteilen Verwendung finden. Darüber hinaus sind im semistrukturellen Bereich auch häufig diskontinuierlich faserverstärkte Kunststoffe vorzufinden, da sie hier im Vergleich zu kontinuierlich faserverstärkten Kunststoffen, aber auch im Vergleich zu Metallen kostengünstiger herzustellen sind. Eine neue, hybride Werkstoffklasse zielt nun darauf ab, die Vorteile diskontinuierlicher mit den Vorteilen kontinuierlicher Faserverstärkung zu verbinden. Durch die Funktionalisierung kontinuierlicher Faserverbunde als hauptlasttragende Verstärkung einer diskontinuierlich langfaserverstärkten Grundstruktur lassen sich kostengünstige, aber leistungsfähige Faserverbundstrukturen herstellen. Derartige kontinuierlich-diskontinuierlich langfaserverstärkte Kunststoffe weisen verschiedenartige innere Grenzflächen auf, welche sich insbesondere auf das Versagensverhalten der Struktur auswirken. Um sichere Auslegungsverfahren für diese Werkstoffklasse entwickeln zu können, ist es daher notwendig, die inneren Grenzflächen untersuchen und beschreiben zu können.

Die vorliegende Arbeit befasst sich mit Methoden, innere Grenzflächen von Faserverbundkunststoffen zu charakterisieren und zu modellieren und wendet diese auf werkstoffklassenspezifische Materialien und Herstellungsprozesse an. Hierzu werden experimentelle Untersuchungen der

Faser-Matrix-Grenzflächen sowie der interlaminaren Grenzflächen von kontinuierlich verstärkten Schichtverbunden durchgeführt und auf die weitere Verwendbarkeit im Produktentwicklungsprozess hin untersucht. Es wird ein kombinierter experimentell-numerischer Ansatz verfolgt, um einerseits die experimentellen Ergebnisse zu validieren und andererseits eine vorteilhafte Modellierung des Materialverhaltens zu untersuchen.

Abstract

Fiber reinforced polymers and especially continuous fiber reinforced polymers feature high stiffness-to-weight and strength-to-weight ratios. Hence, they are considered promising materials for the design and manufacture of lightweight components for the transportation sector. Furthermore, discontinuous fiber reinforced polymers are widely used for semi-structural parts due to their cost-efficient manufacturing capabilities compared to both continuous fiber reinforced polymers and metals. A new hybrid material class aims to combine the specific advantages of continuous and of discontinuous fiber reinforced polymers. Here, continuous fibers reinforcing the main load paths of a discontinuous long fiber composite component allow for cost-efficient, yet high-performing and lightweight fiber reinforced polymer structures. Such continuous-discontinuous long fiber reinforced polymer structures possess a wide range of internal interfaces, which affect the structure's fracture behavior. In order to develop design and simulation methodologies for this material class, reliable methods are required to characterize and model the materials internal interfaces.

The thesis at hand considers methods to characterize and model such interfaces and applies them to the materials and manufacturing processes specific for this novel material class. Therefore, experimental investigations on the fiber-matrix interfaces as well as on the lamina interfaces of continuous fiber reinforced polymers are conducted and analyzed regarding their usability in the product development process. A combined experimental-numerical

approach is used to validate the experimental results on the one hand and to analyze the advantageous modeling schemes of such materials on the other hand.

Acknowledgment

The research presented in this thesis was conducted during the period of July 2015 through October 2018 at the Fraunhofer Institute for Mechanics of Materials IWM, the Institute for Applied Materials – Computational Materials Science at the Karlsruhe Institute of Technology (KIT), at the Department of Mechanical and Materials Engineering and the Fraunhofer Project Centre for Composites Research (FPC), the latter two located at the University of Western Ontario at London, ON, Canada. It was funded by the German Research Foundation (DFG) within International Research Training Group *Integrated engineering of continuous-discontinuous long fiber reinforced polymer structures* (GRK 2078), which is gratefully acknowledged.

During the research work, I cooperated with a large number of supportive researchers whom I want to thank. First of all, I want to express my great gratitude to Jörg Hohe, co-examiner of this thesis and my direct superior at Fraunhofer IWM, for supervising my thesis and spending hours with discussions on experimental and numerical details. His huge knowledge and thoughtful guidance supported my research fundamentally. Furthermore, I want to express my sincere appreciation to Peter Gumbsch for many valuable thought-provoking impulses as well as his essential input in finalizing this thesis and for providing the possibility to work on this research at both KIT and Fraunhofer IWM in general.

I want to sincerely thank Takashi Kuboki for co-examining this thesis and for supervising my research project conducted at the University of

Western Ontario. His critical questions draw my attention to many important aspects in the manufacture and characterization of sample plaques and thus supported this research. Also, my thanks go to Louis Kaptur, Ehsan Ameri, Steve Jones, and Rob Cosh for their counsel and assistance in the manufacture of the sample plaques at FPC. Furthermore, I want to thank Jeff Wood for his support in both scientific and administrative challenges during my research stay at the University of Western Ontario.

I wish to thank Thomas Bölke for chairing the examination committee. Furthermore, I sincerely appreciate his dedication to our International Research Training Group GRK 2078 by spending countless hours guiding and advising this group, which made the fascinating research conducted possible. I greatly appreciate the collaborative and joyful working atmosphere within this group, to which all members have contributed. Especially, I want to thank Pascal Pinter and Ludwig Schöttl for their patient μCT analysis of my micro specimens.

I express my thanks to my student assistants at Fraunhofer IWM, Lucas Paul Mayer and Kerstin Dittmann. Their professional work and great patience were indispensable for the preparation, handling, and testing of numerous microscopic specimens. I wish to thank Zalikha Murni Abdul Hamid for sharing her vast and valuable experience in operating our micro tensile test set-up. My thanks go to Claudio Findeisen for sharing his incredible knowledge on material and damage modeling. I like to thank Peter Tempel and Christian Eichheimer for their support in Python and Mathematica scripts, involving many discussions on geometric modeling. Furthermore, I want to sincerely thank Michael Deissenbeck and Gerhard Stöhr, reliably supporting the set-up, validation, and repair of measuring equipment of any kind and sometimes making the impossible possible after all.

Last but not least, I want to express my deepest gratitude to my family and my closest friends. Their limitless and unconditional support and their

beliefs in me made this thesis possible. Finally, I want to thank Viktoria, for her invaluable calming and encouraging support on the last steps towards my final examination.

Karlsruhe,
Freiburg i. Br., 2019 *Michael Schober*

Publications and Presentations by the author

Schober, M., Kuboki, T., Ameri, E., Hohe, J., and Peter, G. (2017a). Effects of Process Parameters on the Interlaminar Fracture Toughness of GF-PA6-Tapes. *Proceedings in Applied Mathematics and Mechanics*, 17(1):273–274.

Schober, M., Hohe, J., and Kuboki, T. (2017b). Combined Macro- and Micro-Mechanical Analysis of Instable Crack Propagation in Interlaminar Fracture Toughness Tests. *7th GACM Colloquium on Computational Mechanics for Young Scientists from Academia and Industry: Proceedings*, 7(1):665–668.

Abdul Hamid, Z. M., Florea, M., Fliegener, S., Schober, M., Hohe, J., and Rühe, J. (2019). Chemical modification of fiber-matrix interfaces for enhancing the strength and recyclability of lightweight materials. *Advanced Engineering Materials*, 21(6):1800590.

Schober, M., Kuboki, T., Ameri, E., Hohe, J., and Gumbsch, P. (2017a). Effects of Process Parameters on the Interlaminar Fracture Toughness of GF-PA6-Tapes. *88th GAMM Annual Meeting*, International Association of Applied Mathematics and Mechanics, Weimar.

Schober, M., Hohe, J., and Kuboki, T. (2017b). Combined Macro- and Micro-Mechanical Analysis of Instable Crack Propagarion in Interlaminar

Fractgure Toughness Tests. *7th GACM Colloquium on Computational Mechanics for Young Scientists from Academia and Industry*, German Association for Computational Mechanics, Stuttgart.

Schober, M., Abdul Hamid, Z. M., Hohe, J., Fliegener, S., and Kennerknecht, T. (2017c). Numerical-Experimental Characterization of Fiber Matrix Interfaces in Fiber Reinforced Plastics. *CCeV Seminar on Fibers and Matrices*, Carbon Composites e.V., Augsburg.

Schober, M., Kuboki, T., Gumbsch, P., and Hohe, J.(2018). Combined Macro- and Micro-Mechanical Analysis of the Fracture Behavior in Interlaminar Fracture Toughness Tests. *Materials Science and Engineering*, Deutsche Gesellschaft für Materialkunde e.V., Darmstadt.

Contents

Acronyms

μCT	micro-computed tomography
CFRP	carbon fiber reinforced polymers
CoDiCoFRP	continuous-discontinuous long fiber reinforced polymers
CoFRP	continuous-fiber reinforced polymers
DiCoFRP	discontinuous-fiber reinforced polymers
FRP	fiber reinforced polymers
ATL	automated tape laying
CC	compliance calibration
CF	carbon fiber
CMC	ceramic matrix composites
CTOD	crack tip opening displacement
CZ	cohesive zone
DCB	double cantilever beam test
DFG	Deutsche Forschungsgemeinschaft
DIC	digital image correlation
ENF	end notched flexure test
FE	finite element

FEA	finite element analysis
GF	glass fiber
IAM-WK	Institute for Applied Materials – Materials Science
IFSS	interfacial shear strength
ILSS	interlaminar shear strength
KIT	Karlsruhe Institute of Technology
LFT	long-fiber reinforced thermoplastic
LFT-D	dirct long-fiber reinforced thermoplastic process
MBT	modified beam theory
MCC	modified compliance calibration
PA6	polyamide-6
PP	polypropylene
PTFE	polytetrafluoroethylene
SBBT	short beam bending test
SEM	scanning electron microscopy
SFFT	single fiber fragmentation test
SMC	sheet molding compound
UD	unidirectional
UPPH	unsaturated polyester polyurethane hybrid
VE	vinyl ester

WoA	work of adhesion

List of Symbols

Symbol	Description	Unit
A	Cross-sectional area	mm^2 / μm^2
B	Specimen width	mm
D_f	Fiber diameter	µm
F_{max}	Maximum force reached throughout test procedure	N
$F_{5\%}$	Critical force to start the crack propagation in an ENF test	N
F	Force	N
L	Span length of an ENF test	mm
V_f	Fiber volume fraction	%
W_A	Work of Adhesion	$J\,m^{-2}$
$\bar{\tau}_{ult}$	Mean τ_{ult}, averaged over l_e	MPa
$\boldsymbol{\delta}$	Cohesive surface separation vector	mm
$\boldsymbol{\sigma}$	Cauchy stress tensor	MPa
$\boldsymbol{K}$	Cohesive zone stiffness tensor	$N\,mm^{-3}$
$\boldsymbol{n}$	Surface normal vector	
$\boldsymbol{t}$	Traction vector on a surface	MPa
$\boldsymbol{u}$	Three-dimensional displacement vector	mm
$\mathscr{G}_c$	Critical fracture energy release rate	$J\,m^{-2}$
σ_{adh}	Radial stress along the fiber matrix interface, *adhesional pressure*	MPa

Symbol	Description	Unit
σ_{ult}	Ultimate adhesional pressure at the onset of debonding	MPa
τ_{app}	Apparent interlaminar shear strength	MPa
τ_{ult}	Ultimate interfacial shear strength	MPa
l_e	Fiber length embedded in matrix for characterizing the interface	mm
a	Crack length in a fracture toughness test specimen	mm
a_0	Initial crack length in a fracture toughness test specimen	mm
$d_{5\%}$	Critical displacement referring to $F_{5\%}$ in an ENF test	mm
d	Loading element displacement	mm
$\dot{d}$	Loading element displacement rate	$\mathrm{mm\,min^{-1}}$
E	Young's modulus	GPa
ε	Strain	%
Γ^c	Critical separation energy leading to complete failure of a cohesive zone	$\mathrm{J\,m^{-2}}$
l	Strain gauge length	mm
l_0	Initial strain gauge length	mm

1 Introduction

1.1 Motivation

During the recent decades, the curb weights of vehicles of the transportation sector have been increasing steadily (Siebenpfeiffer, 2014). The reasons for this trend lay in increased customer expectations for comfort on the one hand and in stricter safety and environmental regulations on the other hand (Braess and Seiffert, 2013). Next to the driving speed, the vehicle mass has the greatest impact on the driving resistance and thereby on the vehicle's energy consumption and CO_2-emissions. Hence, a conflict of objectives exists when both mass adding requirements and the reduction of CO_2-emissions enforced by the European Union need to be fulfilled (Friedrich, 2013; Heuss et al., 2012; Schuh et al., 2014). In order to resolve this conflict, manufacturers replace steel by lightweight materials in single components, such as aluminum or fiber reinforced polymers (FRP) (Siebenpfeiffer, 2014; Henning and Moeller, 2011). FRP can be classified by the type of reinforcing fibers: continuous-fiber reinforced polymers (CoFRP), consisting of an high percentage of aligned fibers extending throughout the entire structure, and discontinuous-fiber reinforced polymers (DiCoFRP), which consist of a medium percentage of chopped fibers with random orientation (Kärger et al., 2016). Especially CoFRP seem promising in terms of their weight reduction potential, as Figure 1.1 visualizes for carbon fiber reinforced polymers (CFRP).

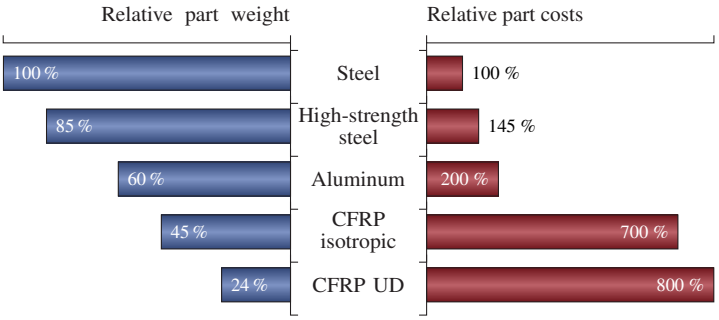

Figure 1.1: Structural parts approximate weight and cost comparison with equal functions in relation to steel components (Lässig et al., 2012; Friedrich, 2013)

The high mass-reduction potential of CFRP results from their high specific stiffness and strength as well as their fracture toughness and fatigue strength, especially when the fibers are aligned unidirectionally (UD). However, severe restrictions exist on the design of a CFRP structure. Moreover, the complex manufacture of such structures processing expensive raw materials increases component costs. For these reasons, the application of CFRP components in mass-produced products is limited (Achternbosch et al., 2003). DiCoFRP on the other hand offer only limited mechanical performance due to the finite length of the fibers and their heterogeneous orientation distribution, but also large freedom in design, making complex geometries possible (Ehrenstein, 2006; Henning and Moeller, 2011). The large freedom of design makes DiCoFRP capable of functional integration which allows to combine several components into one. This capability and the potentially low expenses for molds and tools can lead to a significant cost reduction compared to a corresponding steel structure (Mallick, 2007). For these reasons, this

material class is widely used, yet only for semi-structural parts, such as trunk lids or fenders, and not for structural body parts (Siebenpfeiffer, 2014).

1.1.1 Novel Hybrid Material Class CoDiCoFRP

In order to combine the specific advantages of the two FRP classes mentioned above – and to avoid their specific disadvantages – the International Research Training Group GRK 2078 introduces a new hybrid material class called continuous-discontinuous long fiber reinforced polymers (CoDiCoFRP). Here, the high-performing but cost intensive CoFRP are supposed to carry the main loads only where needed, whereas the DiCoFRP provides local functionalization such as ribs or joint support structures. In this way, a high performing composite structure can be created, yet ensuring cost efficiency by simple geometries of the CoFRP areas and reasonable tooling costs. The research group GRK 2078 aims for a fully integrated approach for the devel-

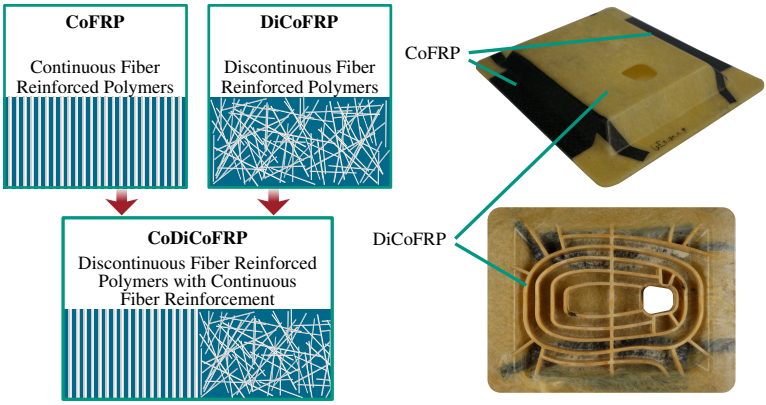

Figure 1.2: Hybrid composite material class continuous-discontinuous long fiber reinforced polymers (CoDiCoFRP) with exemplary structure, according to (Kärger et al., 2016)

opment of CoDiCoFRP structures capable for mass production, including all aspects necessary for both a physical and a virtual process chain, namely manufacturing technologies, characterization and modeling methodologies, and tools for optimization and design (Kärger et al., 2016). Figure 1.2 shows the principle of CoDiCoFRP and a structure with black CoFRP patches on a beige DiCoFRP structure featuring local ribs.

CoDiCoFRP structures can be manufactured using both thermosetting and thermoplastic matrix systems. Their general manufacturing process consists of three steps: (1) production of semi-finished DiCoFRP, (2) production of semi-finished CoFRP, and (3) the joint co-molding of both components to the final CoDiCoFRP structure, as illustrated in Figure 1.3 with respect to thermosetting matrices. The steps differ with respect to the used matrix system. For thermosetting matrices, a sheet molding compound (SMC) process is used for the DiCoFRP, in which glass fibers (GF) or carbon fibers (CF) are chopped and dispersed between two resin films on a flat conveyor belt. Subsequently, the obtained planar compound is coiled up and stored as it needs maturing time in order to develop its desired characteristics. The CoFRP component is manufactured similarly on a heatable flat conveyor belt, cut and draped to the desired shape. Meanwhile, the matrix is transformed into the B-stage – a partly cured yet not cross-linked state of the polymerization – making the reinforcement stiff enough for storage and handling processes. The final hybrid structure then is obtained by compression co-molding of both components (Bücheler, 2018).

CoDiCoFRP structures with thermoplastic matrix systems are usually manufactured by means of a long-fiber reinforced thermoplastic (LFT) compression molding process for the DiCoFRP component and an automated tape laying (ATL) process for the CoFRP component (Graf, 2016). Compared to the process for thermosets, the DiCoFRP component needs to be compression co-molded directly after its production. Here, a dirct long-fiber

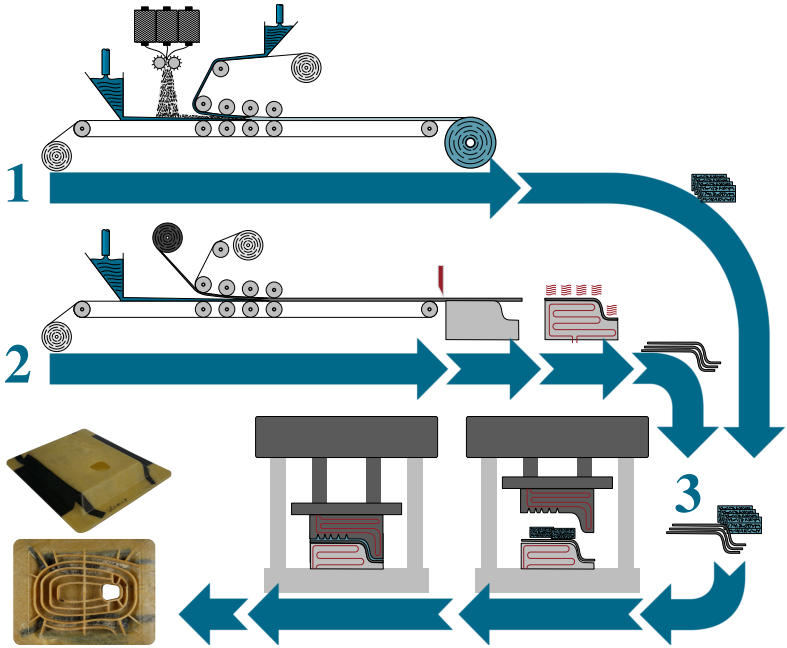

Figure 1.3: Schematic manufacturing process of locally continuous fiber reinforced sheet molding compound (SMC): semi-finish production of (1) SMC and (2) reinforcing patches, (3) co-molding of the semi-finished products to CoDiCoFRP structure (Bücheler, 2018)

reinforced thermoplastic process (LFT-D) with a dual extruder system – one extruder melts the polymer and the second extruder doses the fibers into the polymer – can be used (Krause et al., 2005; Henning et al., 2005; Krause et al., 2003). Unidirectional (UD) glass or carbon fiber reinforced thermoplastic tapes are laid to net-shape by means of an ATL process and consolidated to be used as the CoFRP component. The consolidated tape lay-up is heated to process temperature prior to the co-molding with the LFT charge to the final CoDiCoFRP structure (Graf, 2016).

1.1.2 Interfaces in CoDiCoFRP

In general, the mechanical characteristics of fiber reinforced polymers significantly, yet not exclusively, depend on their constituents, i. e. the polymer, the fibers, and the fiber distribution within the component. Since the mechanical principle of any FRP is the separation of functions – for instance the fibers carry the loads, whereas the matrix transfers loads between them – the interfaces connecting the fibers to the matrix play a substantial role within the material system. Especially when structural failure is considered, whether quasi-static, cyclic, dynamic, or due to creep effects, the interface characteristics strongly affect the dominant material effects causing failure (Kim and Mai, 1998; Mallick, 2007). Consequently, reliable methodologies for the characterization and modeling of interfaces are required for failure predictions of CoDiCoFRP structures.

The impact of failing fiber-matrix interfaces on the macro-mechanical material behavior of a long-fiber reinforced thermoplastic (LFT) structure was shown by Fliegener (2015) and is illustrated in Figure 1.4. Here, the engineering stress-strain-curve of a tensile test specimen made of LFT is plotted in comparison to two curves gained by finite element (FE) simulations, which are based on models containing a micro-structure statistically equivalent to the physical specimen. The simulation represented by the blue curve assumes a perfect fiber-matrix interface at which no failure can occur, whereas the simulation represented by the red curve assumes a finite strength of the interfaces. The point where the two simulation curves drift apart indicates the onset of interfacial failure (Fliegener, 2015). The large difference between the two curves regarding the ultimate strength and the strain at failure emphasizes the influence of the interface and the need for a thorough understanding of its behavior.

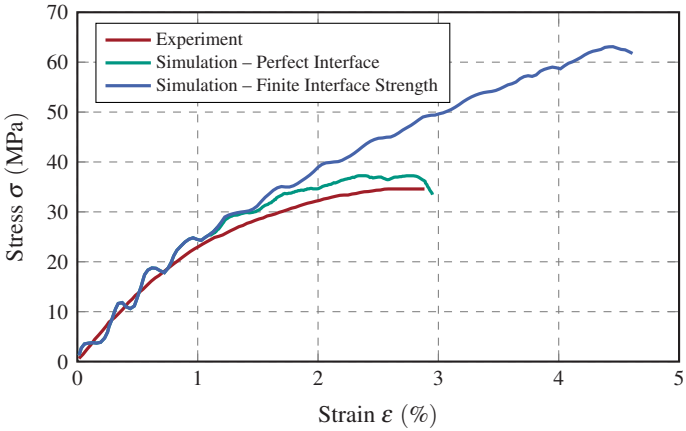

Figure 1.4: Impact of failing fiber-matrix interfaces on the macro-mechanical material behavior of LFT (Fliegener, 2015)

Regarding CoDiCoFRP, several kinds of interfaces exist on different scales of the material. Figure 1.5 schematically shows a scale hierarchy of a CoDiCoFRP structure, from the macroscopic Co-DiCoFRP interfaces to the microscopic interface between the polymer and single fibers (illustrated by (Schemmann, 2018)). On the macro-scale, the interface between the CoFRP patches and the DiCoFRP base structure is the most apparent interface. As the patches shall reinforce the entire structure, this interface is responsible for transferring the main loads from the structure into the high performing patches and hence it can have an essential impact on the structure's global failure mode. For the same reason, creep effects in the interface cannot be ruled out regarding long-term loading scenarios. Depending on the geometry of the structure and on its designated load case, the patches themselves might be stacked and pre-consolidated prior to co-molding the CoDiCoFRP structure (Bücheler, 2018). Hence, lamina interfaces possibly exist within

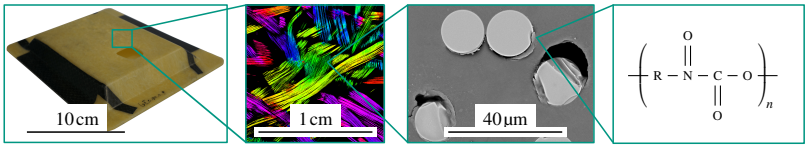

Figure 1.5: Schematic interface hierarchy of a CoDiCoFRP component: between CoFRP and DiCoFRP, between fiber agglomerations and pure matrix areas, and between an individual fiber and matrix (CoDiCoFRP demonstrator manufactured by Bücheler (2018) at Fraunhofer ICT, Germany; SMC micro-structure visualized by Pinter (2018) by means of μCT analysis; debonded fiber-matrix interfaces in a SEM micrograph by the author; illustration by Schemmann (2018))

the patches which potentially affect the global characteristics of the structure, such as the impact resistance (Kuboki et al., 2003).

As described above, fiber-matrix interfaces generally play an important role in fiber reinforced composites. Their characteristics strongly depend on the individual material composition: the matrix, the reinforcing fibers, and also the polymeric sizing on the fiber surfaces, which is applied at the end of the fiber manufacturing process for protection, process capability, and bonding purposes (Kim and Mai, 1998). Since the material compositions differ between the CoFRP region and the DiCoFRP region of a CoDiCoFRP structure, the fiber-matrix interfaces have to be examined individually for each region. Moreover, the interfaces in the two regions are loaded in different modes: since the fibers in the CoFRP region are aligned along a main load path, interfaces are mainly loaded by shear stresses, whereas the randomly oriented fibers within the DiCoFRP structure lead to a much more complex stress state on the interfaces, especially near the fiber ends (Takahashi and Choi, 1991).

Another distinction between thermosetting and thermoplastic matrix systems must be made regarding the micro-structure of the DiCoFRP region: whereas the LFT process usually separates the fibers from each other well

(Geiger et al., 2006), fiber agglomerations in various extents can be found in thermosetting SMC components (Taketa et al., 2008). Special consideration of the interfaces within such fiber agglomerations might be necessary, since the manufacturing process of glass fibers and heavy-tow carbon fibers often covers the rovings with significant amounts of sizing (Ehrenstein, 2006). Moreover, since Bruce (2011) showed for woven glass fiber fabric reinforced epoxy that fracture can occur on the interface between a fiber roving and the surrounding matrix, this interface type may also matter in fiber bundle rich SMC structures.

1.2 Objectives and Approach

The thesis at hand aims at methods of the characterization of interfaces in fiber reinforced polymer structures, which allow for the modeling of the behavior and failure of the interface and thus the optimization of the material and the structures made thereof.

In order to achieve these objectives, the current state of research is studied regarding the characterization and modeling methodologies of interfaces in fiber reinforced polymers (FRP) with respect to quasi-static loading conditions, especially in consideration of the novel hybrid material class continuous-discontinuous long fiber reinforced polymers (CoDiCoFRP) and its specific manufacturing processes. Furthermore, physical experiments are conducted analyzing fiber-matrix interfaces in DiCoFRP by means of single-fiber droplet tests and multi-fiber micro-tensile tests. Lamina interfaces in CoFRP are examined by means of interlaminar fracture toughness tests in consideration of possible manufacturing process impacts. For a further evaluation, the experiments are modeled numerically using finite element analyses (FEA). Within these simulations, the interfaces are modeled by means of cohesive zone formulations with traction-separation laws. A

reverse engineering approach is applied in order to obtain the parameters governing the interfaces and thereby the investigated materials, making the resulting models usable for failure predictions on the macro-scale.

As the manufacturing process can affect the characteristics of the interfaces, the corresponding processes for both thermosetting and thermoplastic matrices are taken into account. Therefore, unidirectional (UD) glass fiber reinforced polyamide-6 (GF-PA6) tapes are used investigating the lamina interface. Regarding fiber-matrix interfaces, a glass fiber reinforced unsaturated polyester polyurethane hybrid (UPPH) resin manufactured with a sheet molding compound (SMC) process is mainly used. The sample material is manufactured using industry scale machinery capable for mass production, such as an ATL machine and a state of the art SMC flat conveyor plant.

1.3 Outline of the Thesis

The thesis at hand describes the current state of research regarding the characterization and modeling of interface in fiber reinforced polymer structures with a focus on the field of fiber-matrix interface. Moreover, the approach of modeling interfaces in general by means of cohesive zone formulations for numerical simulations is compiled.

Experimental investigation of fiber reinforced polymer interfaces are conducted on three different scales: on the microscale by means of the single-fiber microbond test, on the mesoscale by means of the multi-fiber tensile test, and on the macroscale by means of interlaminar fracture toughness tests. The test procedure and the corresponding results are described individually for the three scales of interest.

The experiments on each scale are modeled numerically and analyzed further regarding their capabilities to provide results usable in further numerical simulations. The results are discussed and connected to the experimentally

obtained data sets. Suggestions for the further research on this topic complete this thesis.

2 State of Research on Interfaces in Fiber Reinforced Polymers

The structural integrity of a fiber reinforced composite part depends on the successful interaction between its constituents – here the CoFRP and the DiCoFRP sections as well as the fiber and the polymer in the sections' microstructures – and the applied loading conditions. Especially when a DiCoFRP structure is loaded until failure, the relevant fracture mechanisms depend on the exact composition of the composites, namely the fiber length and orientation distribution in addition to constituent interaction mentioned above, but also the local fiber dispersion and the local fiber impregnation. Concerning this matter, the influence of the fiber length and fiber volume fraction on the mechanical properties of a DiCoFRP structure is well analyzed in the literature (Thomason and Vlug, 1996; Thomason et al., 1996; Thomason and Vlug, 1997; Thomason, 2002, 2007). Regarding CoFRP, failure is usually divided in fiber failure and inter-fiber failure only, with further subdivisions of inter-fiber failure with respect to the applied load case (Puck and Schürmann, 2002). In general, the following fracture mechanisms can be distinguished when examining failure of a fiber reinforced composite on the micro-scale (Zollo, 1997):

- fiber rupture,
- matrix cracking,
- fiber pull-out,

- fiber bridging, and
- fiber matrix debonding.

These failure mechanisms are schematically illustrated in Figure 2.1. Here, especially the fiber bridging effect is of interest. When a propagating crack exceeds a fiber perpendicular to the crack, the fiber can still be attached to both crack surfaces, creating a load carrying fiber bridge from one crack face to the other. The consequence of such fiber bridging effects is either the failure of the fiber or the embedding matrix in case of good fiber matrix bonding, or the pull-out of the fiber due to the failure of the fiber-matrix interface. However, the interfaces can also fail completely without any fiber pull-out effects, leaving a blank fiber surface on the one face and a fiber bed on the other crack face (Rösler et al., 2012). Provided a sufficient length of the fibers, excessive fiber pull-out or interface debonding indicate weak fiber matrix bonding. However, fiber pull-out can also contribute to the

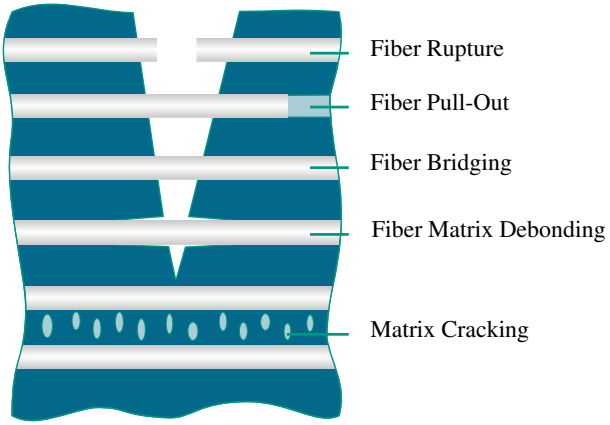

Figure 2.1: Possible fracture mechanisms in fiber reinforced composites, according to Zollo (1997)

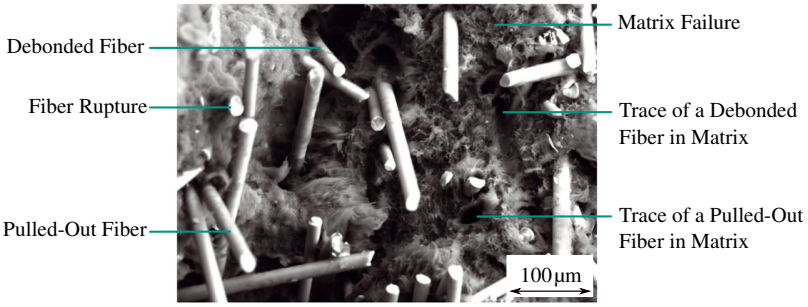

Figure 2.2: Fracture surface of a LFT with different fracture mechanisms, captured by means of scanning electron microscopy (SEM) by (Hohe et al., 2016)

fracture behavior in a positive way, as the friction between the fiber and the matrix after interface failure can increase the materials fracture toughness (Bheemreddy et al., 2013).

Usually, all of the mentioned mechanisms occur when a DiCoFRP structure fractures. Figure 2.2 shows a fracture surface of a LFT material captured by means of SEM. Taking into consideration that bridging fibers lead to fiber rupture or fiber pull-out – due to failure either of the interface or the surrounding matrix – while the crack is propagating, all of the mentioned fracture mechanisms are visible in this micrograph. Traces within the matrix are visible indicating pulled-out fibers and blank fiber surfaces reveal interfaces to have failed. These occurrences well illustrate the effects of interface failure on the material's fracture pattern.

2.1 Characterizing fiber-matrix interfaces in Co- and DiCoFRP

In order to properly predict structural failure of FRP, macroscopic material models require a suitable model for the mechanical interface behavior.

Therefore, several methods have been developed to characterize and model fiber-matrix interfaces. These methods consider different levels of the interface – similar to the scale hierarchy illustrated in Figure 1.5: the molecular scale, the micro-scale, and the meso-scale. Whereas, molecular scale considers the molecular adhesion between two chemical surfaces (Figure 2.3a), the micro-scale considers a homogeneous single fiber embedded within a homogeneous matrix (Figure 2.3b). The meso-scale considers not only a single fiber, but numerous fibers and their distribution within the embedding homogeneous matrix (Figure 2.3c).

On the molecular level (Figure 2.3a), the interface is described by means of the chemical composition of two dissimilar phases and arises from chemical bonds or intermolecular forces, such as covalent bonds or van der Waals forces, respectively. The interfacial strength depends on the concentration of these bonds and their corresponding energies and is characterized by means of the work of adhesion (WoA) W_A. The WoA is done by all chemical and physical interactions involved in the interfacial load transfer. In contrast, the micro-scale in Figure 2.3b is described only

Figure 2.3: Characterization scales of the interface between fiber (black) and matrix (grey): (a) molecular scale, (b) micro-scale, and (c) meso-scale (Zhandarov and Mäder, 2005)

by engineering terms for load transmission or failure. The typical values characterizing the micro-scale failure are the interfacial shear strength (IFSS) – also referred to as ultimate shear strength τ_{ult} – and the critical energy release rate $\mathscr{G}_c$. A further, more complex interfacial failure criterion is provided by the adhesional pressure σ_{adh}, which describes the normal stress component on the interface at the onset of debonding (Pisanova et al., 2001a). The meso-scale (Figure 2.3c) expands this model to the actual micro-structure of the analyzed composite, yet using the same assumptions for the single interfaces as the micro-model (Pisanova et al., 2001b; Zhandarov and Mäder, 2005).

In the literature, it is widely accepted to employ the IFSS as a value for adhesion of the fiber-matrix interface (Yang and Thomason, 2012). Numerous destructive, micromechanical test methods are available, also with respect to the three different scales (Pisanova et al., 2001a; McCarthy et al., 2015). Most of the test methods have in common that they require custom made specimens, which contain a single fiber embedded in a particular manner into a specific amount of polymer. In general, the test methods can be classified into two groups depending on the loading scenario: (i) tests, which apply the load directly onto the fiber, and (ii) tests with external matrix loading. Example tests of the former group are the single-fiber pull-out test, where a fiber tip embedded in matrix is pulled out of matrix, the single-fiber push-out test, where a fiber in a thin-slice micro-composite is pushed out of the matrix by indentation, and the microbond test, where a droplet of polymer applied to a fiber is sheared off by a knife edge. The fiber fragmentation test and the Broutman test are examples for the latter group, which is in principle also capable of analyzing multi-fiber micro-composites, as well (Zhandarov and Mäder, 2005; McCarthy et al., 2015). Here, the fiber is completely embedded within a polymer specimen, which is loaded in tension or compression, respectively, until fiber rupture or interface failure occurs

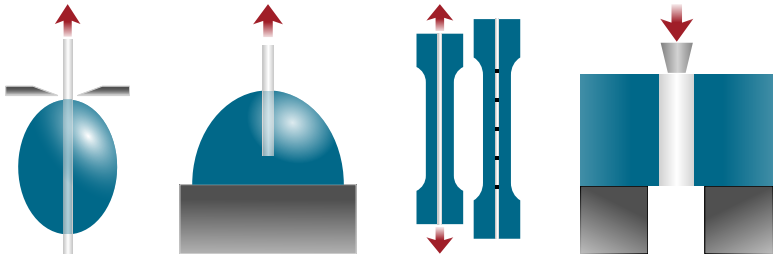

Figure 2.4: Illustration of widely spread characterization methods for fiber-matrix interfaces with gray fibers, blue matrix, black knife/substrate, and red load: (a) microbond-test (Zhandarov et al., 2006), (b) fiber pull-out test (Zhandarov et al., 2006), (c) single-fiber fragmentation test (Greenfield et al., 2000), (d) fiber push-out test (Chandra and Ghonem, 2001)

(Tripathi and Jones, 1998; Nishikawa et al., 2007; Ageorges et al., 1999). The most important test methods for the fiber-matrix interface regarding the interfacial shear strength are illustrated in Figure 2.4.

Further test methods examining interface failure characteristics by distinguishing normal and shear failure have been developed. Such methods use for example cruciform specimens, in which a single fiber is embedded within a resin perpendicular or at a certain angle to the loading direction, resulting in separate values for the normal strength and for the shear strength of the fiber-matrix interface (Tandon et al., 2002; Ogihara and Koyanagi, 2010; Koyanagi et al., 2012).

2.1.1 Fiber Fragmentation Test

In general, the applied test method shall suit the interface loading scenario in a structural application. Regarding CoFRP, one test method replicating a similar stress distribution on the interface is the single fiber fragmentation test (SFFT) (Zhandarov and Mäder, 2005). This test method originally

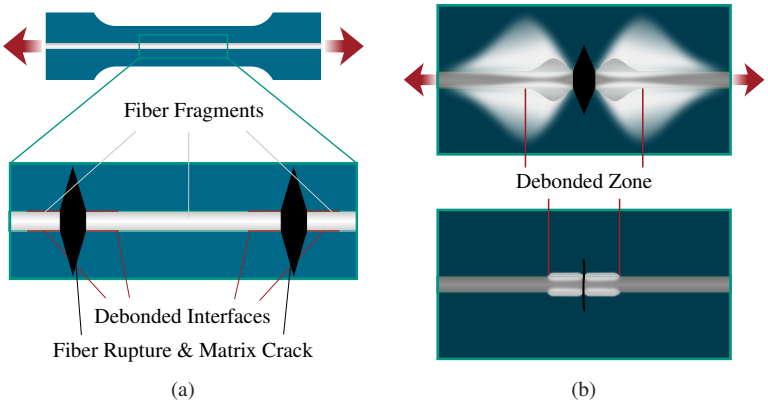

Figure 2.5: Single fiber fragmentation test: (a) schematic specimen and observable fracture pattern (according to Nishikawa et al. (2008)), (b) schematic birefringence pattern of an E-glass/epoxy specimen lit by cross-polarized light: (top) load-applied state, (bottom) load-released state (according to Kim and Nairn (2002))

proposed by (Kelly and Tyson, 1965) has been amply analyzed in terms of its application and its theoretical basis (Copponnex, 1996; Tripathi and Jones, 1998). Figure 2.5a illustrates the SFFT in more detail: a continuous fiber is longitudinally embedded into a polymeric tensile test specimen. Since the matrix features a much higher elongation-to-failure than the reinforcing fiber, the fiber breaks in multiple locations when the specimen is loaded in tension, including matrix cracks and debonded interfaces in the surroundings of the fiber ruptures. Such a fiber rupture results in a specific pattern when lit by cross-polarized light, which is schematically shown in Figure 2.5b in a load-applied state in the top image and in a load-released state in the bottom image. Such colored pattern – called birefringence or photoelastic pattern – exhibits the stresses and strains due to interfacial shear and friction at the fiber-matrix interface (Feih et al., 2004). It consists of two overlaying patterns symmetric around the fiber breaks – a large, bright pattern and a small, darker

pattern overlaying the large pattern. The small pattern is caused by frictional stresses and indicates the debonded zone and thus remains after the load is released (Kim and Nairn, 2002). With the amount of fiber fragments after testing and the size of the debonded areas, the interfacial strength can be determined (Zhandarov and Mäder, 2005; Goda et al., 1995). By means of an enhanced fracture model and with a cyclic unloading and reloading procedure after the first fiber rupture, Ramirez et al. (2009) could derive both the interfacial fracture toughness and the effect of fiber-matrix-friction. In contrast to the original procedure, this method focuses exclusively on the growth of the debonded area at the tip of a ruptured fiber due to a loading cycle. The single fiber fragmentation test method has been expanded to the multi-fiber fragmentation test in order to consider the interaction between the fibers and hence the interdependency of micro-cracking events in a CoFRP structure. Here, a limited number of fibers is arranged in a two-dimensional and later in three-dimensional array and embedded into a matrix comparable to the SFFT procedure (Li et al., 1995; Kim et al., 2009; McCarthy et al., 2015).

2.1.2 The Microbond and the Single-Fiber Pull-Out Test

The stress state on the interface in a real application shall be replicated by an experimental test set-up. However, test methods like the SFFT are limited to the interfacial shear stress. In contrast, when the interfacial adhesion is subject to investigation, test methods directly loading the fiber – i. e. microbond, pull-out, but also the push-out test – are more promising investigation tools (Zhandarov and Mäder, 2005; Zhandarov et al., 2006). In these tests, the complete interface of the embedded fiber is debonded, while the occurring forces and displacements are recorded. The single fiber pull-out test and the microbond test result in very similar force-displacement curves (Yang and

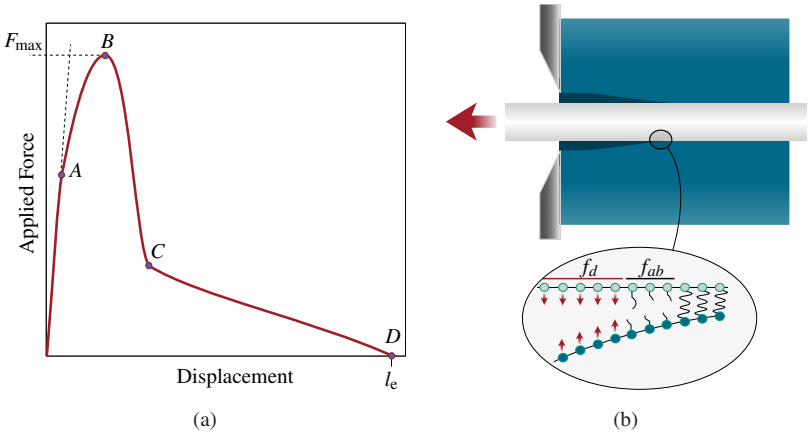

Figure 2.6: (a) idealized force-displacement-curve from a pull-out test (Zhandarov and Mäder, 2014), (b) schematic crack opening on the molecular scale during a microbond test (Pisanova et al., 2001a)

Thomason, 2012). Figure 2.6a illustrates an idealized force-displacement curve from a pull-out test. During this schematic test process, the interface remains intact during the initial loading. The interface debonding initiates at point A, causing the maximum force F_{max} in point B, and ends in the point C. In the following section to the point D, the required force is caused by friction occurring between the fiber and the matrix. Regarding pull-out and push-out tests, this friction and hence the recorded force decrease with the contact area, as the fiber is embedded in the matrix with a limited length l_e. The curve received from a microbond test shows a plateau, instead, as the area of contact of the matrix droplet and the fiber remains constant (Zhandarov and Mäder, 2014).

During these experiments, the crack initiates in normal direction to the interface (Piggott, 1995) and propagates due to the subsequent breakup of molecular interactions responsible for the polymer adhesion. These interac-

tions consist of inter-molecular dispersion forces – van der Waals' forces, for instance – and acid-base forces (Pisanova et al., 2001a). These acid-base forces arise from the interaction between acidic and basic chemical groups within the involved materials and can strengthen the possible level of adhesion significantly (Fowkes, 1981). This debonding process on the molecular scale is illustrated in Figure 2.6b, where the sections of the failing interfaces are labeled f_d where dispersion forces act and f_{ab} where acid-base forces act in addition (Zhandarov and Mäder, 2005).

Several methods processing the experimental force-displacement curve have been developed in order to extract the distributions of the adhesional pressure σ_{adh} (Piggott, 1995; Pisanova et al., 2001a,b) and of the interfacial shear stress τ as well as the interfacial fracture toughness $\mathscr{G}_{\mathrm{c}}$ (Pisanova et al., 2001b; Zhandarov et al., 2006; Zhandarov and Mäder, 2014, 2016). The variational mechanics model by Scheer and Nairn (1995) makes the calculation of the stresses within a microbond test specimen possible. The qualitative distribution of the interfacial shear stress τ and of the adhesional pressure

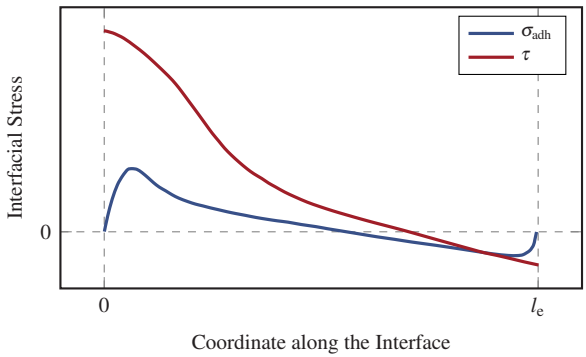

Figure 2.7: Distribution of the adhesional pressure σ_{adh} and the shear stress τ on the interface along the embedded fiber length l_{e} (Pisanova et al., 2001a) according to the variational mechanics model by (Scheer and Nairn, 1995)

σ_{adh} along the embedded length can be derived. The stress distribution is illustrated in Figure 2.7 and shows that the radial stress σ_{adh} has its maximum at the point where the fiber matrix contact begins, and that the shear stress τ vanishes here. A simple way of deriving a failure criterion by these calculations is to define the critical value σ_{ult}. When this value is reached by the adhesional pressure ($\sigma_{adh} = \sigma_{ult}$), interface debonding initiates on the edge of the fiber matrix contact area. The obtained value σ_{ult} is a precise parameter for the characterization of the actual adhesion between the fiber and the polymer due to its direct relation to molecular work of adhesion. However, as the model by (Scheer and Nairn, 1995) is restricted to the microbond test due to the compressive load on the matrix, other tests such as the fiber pull-out test can only be used for a coarse evaluation of the fiber matrix adhesion (Pisanova et al., 2001a; Zhandarov and Mäder, 2005).

2.1.3 Single-Fiber Push-Out Test

The fiber push-out test has first been proposed by Marshall (1984) as a method to analyze the shear stress due to fiber-matrix-friction in ceramic matrix composites (CMC). In the following years, the test method has been developed further by reducing the specimen thickness from originally several millimeters to approximately 30 µm (Kallas et al., 1992; Godara et al., 2010). The schematic test procedure is illustrated in Figure 2.8: by means of a nanomechanical testing system, a single, completely embedded fiber is loaded by an indenter tip. While the fiber is pushed out of the embedding matrix, the interface gradually debonds and frictional forces are generated by the slipping contact surfaces (Tandon and Pagano, 1998; Mueller et al., 2013). Regarding the indenter, pyramidal tip and -flat-end shapes (Mueller et al., 2013), flat-end cone shapes (Haspel, 2014), and cylindrical shapes (Greisel et al., 2014) are used. The evaluation of the test regarding the interface characteristics is

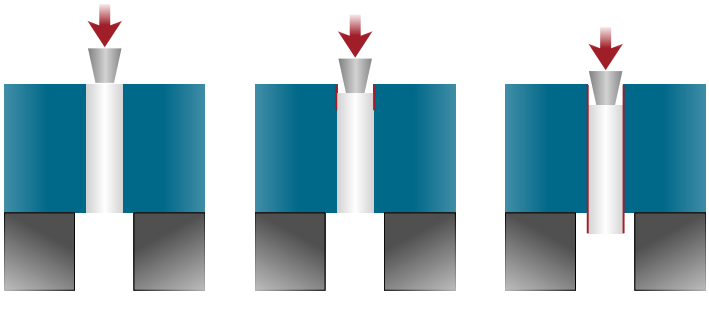

Figure 2.8: Schematic procedure of single-fiber push-out test: (a) beginning of experiment, (b) partial debonding, (c) complete debonding and push-out (Chandra and Ghonem, 2001)

based on the obtained force-displacement curve, which is processed similarly to the force-displacement curve of the fiber pull-out test shown in Figure 2.6a. In contrast to the interface characterization methods described above, the fiber push-out test does not require custom-made specimens. In fact, this test methods allows to analyze the fiber-matrix interface with specimens extracted directly from the structure of interest and, therefore, to analyze also factors which influence the interface characteristics, such as the surroundings of the fiber, the fiber orientation or the fiber impregnation (Kalinka et al., 1997). Furthermore, the influence of process induced residual stresses on the interface strength caused by the mismatch of the thermal expansion coefficients can be analyzed with this test method (Chandra and Ananth, 1995; Greisel et al., 2014).

This test method has been thoroughly analyzed in experimental, analytical, as well as numerical manners in order to reliably derive interface properties from the obtained force-displacement curves. Kerans and Parthasarathy (1991) developed an analytical model to compute the fracture toughness $\mathscr{G}_c$

independently from the stress distribution in the interface region. However, in order to accurately analyze the stress distribution during the push-out test, Tandon and Pagano (1998) showed that the applied models must not neglect radial stresses on the interface. Especially when thin-slice specimens are used, significant bending stresses can occur influencing the debonding behavior of the interface (Kallas et al., 1992). Beyond the analytical calculation, the direct measurement of the interfacial fracture toughness as well as frictional parameters was achieved by means of a cyclic loading, unloading, and reloading procedure by Mueller et al. (2013). An asymmetric fiber configuration surrounding the analyzed fiber was experimentally determined to influence the pattern of debonding progression by skewing the areas of stable and unstable crack growth along the fiber (Mueller et al., 2015). In contrast, numerical investigations show that it influences the peak forces only in the range of $\pm 5\,\%$ (Brylka et al., 2011).

2.2 Characterizing Lamina-Interfaces in CoFRP

Despite their numerous favorable characteristics, laminated continuous-fiber reinforced polymers (CoFRP) are susceptible to delamination due to their matrix dominated interlaminar regions, which is a critical factor in the design of CoFRP structures (Borowski et al., 2015). Delamination can be induced by interlaminar shear stresses – which also arise in an assumed generalized plane stress state – or by through-thickness stresses. Because of the high anisotropy of CoFRP with a low through-thickness strength, external loads and especially transverse impact can initiate delamination (Puppo and Evensen, 1970; Robinson and Hodgkinson, 2000; Kuboki et al., 2002). Examples for such loading scenarios are illustrated in Figure 2.9. Furthermore, since the interface region is matrix dominated and many polymers are susceptible to creep,

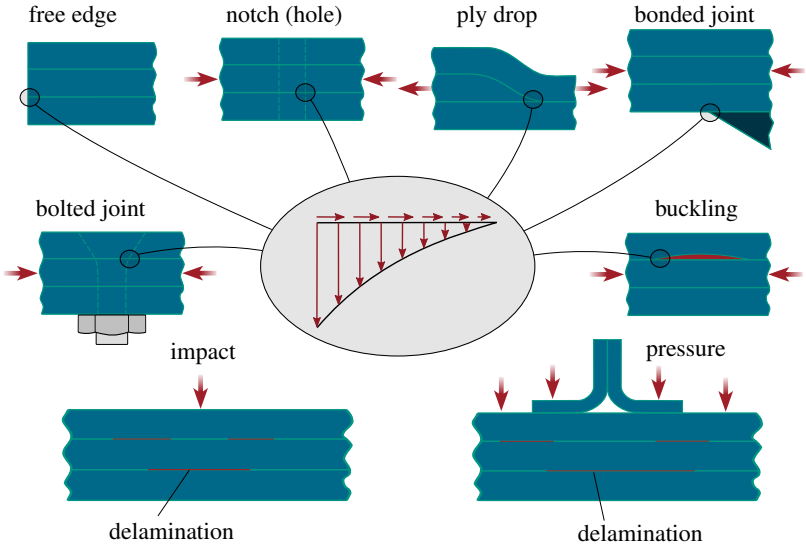

Figure 2.9: Possible loading scenarios causing initiation of delamination in CoFRP (Robinson and Hodgkinson, 2000)

creep deformations can occur due to interlaminar shear stresses (Robinson and Hodgkinson, 2000).

Lamina interfaces are characterized – similar to the characterization of fiber-matrix interfaces – regarding the interlaminar shear strength (ILSS) and the interlaminar fracture toughness, but also regarding the interlaminar shear creep. Especially the fracture toughness is a significant parameter, since it controls the propagation of an initiated delamination and strongly affects the structure's resistance to transverse impacts (Robinson and Hodgkinson, 2000; Thielicke et al., 1999; Kuboki et al., 2003). The following sections describe the current state of investigating the interlaminar shear strength and creep as well as the interlaminar fracture toughness.

2.2.1 Interlaminar Shear Strength and Creep

Several test methods analyzing a material's interlaminar shear behavior are available. A simple and thus widely used test method is the short beam bending test (SBBT), which is standardized in ASTM D 2344 as well as in DIN EN 2563. The SBBT is a three-point bending test of a rectangular specimen with a small span length of 8 mm and 10 mm, according to the standards illustrated in Figure 2.10, or depending on the specimen thickness, in case non-standard thickness materials are analyzed. The small span-to-thickness ratio (approximately 4 to 5) induces high shear forces and leads to interlaminar shear failure (Robinson and Hodgkinson, 2000; Grellmann and Seidler, 2013).

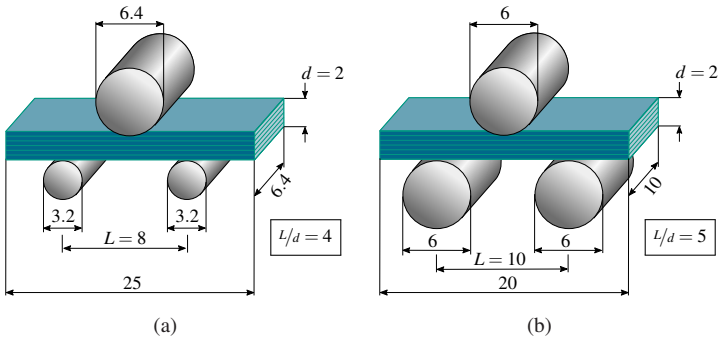

Figure 2.10: Short beam bending test analyzing apparent interlaminar shear test τ_{app}, standardized by (a) ASTM D 2344 and (b) DIN EN 2563 (Grellmann and Seidler, 2013)

The SBBT is evaluated regarding the maximum shear stress according to the classical beam theory. However, numerous studies have shown inadequacies of this theory determining the stress state of the short-beam (He and Makeev, 2014). The stress state is significantly skewed in the loading regions which makes the beam theory inapplicable. Thus, the resulting values do

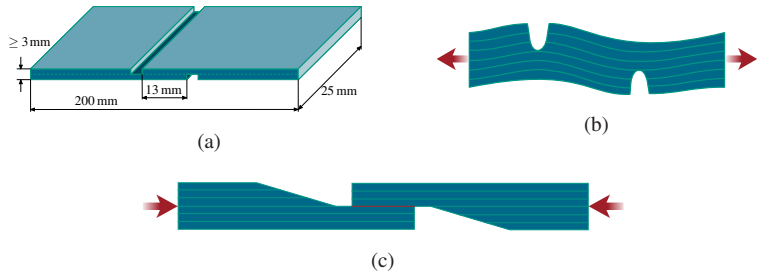

Figure 2.11: Double-notched interlaminar shear test specimen: (a) dimensions according to ASTM D 2730-70, (b) schematic bending behavior during loading (Ehrenstein, 2006), (c) compressive interlaminar creep specimen (Thielicke et al., 1999)

not truly represent the material, but only the apparent interlaminar shear strength τ_{app}. Furthermore, the failure depends on the through-thickness material properties and is highly affected by contact and bending stresses. These circumstances make the actual failure mode much more complex than the assumed pure shear failure mode. The apparent shear strength τ_{app} can therefore not be used as a material model parameter. Since its test procedure is very simple, however, it is widely used as a qualitative and comparative value, for instance for process quality assurance (Robinson and Hodgkinson, 2000).

Further test methods are available yielding more accurate shear strength results than the SBBT, such as the double-notched shear test (Thielicke et al., 1994). As standardized for instance in ASTM D 2730-70 (Figure 2.11a), a rectangular cross-section specimen is unsymmetrically notched – with one notch on each face of the specimen reaching to its mid-plane. The specimen is loaded in tension or compression, inducing shear stresses in the specimen's mid-plane and thus shear failure (Robinson and Hodgkinson, 2000). However, since it is asymmetrically shaped, the normal and the shear stiffnesses of the specimen are coupled. Hence, the specimen bends under load (Figure 2.11b)

and fails in a mixed instead of pure shear failure mode (Ehrenstein, 2006). Nevertheless, this specimen type is also used for interlaminar shear creep investigations by applying static tensile or compressive load (Thielicke et al., 1999).

2.2.2 Interlaminar Fracture Toughness

The propagation of an nucleated interlaminar crack is controlled by the materials interlaminar fracture toughness. It is quantified by the critical energy release rate $\mathscr{G}_c$, defining the energy necessary for a particular crack extension. The fracture toughness is analyzed with various standardized test methods, each considering a particular fracture mode: the double cantilever beam test (DCB) for mode I fracture, the end notched flexure test (ENF) for mode II fracture, and the mixed-mode fracture toughness test for the coupled mode-I-mode-II analysis (Hodgkinson, 2000).

The DCB test uses pre-cracked specimens which are loaded such that the crack is opened in normal direction. The pre-crack is usually obtained by

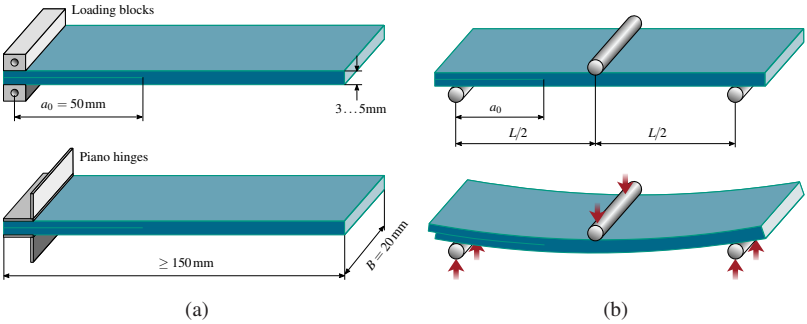

Figure 2.12: Interlaminar fracture toughness tests: (a) double cantilever beam test (DCB) test for mode I fracture, (b) ENF test for mode II fracture (Grellmann and Seidler, 2013)

placing a polytetrafluoroethylene (PTFE) foil between two laminae, which inhibits the consolidation of these laminae in the manufacturing process. Load transmission elements (blocks or hinges) are glued onto the specimen faces in the region of the pre-crack (Figure 2.12a). Thus, the crack propagates along the lamina-interface by mode I fracture as the load transmission elements are moved apart. During the test, the force F and the load point displacement d are recorded and the crack length a is measured optically on the side of the specimen. The accuracy of the optical crack length measurement is crucial since the subsequent computing of the mode I fracture toughness $\mathscr{G}_{\mathrm{Ic}}$ is highly sensitive to the crack growth.

The end notched flexure test (ENF) uses a pre-cracked specimen similar to the DCB test. The specimen is loaded in a three-point-bending mode, as shown in Figure 2.12b, enforcing shear delamination. Since the crack surfaces are pressed onto each other, the crack tip might not be identifiable during the experiment. Hence, in contrast to the DCB test, the end notched flexure test (ENF) test is evaluated only by the analysis the recorded force-displacement-curve for the determination of the mode II fracture initiation toughness $\mathscr{G}_{\mathrm{IIc}}$ (Hodgkinson, 2000).

For both experiments, linear-elastic fracture mechanics are assumed. The critical energy release rate $\mathscr{G}_{\mathrm{c}}$ is computed by the negative ratio of the total energy dΠ dissipated by the fracture to the area cracked by the propagating fracture dA, which is shown in Figure 2.13 for an exemplary DCB test: the highlighted fracture energy dΠ is dissipated by the crack growth $\Delta a = a_4 - a_3$, giving the energy release rate with the specimen width B (Grellmann and Seidler, 2013):

$$\mathscr{G}_{\mathrm{c}} = -\frac{\mathrm{d}\Pi}{\mathrm{d}A} = -\frac{\mathrm{d}\Pi}{B\Delta a}, \qquad \text{in } \tfrac{\mathrm{J}}{\mathrm{m}^2}. \quad (2.1)$$

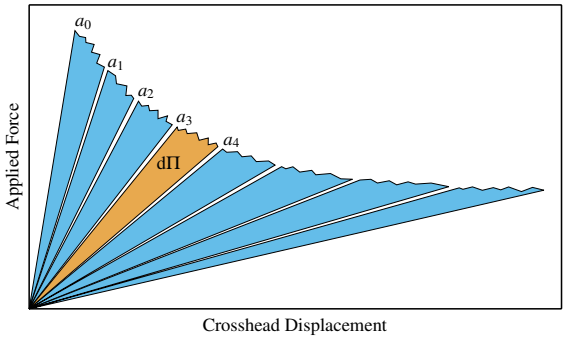

Figure 2.13: Evaluation scheme of a DCB test in the corresponding force displacement curve (Grellmann and Seidler, 2013)

As suggested by ASTM D 5528-13, there are three possibilities of calculating mode I fracture toughness $\mathcal{G}_{\mathrm{Ic}}$ with the acquired data: (i) the modified beam theory (MBT), (ii) the compliance calibration (CC), and (iii) the modified compliance calibration (MCC). The MBT procedure use the simple beam theory and makes a correction of the measured crack length by adding a constant value (Berry, 1963). This method accounts for probable rotations of the DCB specimen's single beams at the delamination front. The CC method assumes the logarithmic system compliance $C = {}^{F}/_{d}$ to be proportional to the logarithmic crack length a and uses the proportionality factor between $\log C$ and $\log a$ to calculate the fracture toughness. This procedure does not consider the actual mechanisms controlling the debonding; however, it can evaluate the experiment with a reasonable accuracy (Berry, 1963). The MCC procedure similarly assumes that the compliance's cube root $\sqrt[3]{C}$ is proportional to the crack length a, but additionally includes the crack length correction achieved by the MBT method (Hodgkinson, 2000). In general, the three data reduction methods result in very similar fracture toughness values which differ by only 3 % (Hodgkinson, 2000). Since none of the methods

is in general superior, their application depend on the fracture behavior of the considered material. Furthermore, all available data reduction methods strongly depend on the necessity to accurately measure the crack propagation during the experiment.

2.3 Modeling Interfaces for Numerical Simulations

Crack propagation within a homogeneous material is widely modeled by means of a cohesive zone formulation along a predefined crack path (Li et al., 2005; Scheider and Brocks, 2003). Moreover, this damage model is also used for the interface failure of any kind, for instance for the intergranular cracking in metal alloys (Simonovski and Cizelj, 2015), or failure of adhesively bonded joints (Jousset and Rachik, 2014; Hu et al., 2015). Consequently, cohesive zone models are also a suitable tool for modeling both fiber-matrix interfaces (Rodríguez et al., 2012; Naya et al., 2016) and interlaminar debonding (Ridha et al., 2014).

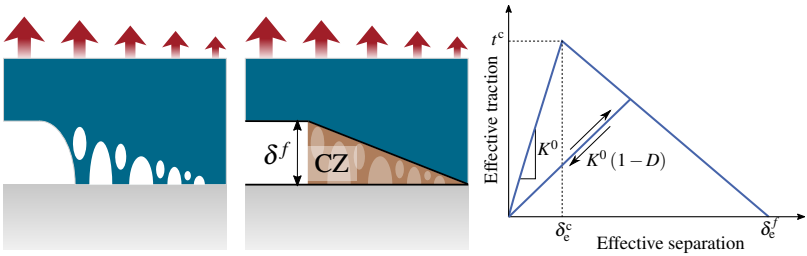

Figure 2.14: Cohesive zone fracture modeling: (a) normal fracture zone on fiber-matrix interface and corresponding separation based cohesive zone (CZ, brown), (b) bi-linear traction-separation law used for cohesive zone formulations (Rodríguez et al., 2012)

Cohesive zone models describe failure as a continuous process of degrading material stiffness. Its application to fiber-matrix interface debonding under normal load is illustrated in Figure 2.14a: in the fiber-near matrix or in the interphase between fiber and matrix, in which the fiber sizing interacts with the matrix, damage initiates as soon as a critical strain or stress is reached, for instances by the nucleation of voids. With increasing strain, the voids grow and merge, decreasing the load carrying capacity until the damaged region finally fails (Figure 2.14a on the left). While the damage increases, the material is assumed to be elastic, i.e. the damage affects the material exclusively by decreasing its stiffness. The cohesive zone model (Figure 2.14a on the right) projects every process taking place in the fiber-near matrix or the interphase onto the interaction of two cohesive surfaces – one belonging to the fiber, one belonging to the matrix (black lines) – which enclose the cohesive zone (CZ). The gradual fracture is modeled by the two surfaces being separated by the separation δ, while being interconnected by the initial stiffness K^0. Thus, the traction $t = K^0 \cdot \delta$ is transferred while the cohesive zone (CZ) is undamaged. Damage initiates when a critical value of the separation (δ^c) or the traction (t^c) is reached. The propagating damage is described by the damage variable D in a range from 0 (no damage) to 1 (complete failure), decreasing the cohesive stiffness $K = K^0(1-D)$ until ultimate failure occurs when the fracture separation δ^f is reached. The behavior of the cohesive zone is driven by the traction-separation-law, which describes the load carrying capacity of the CZ (Kuna, 2008; Jousset and Rachik, 2014). An example is plotted in Figure 2.14b. Here, a linear damage evolution law with respect to the effective traction t_e and the effective separation δ_e is used. Damage initiates at the separation δ_e^c – leading to the critical traction t^c – and ultimate failure is reached at the separation δ_e^f. However, damage evolution can be described in any kind and does not need to be linear (Li et al., 2005).

A cohesive zone formulation can be used for one-dimensional, but also for two- or three-dimensional fracture. That means that the fracture governing separation and the corresponding traction act in one, two, or three spatial directions. Therefore, the traction-separation law is generalized to three dimensions, with the surface separation displacement $\boldsymbol{\delta}$, the stiffness tensor $\boldsymbol{K}$, the cohesive surface normal $\boldsymbol{n}$ and the traction vector $\boldsymbol{t} = \boldsymbol{\sigma n}$ (Kuna, 2008):

$$\boldsymbol{t} = \begin{pmatrix} t_n \\ t_s \\ t_t \end{pmatrix} = \begin{pmatrix} K_{nn} & K_{ns} & K_{nt} \\ & K_{ss} & K_{st} \\ \text{sym.} & & K_{tt} \end{pmatrix} \begin{pmatrix} \delta_n \\ \delta_s \\ \delta_t \end{pmatrix} = \boldsymbol{K\delta} \tag{2.2}$$

Here, the orthonormal basis $\{\boldsymbol{e}_n, \boldsymbol{e}_s, \boldsymbol{e}_t\}$ is used, where $\boldsymbol{e}_n$ is the surface normal direction and $\boldsymbol{e}_s$ and $\boldsymbol{e}_t$ are the surface tangential and transverse directions, and the stiffness tensor $\boldsymbol{K}$ is a function of the damage variable $\boldsymbol{K} = (1-D)\,\boldsymbol{K}^0$. The off-diagonal components K_{ns}, K_{nt}, and K_{st} define the mode interdependency and are zero if no mode coupling is assumed (Abaqus, 2018). For the evolution of the damage variable D, an arbitrary law can be chosen which fits to the material behavior to be modeled. For instance, exponential damage evolution laws well suit the behavior of brittle metals, whereas trapezoidal laws suit ductile polymer behavior (Kuna, 2008).

A separation energy is dissipated while the cohesive surfaces are separated and damage evolves. Using cohesive zones to model cracking, this separation energy represents the fracture toughness $\mathscr{G}_\mathrm{c}$ of the considered material. It is described by the following equations 2.3 with respect to the normal separation (mode I fracture) and tangential separation (mode II fracture), respectively (Kuna, 2008):

$$\Gamma_n^{\mathrm{c}} = \int_0^{\delta_{\mathrm{n}}^f} t(\delta_{\mathrm{n}})\,\mathrm{d}\delta_{\mathrm{n}}, \qquad \Gamma_s^{\mathrm{c}} = \int_0^{\delta_{\mathrm{s}}^f} t(\delta_{\mathrm{s}})\,\mathrm{d}\delta_{\mathrm{s}}. \tag{2.3}$$

In three-dimensional applications of cohesive zones, usually a mixture of the fracture modes rather than one sole mode occurs. Therefore, adapted criteria for both damage initiation and damage propagation have been developed to take the mixed-mode behavior into account (Kuna, 2008). One possible way of handling mixed-mode fraction is using the effective separation and traction $\delta_{\mathrm{e}} = \|\boldsymbol{\delta}\|$ and $t_{\mathrm{e}} = \|\boldsymbol{t}\|$, respectively, which are used for the traction-separation law illustrated in Figure 2.14b. However, in case of anisotropic damage, the damage initiation criterion needs further adaption, for example with a quadratic model, which is shown in Equation 2.4 with respect to the critical separation $\boldsymbol{\delta}^{\mathrm{c}}$ (Hu et al., 2015):

$$\left(\frac{\langle \delta_n \rangle}{\delta_n^{\mathrm{c}}}\right)^2 + \left(\frac{\delta_s}{\delta_s^{\mathrm{c}}}\right)^2 + \left(\frac{\delta_t}{\delta_t^{\mathrm{c}}}\right)^2 = 1. \tag{2.4}$$

Damage initiates when the equation is satisfied. Here, the Macaulay brackets $\langle \bullet \rangle = \max(\bullet, 0)$ indicate that normal compressive displacement does not contribute to damage. In the same way, a damage initiation criterion can be proposed with respect to the critical traction $\boldsymbol{t}^{\mathrm{c}}$ (Hu et al., 2015). Damage propagation criteria can be proposed in a similar way, either by means of the effective separation δ_{e} or the separation energies for the three directions (Hu et al., 2015). Figure 2.15 illustrates a traction-separation law which is applicable for mixed-mode loading scenarios.

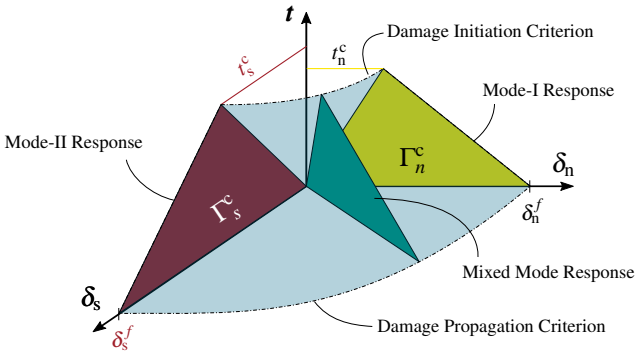

Figure 2.15: Traction-separation principle for cohesive zones applicable for mixed normal-shear-loading (according to Hu et al. (2015))

2.4 Critical Evaluation of the State of Research

The influence of fiber-matrix interfaces on the fracture behavior of a FRP structure is widely accepted to be significant, especially in case of DiCoFRP. However, the interface behavior observed in and the accuracy of the failure parameters obtained by micromechanical experiments are widely disputed in the literature concerning the underlying model approaches (Tandon and Pagano, 1998; Piggott, 1997b), the great susceptibility to the specimen preparation and geometries (Kallas et al., 1992; Zhi et al., 2017), and the limited comparability of the available tests (Piggott, 1997a; Pisanova et al., 2001a,b). Hence, the transferability of the observed interface behavior to real structures appears to be questionable. Moreover, even the basic understanding of the fiber-matrix interface is disputed as contradictory opinions exist regarding the model approach of "adhesion" or "adhesional strength" and their connection to the interfacial parameters obtained by micromechanical tests (Pisanova et al., 2001a).

A general concern is that the existing test methods are not standardized, though the obtained results are highly sensitive to the test parameters, such as the specimen geometry or the test set-up (Zhi et al., 2017; Awal et al., 2011). Especially the specimen geometry and the specimen preparation – with its repercussion on the specimen geometry and the matrix composition – can severely affect the obtained interfacial strength results (Rao et al., 1991; Kallas et al., 1992; Zhi et al., 2017). This leads to a significant scatter in the micromechanical test data, not only in comparison of different experimental campaigns, but also in the results of a single campaign conducted in one laboratory without operator changes (Zinck et al., 2001).

Another reason for the questioning of the described characterization methodologies and their results is the unique composition of the test specimens in terms of their geometry and loading conditions. This set-up leads to stress states and debonding processes which are artificial and hence not comparable to those occurring in a real structure (Piggott, 1997a). A significant difference becomes clear when the fracture of a DiCoFRP is compared to the fracture of a single-fiber micro-composite: in DiCoFRP, the damage of both matrix and fiber-matrix interface initiates at the fiber tips and propagates progressively by merging micro-cracks (Curtis et al., 1978; Takahashi and Choi, 1991) and along the interface, respectively (Sato et al., 1984, 1991). The micromechanical test methods, on the other hand, lead to debonding onsets near the beginning of load transmission, which is the entry point of the fiber into the matrix regarding the microbond or the pull-out test (Piggott and Xiong, 1994), or close to the fiber loading face in a push-out test (Chandra and Ananth, 1995). This peculiarity of the described micromechanical tests is caused by the centro-symmetric system they create, in which the matrix surrounds the centric fiber (Piggott, 1997a). This centro-symmetry can furthermore lead to the paradox that the interface appears to be stronger than the embedding matrix. This can be explained by the failure mode of most

polymers, which do not fail in shear, but due to tension in 45° to the shear direction. Hence, matrix failure in a centro-symmetric set-up requires 45° failure cones around the fiber, as illustrated in Figure 2.16.

Since the cone area increases with the distance r from the fiber proportionally with r^3 and the shear stress decreases with the inverse distance $1/r$, matrix failure is inhibited by fourth order and interface failure is enforced. Furthermore, unknown parameters can strongly affect the measured interface strength, such as the normal pressure on the interface prior to testing – due to curing shrinkage or different thermal expansion coefficients of the constituents – and the coefficient of friction, which in turn can be affected by the interface failure. These circumstances can lead to very high mean shear strength values of the interface, which were found to appear eight times higher than the matrix strength (Piggott, 1997b). However, Madhukar and Drzal (1991a,b) showed that such high strength values severely overestimate the interface strength in a real structure by comparing interface parameters resulting from SFFT and from macroscopic tensile tests transverse to the fiber direction. Possible reasons for this overestimation are the assumptions which have to be made to evaluate the experiments, such as the perfect geometry of the specimen in a stress-free initial state, or the homogeneous, linear-elastic constituents.

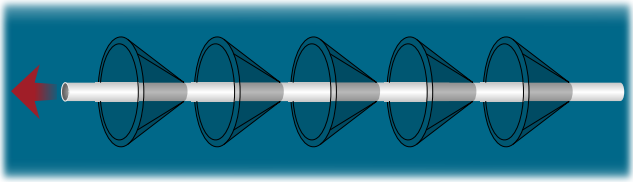

Figure 2.16: Development of tensile matrix failure in a centro-symmetric system (Piggott, 1997b)

Although substantial amount of work has been undertaken to reduce the amount of unknown parameters – for example Mueller et al. (2013) and Greisel et al. (2014) regarding the push-out test, Zhandarov and Mäder (2016) regarding the pull-out test, and Ramirez et al. (2009) and McCarthy et al. (2015) regarding the single-fiber and multi-fiber fragmentation test – major concerns still remain: the centro-symmetric framework of the test set-up on the one hand, and the limitation to use polymers suitable for the required specimen preparation on the other hand. Especially the latter is of major interest if the fiber-matrix interface is analyzed to promote the development of advanced composite structures, since the polymers used here often require high-temperature, compression molding, or fillers for adequate curing (Henning and Moeller, 2011). The studies available in literature mostly use an epoxy resin, which is capable of room-temperature curing and is particularly transparent. However, explicitly highlighted is the influence of the specimen preparation and the polymer composition on the interfacial parameters (Rao et al., 1991; Awal et al., 2011) and that the fundamental test results – concerning the general process of debonding – are not transferable to other matrix systems (Zinck et al., 2001). Applying these test methods to structural resins can therefore be severely difficult or even impossible.

The problems possibly occurring with structural resins can be demonstrated with the UPPH resin: if the UPPH resin used for CoDiCoFRP structures was applied on a single fiber for a microbond test, high-temperature curing would not be successful, since the resin outgases ingredients without additional pressure applied. This behavior was illustrated by an oven-curing trial at IAM-WK, where neat UPPH resin was heated up to curing temperature of 120 °C at atmospheric pressure. The outgassing ingredients make the resin expand and foam heterogeneously, resulting in a very rough shape of the cured polymer with a high amount of voids, as shown in Figure 2.17. A possible way of applying additional pressure onto the curing resin is com-

pression molding. However, resins for SMC structures such as UPPH and the widely used vinyl ester (VE) resin require adaption of their compositions to be capable of neat compression molding. Compression molded and backlit plaques of such adapted resins are shown in Figure 2.18a, where inhomogeneities and cracks can be found. Backlit UPPH with an inserted fiber fixture for a compression molded SFFT specimen is shown in Figure 2.18b (top). Here again, the resin cured very heterogeneously with the inclusion of several voids. Conducting SFFT experiments according to the literature mentioned above seems questionable with such resin curing behavior. Figure 2.18b (bottom) shows a similar trial with a SMC-VE resin adapted for casting. In contrast to the transparent epoxy specimens shown in the literature, the cured resin is milky and unclear in which the fiber can not or only hardly be detected with an optical microscope.

The analysis of the interfacial behavior in a fiber reinforced composite structure under near-application conditions can therefore be problematic with the well-established characterization methods. Only the fiber push-out test seems to be a possible method to determine interfacial properties, since the

Figure 2.17: Neat UPPH resin after curing trial at atmospheric pressure (Anna Trauth, KIT IAM-WK)

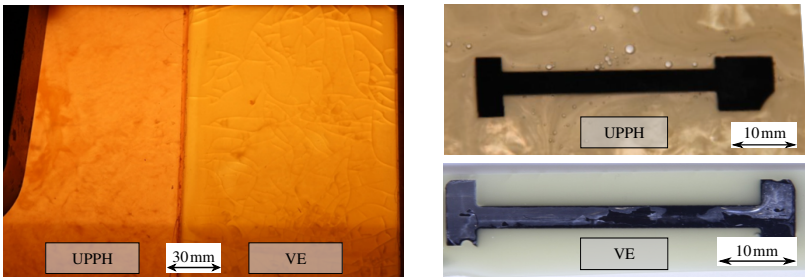

(a) (b)

Figure 2.18: Resin curing trials: (a) compression molded neat resin samples: UPPH and VE, (b) with additional fiber fixture for SFFT: compression molded UPPH resin (top) and adapted VE casting resin (bottom)

corresponding samples can be prepared out of a real structural component. However, since the test requires aligned fibers, its execution and evaluation can be difficult for DiCoFRP. Nevertheless, the centro-symmetric framework and the unknowns arising from the surrounding microstructure still remain.

Especially the influence of the microstructure on the onset and the propagation of the interface debonding is not examined by the established test methods. As Mishnaevsky Jr and Brøndsted (2009) pointed out, the damage initiation in a fiber-polymer-composite is driven by fracture events which are governed by meso-scale rather than micro-scale mechanisms. This means that the interactions between the constituents have to be considered with respect to the fiber-matrix-distribution, including debonded interfaces and the location and orientation of the micro-cracking of the matrix therein. Consequently, focusing on single-fiber composite tests might be insufficient for examining the interfacial behavior relevant in a real structure. Furthermore, since the centro-symmetric experiments mainly apply shear forces on the specimens yet real-life applications create multiaxial stresses in a composite's microstructure, models fitted to such experiments might even be misleading.

A novel test method – for DiCoFRP first proposed by Fliegener et al. (2017) and thoroughly described and carried out in the following chapters – might provide the opportunity to analyze the fiber-matrix interface with respect to the local mesostructure. The methodology involves a tensile test on a mesoscopic test specimen, which has a cross-sectional area of approximately $A \approx 100\,\mu\text{m} \times 200\,\mu\text{m}$ and contains few hundred fibers. The loaded specimen is therefore subject to fracture of several kinds: interfacial debonding and matrix cracking, but also fiber pull-out events can occur. Each experiment is evaluated by means of numerical analyses of an exact model of the physical specimen. Hence, a meso-scale validation of the material models for the composite constituents is possible, as well.

3 Experimental Investigations on Interface Characteristics

As described in the sections above, interfaces in fiber reinforced polymers can be examined on different scales: (i) on the molecular scale regarding the chemical fiber-matrix bonding, (ii) on the microscale regarding the mechanical fiber-matrix bonding, (iii) on the mesoscale with respect to micro cracking, and (iv) on the macroscale regarding delamination. Considering the intended application of the obtained results in design and simulation methods for CoDiCoFRP, the experimental investigation of the behavior of composite interfaces covers three scales:

1. the microscale, considering single fiber-matrix interface failure, only using ideal or close to ideal specimen geometries,

2. the mesoscale, considering multiple interface and matrix failure and also accounting for interaction effects, and

3. the macroscale, considering the failure of lamina interfaces, involving large amounts of fiber-matrix interface failures.

The investigation focuses neither on a specific fiber-matrix-system, nor on the basic principles dominating interface failure. Instead, test methods which are applicable for CoDiCoFRP related material compositions are developed and established. Following a combined experimental-numerical

approach, the experiments are not only conducted physically, but also modeled numerically by finite element (FE) simulations, which help to assess and to interpret the observations from the physical experiments. While the numerical modeling is addressed in Chapter 4, the physical experiments and their results are described in the following sections.

3.1 Characterization Methods

The three material scales of interest mentioned above are analyzed separately with three different experiments:

1. the single-fiber microbond test,
2. the multi-fiber tensile test, and
3. interlaminar fracture toughness tests in mode I and mode II.

The specimens used for these experiments consist of materials used by GRK 2078 for the development of CoDiCoFRP structures. Since the microbond test requires unique specimens, it is carried out with a thermoplastic droplet applied on a glass fiber. The specimens for the multi-fiber tensile test are extracted from glass fiber reinforced unsaturated polyester polyurethane hybrid (UPPH) plaques manufactured by a sheet molding compound (SMC) process, while the specimens for the fracture toughness tests are extracted from unidirectional thermoplastic plaques, manufactured in an automated tape laying (ATL) and subsequent consolidation process.

3.1.1 Single-Fiber Microbond Test

The microbond test is carried out at Fraunhofer IWM using a custom made test set-up. The specimens consist of a droplet of the clear polypropylene

(PP) SABIC PP 579S applied on a PPG TufRov 4575 E-glass fiber, which features a nominal diameter of 17 µm and a sizing suitable for PP.

Specimen Preparation

The preparation of the microbond specimens is a two-step process: (i) dosing of the polymer amount necessary for the droplet, and (ii) applying and shaping the polymer droplet onto the fiber. Both steps require a polymer melt. Hence a heat treatment of the polymer is necessary and inevitable.

Since the polymer amount of a single droplet is very low, it needs to be dosed very accurately. The dosing is realized by means of a fiber melt-spinning process, as sketched in Figure 3.1 with a black-colored PP. Within this process, the raw polymer granulate is melted on a heat plate and a fiber is manually spun out of the polymer melt (Figure 3.1a). The obtained polymeric fiber is subsequently stretched until a diameter of approximately 150 µm is

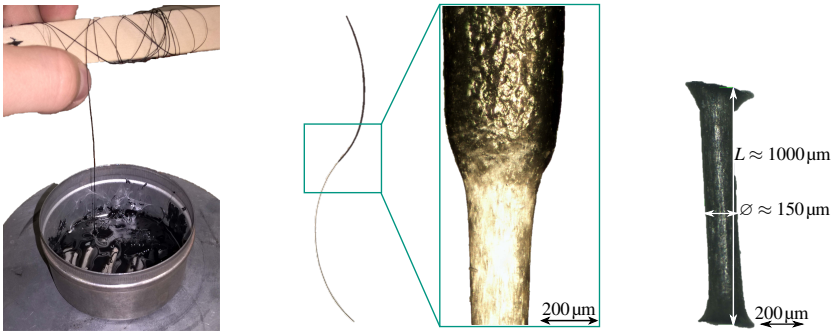

Figure 3.1: Microbond specimen preparation - dosing of the polymer: (a) manufacturing of a polymer fiber by manual melt spinning, (b) stretching the polymer fiber to diameter of approximately 150 µm, (c) cutting the polymer fiber into short pieces of 1 mm

reached (Figure 3.1b). Finally, the stretched PP fiber is cut to fragments with a length of approximately 1000 µm, each providing the polymer amount necessary for a single droplet (Figure 3.1c).

In the second step, the polymer fragments are attached to the fiber. For this purpose, a single glass fiber is clamped on a fiber fixture under light tension and a polymer fiber fragment is attached to it. The fixture including the fiber and the polymer is transferred into a convection oven, pre-heated to 205 °C. The glass fiber is oriented upright in the oven to achieve axially symmetric droplet shapes. The polymer melts inside the oven within 5 min and creates a droplet around the glass fiber. Its shape depends on the surface energy and viscosity of the polymer. Specimens are prepared within two different environments: in air and in an inert gas atmosphere. For this purpose, the oven is flushed with argon. To reduce temperature gradients inside the oven, a pipe spool located within the oven pre-heats the inflowing gas.

Test Procedure

The test is carried out by means of a set-up designed specifically for this test and mounted on a BOSE electro-magnetic universal test machine. The test set-up illustrated in Figure 3.2 consists of two parts: one part pins the fiber and another part shears the droplet off. A perforated stainless steel plate with a 60 µm diameter hole is used as a circular knife edge stripping the droplet off the fiber. It is mounted to the machine's crosshead. The specimen is fed through the perforated steel plate with the droplet facing upwards. The specimen fiber is glued onto a composite plate, which is attached via an adapter to a load cell. That composite plate remains free to rotate to compensate fiber misalignment and an offset between the fiber fixation and the knife center. However, since the compensation of a misaligned fiber

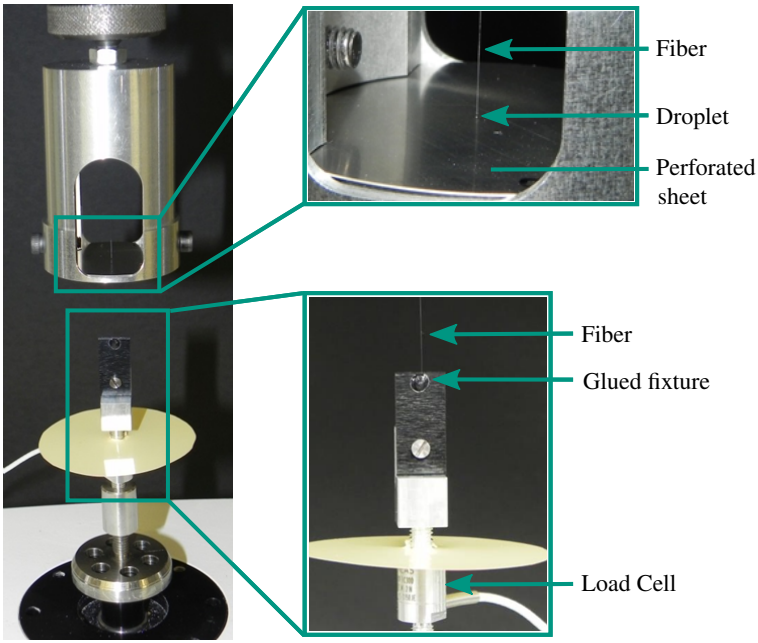

Figure 3.2: Microbond test set-up with attached specimen

and the compensation of a fiber offset are coupled, a total, simultaneous compensation of both misalignment and offset cannot be achieved. Therefore, a minimum distance of few 10 mm between the fiber pinning point and the perforated steel sheet must be retained to minimize the eccentric shearing on the droplet.

Every specimen is microscopically measured prior to testing, concerning the droplet diameter, the droplet length which equals the embedded length l_e, and the fiber diameter D_f (see also Figure 2.4da). The experiment is conducted with a constant crosshead displacement rate of $\dot{d} = 1\,\mu m/s$. The time, the crosshead displacement d, and the applied force F are recorded

continuously. The experiment is evaluated regarding the mean ultimate shear strength $\bar{\tau}_{\mathrm{ult}}$, which is the averaged strength over the embedded length l_{e}, computed as:

$$\bar{\tau}_{ult} = \frac{F_{\max}}{\pi \cdot D_{\mathrm{f}} \cdot l_{\mathrm{e}}} \qquad \text{in MPa.} \quad (3.1)$$

3.1.2 Multi-Fiber Tensile Test

The multi-fiber tensile test allows to investigate the fiber-matrix interface behavior while considering the microstructure of a material, specifically the local fiber volume fraction V_{f}, the fiber distribution or agglomeration, and the fiber orientation distribution. This is achieved by preparing tensile test specimens featuring a cross-sectional area of $A \approx 100\,\mu\mathrm{m} \times 200\,\mu\mathrm{m}$ out of the real material. The evaluation of the experiment and the extraction of the interfacial parameters is achieved with finite element simulations. To do so, the specimen's gauge length including all fibers is precisely modeled. Using a reverse engineering approach, the interface properties are adjusted to fit the numerical force-displacement curve and the numerical fracture modes to the force-displacement curve and the fracture modes of the physical experiment. The modeling is described in detail in Section 4.2.2. The experiments are conducted on a glass fiber (MultiStar 272 by Johns Manville, chopped to a length of 25.4 mm) reinforced UPPH resin, manufactured in a SMC process and compression molded to plaques at Fraunhofer ICT by David Bücheler (Bücheler, 2018). The plaques were compression molded with limited material flow, which results in a random fiber orientation distribution and thus a nea-isotropic in-plane material behavior on the macroscale. The plaques have a mean fiber volume fraction of $V_{\mathrm{f}} \approx 23\,\%$. The reader is referred to the doctoral thesis by Bücheler (2018) for details on the manufacturing process

and its effects on the microstructure and to the doctoral thesis by Trauth (2018) for a profound examination of the macroscopic material behavior.

Specimen Preparation

The specimens used for the multi-fiber tensile test are extracted directly from SMC plaques provided by Bücheler (2018). The process of the specimen extraction from the plaque is illustrated in Figure 3.3 and consists of four steps: (a) a small plate with a manageable size of approximately 50 mm × 50 mm is extracted from the plaque and (b) transversely sliced into thin stripes with a thickness of 1 mm. (c) Using materialography machinery, the cross-sectional faces of the stripes are carefully sanded and polished to obtain smooth sur-

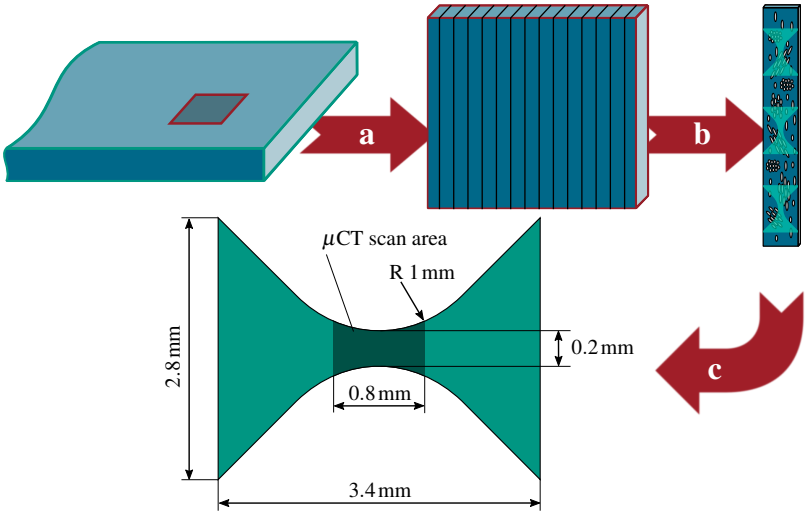

Figure 3.3: Multi-fiber specimen preparation: (a) extracting a planar plate (red contour, $50 \times 50\,\mathrm{mm}^2$) from the structure of interest (green contour), (b) slicing cross-sectional stripes and polishing their surfaces, reducing the thickness to 100 µm (black contour), (c) machining final contour (green filling)

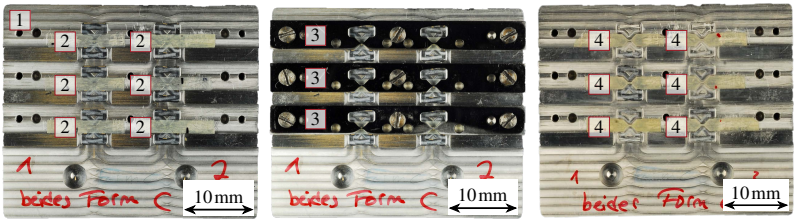

(a) (b) (c)

Figure 3.4: CNC-machining of the final specimen contour: (a) machining fixture [1] with six sprecimen stripes [2] prior to machining, (b) with mounted holding clamps [3], (c) stripes with final contour [4] after machining

faces and to avoid material damage within the stripes. The polishing process is repeated until a stripe thickness of approximately 100 µm is reached. Finally, (d) the stripes are cut to their designated contour. Therefor, the stripes are attached onto a fixture and are cut by means of CNC-machining with a diamond coated mounted point. During the machining, a polished holding clamp compresses the specimens and thus reduces vibrations which can lead to microscopic damage. A machining fixture with attached stripes

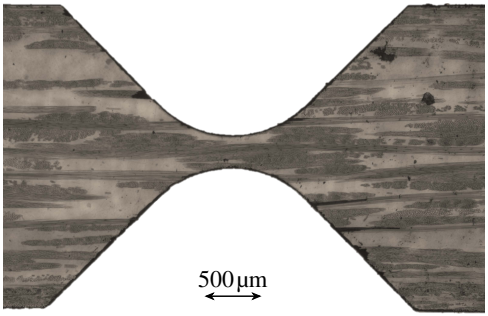

Figure 3.5: Final multi-fiber tensile test specimen

is shown in Figure 3.4 prior to machining (a), with mounted holding clamp (b), and after machining (c).

After machining the final contour, the specimens are thoroughly analyzed with an optical microscope regarding damage of any kind initiated by the preparation process. If no irreversible deformation or fracture can be detected, the specimen's thickness and its width in the gauge length is measured. An example is shown in Figure 3.5.

Test Procedure

The multi-fiber tensile test is conducted like a standard tensile test, yet miniaturized to suit the small scale. Within the test set-up shown in Figure 3.6, which is based on the work of Kennerknecht (2014), the specimen is clamped in dove tail specimen holders (2), where one holder is pinned via a load cell (3) and the other holder is attached to a piezo actuator (4) and a linear motor (5), which apply the loading displacement on the specimen. During the clamping procedure, a pre-load of 5 mN is applied on the specimen. Since

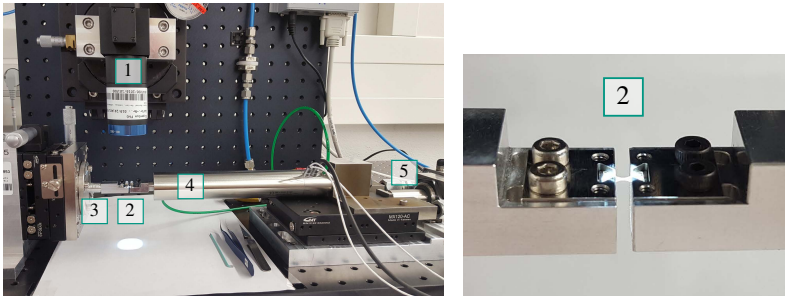

(a) (b)

Figure 3.6: Multi-fiber tensile test set-up: (a) equipment: 1. microscope camera, 2. specimen fixtures, 3. load cell, 4. piezo actuator, 5. linear motor, (b) close-up of the fixtures with a specimen

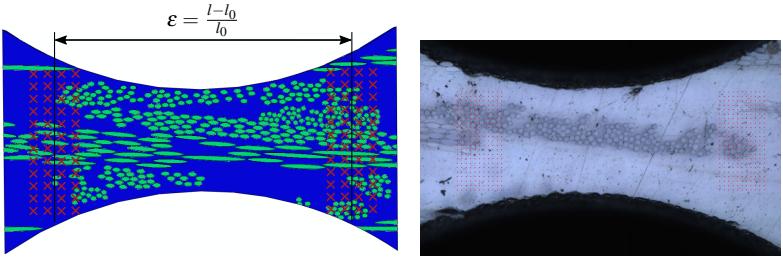

(a) (b)

Figure 3.7: Strain measurement with virtual strain gauge *Matlab* plug-in by Senn and Eberl (2018): (a) strain is calculated with the displacements of two grid fields, (b) application on a specimen

the analyzed specimens are very sensitive, strain cannot be measured tactile on the specimen. Instead, a camera system (1) mounted above the specimen records the specimen during testing for subsequent analyzes. The applied displacement rate is $\dot{d} = 1\,\mu m/s$, the camera shutter frequency is 1 Hz and the time and force are continuously recorded.

The post-processing of the specimen's strain is done by means of a *Matlab* plug-in developed by Senn and Eberl (2018), using digital image correlation (DIC). Instead of the widely used speckle pattern, this DIC method uses the native structured contrast of the material caused by the microstructure. The *Matlab* tool serves as a virtual strain gauge applied onto the specimen. This principle is illustrated in Figure 3.7a: a grid field (red) is positioned on either end of the specimen. The grid fields follow their dedicated position on the specimen throughout all the pictures taken by tracking the specimen's microstructure – here, the green fibers in the

blue matrix. With the displacements of the grid fields, the one-dimensional engineering strain ε can be computed as:

$$\varepsilon = \frac{l - l_0}{l_0}, \tag{3.2}$$

with the initial distance between the fields (i.e. initial strain gauge length) l_0 and the current field distance (current strain gauge length) l. An example featuring a real specimen is shown in Figure 3.7b, where the grid fields are illustrated by red dots.

Additional experiments supporting the multi-fiber tensile test

An exact numerical 1:1-model of the multi-fiber tensile test specimen for enhanced test evaluation requires knowledge in excess of the recorded force-strain relationship. Especially two topics are of major interest: (i) the yield and fracture behavior of the matrix and (ii) the exact position and direction of each fiber within the gauge section. The former is gained by small dovetail tensile tests of neat UPPH resin, whereas the latter is gained by micro-computed tomography (μCT) scanning of each specimen. This μCT measurement is provided by Pascal Pinter (Pinter, 2018).

The UPPH resin has not been developed for neat use and neat plaques for testing purposes cannot be manufactured without further adaption of the resin recipe. Therefore, the resin manufacturer Aliancys Quality Resins provided compression molded neat polymer plaques with an adapted UPPH recipe. The tensile test is conducted on small dovetail specimens according to Figure 3.8, which feature a cross-sectional area of approximately $A \approx 3\,\mathrm{mm} \times 2\,\mathrm{mm}$. The load is applied on the specimen via dovetail-shaped specimen heads with a constant crosshead displacement rate of $\dot{d} = 0.5\,\mathrm{mm/min}$. The strain is measured with a tactile strain gauge throughout the test.

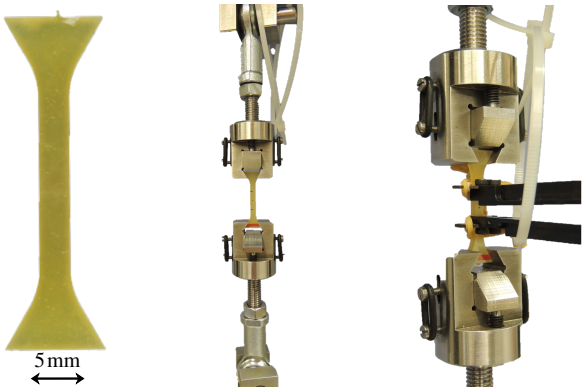

Figure 3.8: Dovetail tensile test of neat UPPH: (c) dovetail tensile test specimen, (b) test set-up in an universal testing machine, (c) tactile strain gauge applied on specimen

μCT scanning for the geometric specimen analysis is performed at the Institute for Applied Materials – Materials Science (IAM-WK) at the Karlsruhe Institute of Technology (KIT) by Pascal Pinter and Ludwig Schöttl with their tools and algorithm provided by Pinter (2018). A fiber tracking algorithm post-processing the μCT data distinguishes the fibers from the matrix and tracks every single fiber. It gives an array of the voxel coordinates of each fiber's centerline. Since the voxel-based μCT can only result in discrete voxel coordinates and the specimen modeling requires a smooth

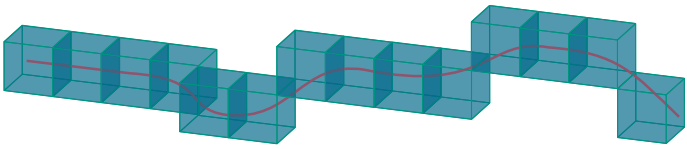

Figure 3.9: Schematic fiber tracking in μCT scan: tracked fiber voxels with a B-spline fit for the fiber's medial axis (Pinter, 2018)

fiber course, the tracked fiber data has to be transformed into a continuous description of the fiber path. To obtain a continuous description of the fiber path, a B-spline is fitted to the voxel coordinates. This approach is schematically illustrated in Figure 3.9.

3.1.3 Interlaminar Fracture Toughness Test[1]

Continuous fiber reinforced thermoplastic tapes can be used to locally reinforce LFT structures. For this purpose, the tapes need to be consolidated to their designated shape prior to co-molding with the LFT material. This consolidation process consists of three steps: (i) stacking the tapes to a lay-up with a predefined shape and tape orientation sequence, (ii) heating the lay-up to a polymer-specific processing temperature, and (iii) compression molding of the lay-up to join the individual tapes. Since the consolidation creates the interaction between the tape layers, its process parameters need to be chosen carefully. This section describes the determination of the interlaminar fracture toughness in mode I and mode II with respect to different consolidation process parameters, specifically the consolidation temperature and the consolidation pressure. The investigated material is Ultratape B3WG12 provided by BASF, which is a continuous glass fiber reinforced polyamide-6 (poly-caprolactam, PA6) with a fiber volume fraction of $V_\mathrm{f} = 40\,\%$ and a thickness of 0.25 mm. The manufacturing of the thermoplastic sample material and the experimental study on the interlaminar fracture toughness has been conducted at the University of Western Ontario and the Fraunhofer Project Centre for Composites Research at Western, both at London, ON, Canada.

[1] This section as well as the corresponding results in Section 3.2.3 are based on the proceedings Schober et al. (2017a,b)

Plaque and Specimen Manufacturing

The laying and consolidation of the thermoplastic tapes has been performed with industry-scale machinery at the Fraunhofer Project Centre. A Fiberforge Relay 1000 automated tape laying machine shown in Figure 3.10a is used for the stack preparation. The raw tape material delivered on spools is fed from its racks (position 1) to the cutting and laying unit (2). The unit cuts the tape to the desired length and places it onto a vacuum table (3), which can slide in its planar directions and rotate around its vertical axis, allowing an arbitrary shape and alignment sequence of the tape lay-up. An array of ultrasonic spot welders presses and joins a newly placed tape onto its subjacent tapes, while the vacuum table keeps the lay-up in place. For the fracture toughness investigations, a stack of 20 tape layers is laid. For the preparation of the pre-crack, a 25 µm thick and 100 mm wide film of PTFE is placed between the 10^{th} and 11^{th} layer, preventing the layers to merge. The finished lay-up

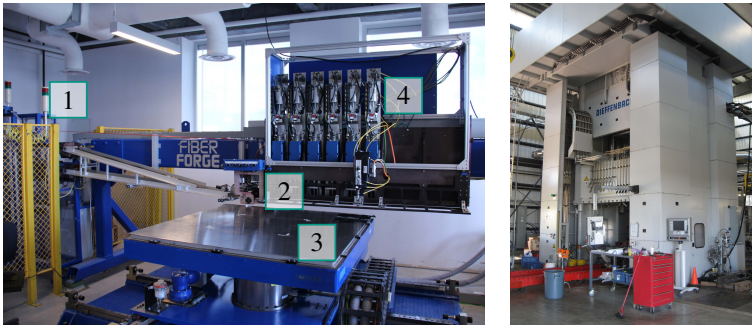

(a) (b)

Figure 3.10: Thermoplastic tape laying and consolidation process: (a) ATL machine Fiberforge Relay 1000: 1. tape feeder, 2. cutting and laying unit, 3. movable and rotatable vacuum table, 4. spot welder array, (b) hydraulic press used for compression molding

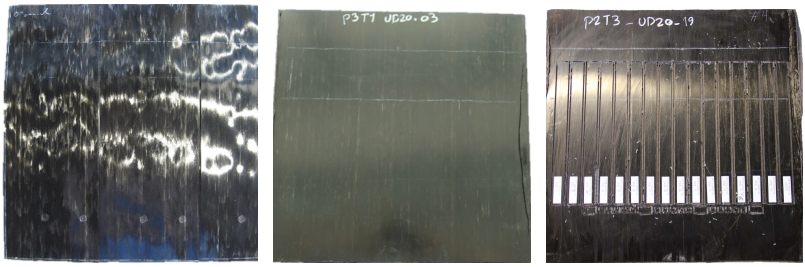

(a) (b) (c)

Figure 3.11: Sample manufacturing steps: (a) tape lay-up with PTFE sheet, (b) consolidated plaque, (c) CNC-machined specimen in consolidated plaque

with the indicated position of the PTFE film is shown in Figure 3.11a. In order to prevent influences by the ultrasonic welding spots – such as polymer degradation and a reduced local matrix volume fraction – the welders are deactivated in the designated specimen area. Prior to consolidation, the tape lay-ups are dried at 100 °C for 8 h.

The consolidation starts with the heating of the lay-up. Therefor, it is placed between two pre-heated aluminum sheets, transferred into a convection oven and heated for 25 min. Subsequently, the aluminum-lay-up stack is transferred into a shear-edge mold, which is mounted in a 30 000 kN hydraulic press (Figure 3.10b) and heated to 90 °C, and compression molded for 120 s. The oven temperature is varied from 275 °C to 285 °C and 295 °C in order to reach lay-up temperatures of 260 °C, 270 °C, and 280 °C, respectively, while the heating time is kept constant. The compression force is varied from 500 kN to 750 kN and 1000 kN, resulting in a cavity pressure of 24 bar, 36 bar, and 48 bar, respectively. Full fractional consolidation parameter variations are conducted to investigate their influence on the fracture toughness. An exemplary consolidated plaque is shown in Figure 3.11b, on which the position of the PTFE film is indicated by white lines.

The fracture toughness specimens are extracted from the plaques by CNC-milling. They are 250 mm long, $B = 20$ mm wide and between 5.0 mm and 5.3 mm thick, depending on the consolidation parameters. The specimens are positioned within the plaque so that a 70 mm initial crack remains in the top end of each specimen.

Test Procedure

The interlaminar fracture toughness is analyzed in mode I with the double cantilever beam test (DCB) according to ASTM D 5528 and in mode II with the end notched flexure test (ENF) according to DIN EN 6034. All tested specimens are dried prior to testing at 100 °C for 24 h.

The experiment is conducted with a MTS universal testing machine; the experimental set-up is shown in Figure 3.12. For the DCB tests, stainless steel hinges are glued onto the specimen at the pre-cracked end, resulting in an initial crack length of 50 mm between the crack tip and the load line. A

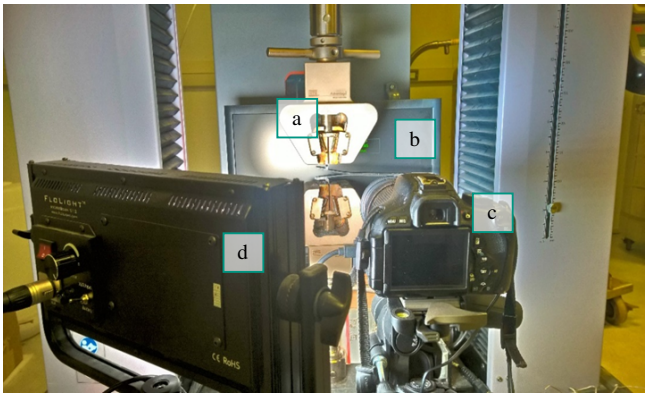

Figure 3.12: Test set-up for fracture toughness experiments: (a) grippers with fixed DCB specimen, (b) computer screen displaying current crosshead displacement, (c) auto-shutter camera, (d) flood light

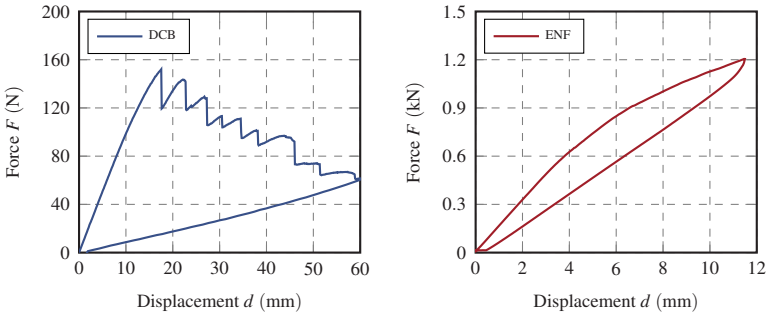

(a) (b)

Figure 3.13: Typical force-displacement curves $F(d)$: (a) double cantilever beam test, (b) end notched flexure test

loaded specimen is shown in Figure 3.12 at location (a). During the test, the propagating fracture is recorded by means of a D-SLR camera (c) with an automatic shutter release frequency of 0.2 Hz. A computer screen behind the specimen (b) displays the current crosshead displacement to synchronize the images to the recorded force and crosshead displacement data. An additional flood light (d) provides the necessary lighting for the crack front tracking. Prior to the actual fracture toughness test, the specimen is initially loaded until the crack starts to propagate in order to create a sharp crack-tip. The test is conducted under displacement control with a crosshead displacement rate of $\dot{d} = 2\,{}^{mm}/_{min}$ until a total displacement of 60 mm is reached, which aims a total crack length of 100 mm at the end of the test. Finally, the specimen is unloaded with a reverse crosshead displacement rate of $\dot{d} = -20\,{}^{mm}/_{min}$. A typical force-displacement curve of the DCB test is plotted in Figure 3.13a.

The crack length is measured by post-processing the taken images with the *ImageJ* plug-in *MTrackJ*, as schematically shown in Figure 3.14. The specimen displacement is tracked in three ways: (a) the point of load

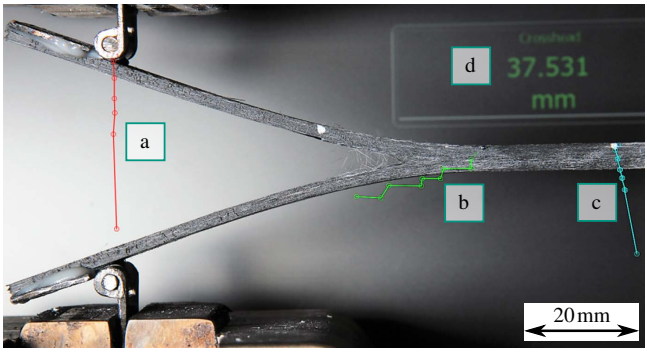

Figure 3.14: Experiment post-processing scheme with *ImageJ* - *MTrackJ*: (a) tracking of the load-transmission point, (b) tracking of the crack-tip, (c) tracking of the longitudinal specimen displacement, (d) current crosshead displacement

transmission from the crosshead into the specimen is tracked, (b) the local crack tip on the specimen side is tracked, and (c) the longitudinal specimen displacement due to the crack opening is tracked. With the tracked data, the current crack length is computed and referred to the current crosshead displacement (d). The critical energy release rate for mode I fracture is the computed according to Equation 2.1:

$$\mathscr{G}_{\mathrm{Ic}} = -\frac{\mathrm{d}\Pi}{B\,\Delta a} \tag{3.3}$$

$$\mathscr{G}_{\mathrm{Ic}} = \frac{\frac{1}{2}F_1 d_1 + \int_{d_1}^{d_2} F(d)\,\mathrm{d}d - \frac{1}{2}F_2 d_2}{B\,(a_2 - a_1)}, \qquad \text{in } \frac{\mathrm{J}}{\mathrm{m}^2}, \tag{3.4}$$

for a crack propagating from a_1 to a_2, with the corresponding forces F_1 and F_2, the corresponding crosshead displacements d_1 and d_2, the force-displacement curve $F(d)$ and specimen width B. This approach is identical to the one shown in Figure 2.13b (Grellmann and Seidler, 2013).

The ENF test uses the same experimental set-up as the DCB test, however, with a 3-point beding test rig featuring a span width of $L = 100\,\text{mm}$. The test is conducted with a loading crosshead displacement rate of $\dot{d} = 2\,{}^{mm}/_{min}$ and an unloading crosshead displacement rate of $\dot{d} = -5\,{}^{mm}/_{min}$. A typical force-displacement curve of the ENF test is plotted in Figure 3.13b. The specimens have been initially loaded in mode I to create a sharp crack tip and are cut to achieve a initial crack length of $a_0 = 35\,\text{mm}$. However, the crack tip is not clearly detectable during the experiment since the crack surfaces are pressed onto each other. Thus, continuous crack propagation measurements are not possible and the fracture toughness cannot be computed according to Equation 2.1. Instead, the ENF test is evaluated by means of the fracture initiation resistance according to DIN EN 6034 with:

$$\mathscr{G}_{\text{IIc}} = \frac{9 \cdot F_{5\%} \cdot d_{5\%} \cdot a_0^2 \cdot 1\,000}{2B \cdot \left(\frac{1}{4}L^2 + 3a_0\right)}, \qquad \text{in } \tfrac{\text{J}}{\text{m}^2}. \quad (3.5)$$

Here, the critical force to initiate the crack propagation is defined by the 5 % deviation of the force-displacement curve from the initial specimen stiffness, described as $F_{5\%}$ with the corresponding crosshead displacement $d_{5\%}$. L is the span width of the 3-point bending test rig and a_0 is the initial crack length in the specimen.

Additional experiments supporting the multi-fiber tensile test

The experimental investigations are accompanied by numerical simulations, which are described in Chapter 4. In order to properly model the physical experiments, the fracture toughness investigation is complemented by a basic characterization of the material's elastic properties. For this purpose, additional plaques with a reduced tape stack consisting of ten layers were manufactured representing half of the double cantilever beam test specimen.

The plaques were manufactured with the consolidation parameters according to Section 3.1.3. Since the lay-up mass is severely reduced, the heating time was reduced to 10 min to reach the aimed lay-up temperature.

The elastic properties of the composites are determined with tensile tests according to ISO 527-5, conducted at angles of 0° and 90° to the fiber direction. The experiments are conducted with a constant crosshead displacement rate of $\dot{d} = 2\,{}^{mm}/_{min}$ and the lateral strain of the specimen is measured by means of a tactile strain gauge. The tests are evaluated by computing the corresponding Young's moduli E_{11} and E_{22}, respectively. Furthermore, the elastic shear behavior is analyzed by means of a V-notched rail shear test according to ASTM D 7078. The corresponding test rig is shown in Figure 3.15 with a mounted specimen, in which the fibers are aligned in the upwards direction. The specimen is loaded by the right grippers with a constant crosshead displacement rate of $\dot{d} = 0.5\,{}^{mm}/_{min}$. A speckle pattern is applied on the specimens, which allows DIC measurements of the

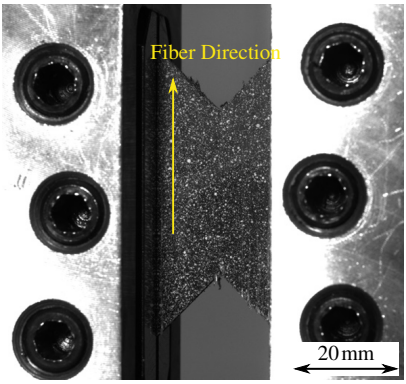

Figure 3.15: V-notched rail shear test according to ASTM D 7078 to investigate the materials shear behavior with speckled specimens for DIC strain measurement

local strains with a dual-camera system. The test is evaluated by computing the shear modulus G_{12}.

3.2 Experimental Results

3.2.1 Single-Fiber Microbond Test

Specimen Preparation

Microbond test specimens were prepared successfully with the procedure described in Section 3.1.1. Selected specimens prepared in pure air atmosphere are shown in Figure 3.16. The droplets are shaped well around the fiber and show only minor asymmetries with respect to the glass fiber and also with respect to their horizontal plane. The globular droplets phase out towards the fiber via so-called menisci with smooth and regular shapes, which extend the droplets slightly in the fiber directions, leading to diameters between 150 µm and 190 µm and lengths between 230 µm and 250 µm. The clear polypropylene remained transparent, however, the droplets are discolored in a slight brown. This coloration can be seen in the meniscus areas, but also in the droplet center, where the fiber shines through. Although the degree

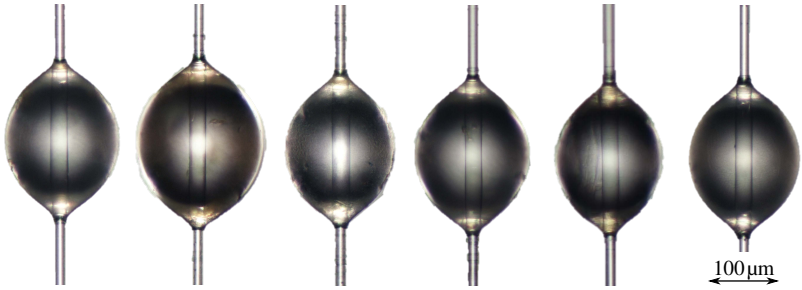

Figure 3.16: Microbond specimens prepared in air atmosphere – specimen numbers from left to right: Air-1 to Air-5, Air-7

of discoloration differs from specimen to specimen, none of the droplets prepared in pure air atmosphere retained the clear transparency of the original PP.

The discoloration of the droplets indicates polymer degradation, which can affect the fiber-matrix interface properties. In order to reduce or to eliminate such effects, the oven used for the specimen preparation is flushed with inert gas during the heating process. Pressurized argon is passed through a metallic spool to pre-heat and blown into the oven with a relative pressure of 2 bar. The resulting atmosphere composition within the oven is measured at room temperature with respect to the oxygen fraction. For this purpose, a specimen preparation process is simulated: the gas is continuously streaming in the opened oven, which is closed at the time 0 sec and remains closed for 300 sec, while the oxygen fraction within the oven is measured. The evolution of the residual oxygen fraction is plotted in Figure 3.17. Originating from a

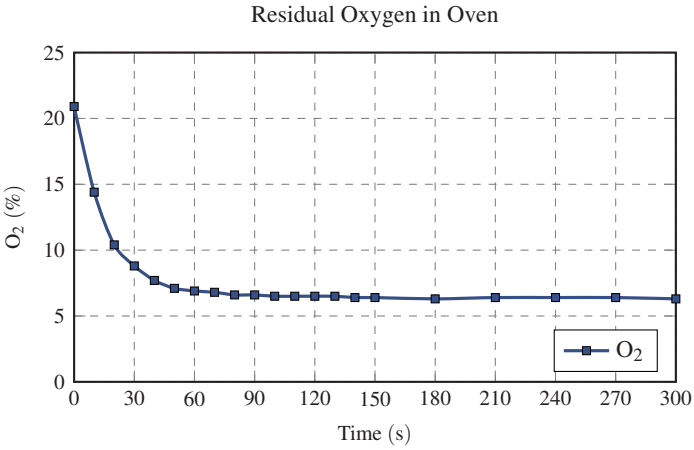

Figure 3.17: Residual oxygen in convection oven flushed with inert gas

normal atmosphere content of 20.9 %, the oxygen fraction decreases rapidly after the oven door is closed. After 30 sec, its fraction is below 9 % and it almost saturates at 6.5 % after 90 sec. The final oxygen fraction after 300 sec is 6.3 %. Throughout the whole specimen preparation time of 300 sec, the mean oxygen fraction is 7.2 %.

Selected microbond specimens prepared in the reduced oxygen atmosphere described above are shown in Figure 3.18. The droplets are well shaped with smooth menisci and limited asymmetries. In general, the droplets prepared with argon are significantly less discolored indicating a lower amount of degradation. While the specimens Ar-8 and Ar-13 in Figure 3.18, for example, show perfectly clear meniscuses, the specimens Ar-4 and Ar-12, however, show a slight degree of discoloration. Nevertheless, the most discolored droplet prepared with inert gas has a clearer transparency than the least discolored droplet prepared in air. Furthermore, the droplets prepared with flushing inert gas are larger regarding both diameter (175 µm to 240 µm) and length (235 µm to 305 µm). The different droplet sizes may be caused by thermal-oxidative degradation of the polymer during the preparation process. However, the reasons may also be found simply in the scatter

Figure 3.18: Microbond specimen prepared with flushing argon – specimen numbers from left to right: Ar-1, Ar-2, Ar-3, Ar-4, Ar-8, Ar-9

of the manual preparation process. A direct analysis of the root cause is not possible at this point. The droplet diameters and lengths are listed in the appendix in Table A.1 regarding the air specimens and in Table A.2 regarding the argon specimens.

Single-Fiber Microbond Test Results

The microbond test is conducted by means of five specimens prepared in air (specimen numbers Air-1 to Air-5) and seven specimens prepared in argon (Ar-1 to Ar-7). The mean shear stress-displacement ($\bar{\tau}(d)$) curves of the Air-specimens feature a proportional increase of the computed means shear stress $\bar{\tau}$ with increasing crosshead displacement d. Failure occurs suddenly at ultimate interfacial shear strength $\bar{\tau}_{\mathrm{ult}}$ between 3 MPa and 4.1 MPa and without prior deviation of the curve and goes along with a significant drop of the transferred shear stress. The sudden failure indicates unstable crack

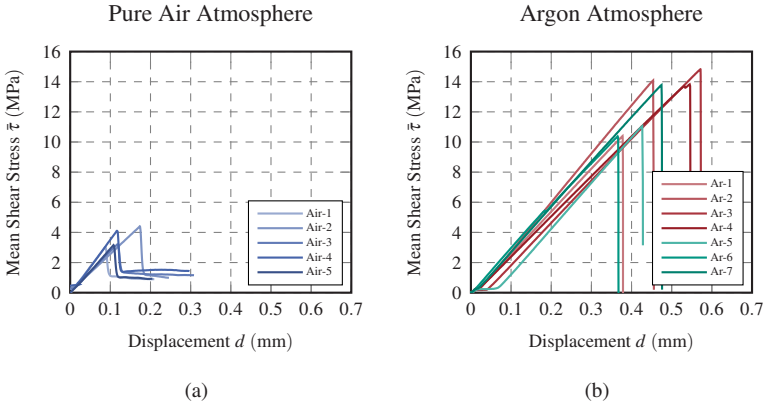

Figure 3.19: Microbond test results – mean interfacial shear stress $\bar{\tau}$ plotted against machine crosshead displacement: (a) specimens prepared in air, (b) specimens prepared in argon

propagation once a crack has nucleated. It is followed by a plateau-like stress state between 1 MPa and 1.5 MPa. The $\bar{\tau}(d)$-curves are plotted in Figure 3.19a.

The specimens prepared in argon in general show a similar initial behavior; the corresponding $\bar{\tau}(d)$-curves are plotted in Figure 3.19b. The interfacial shear stress increases constantly with the increasing crosshead displacement until ultimate failure occurs. Noticeable for few specimens, however, is that the stress increase is divided by a distinct stress plateau after an initial small stress increase at the beginning of the experiment, which is most pronounced for the specimens Ar-3 and Ar-5. In contrast to the specimens prepared in air, the ultimate shear strength $\bar{\tau}_{\mathrm{ult}}$ is much higher with values between 10.4 MPa and 14.8 MPa. At the instant of failure, the fiber springs back due to the elastic energy stored in the fiber. This spring back exceeds the fiber's initial position and thus pushes the droplet far away from its initial bonding zone. Hence, post-failure interfacial stress due to friction is not detectable. Again, the sudden failure indicates that crack nucleation is directly followed by unstable crack propagation. The experimental results are summarized in Table 3.1 with their arithmetic mean values and their standard deviations. The maximum forces F_{max} of the individual specimens and their interfacial shear strengths $\bar{\tau}_{\mathrm{ult}}$ are listed together with the corresponding droplet dimensions in the appendix in Tables A.1 and A.2 regarding air- and argon-preparation, respectively.

Table 3.1: Summary of the microbond test results with respect to the preparation atmosphere

Atmosphere	Mean Value $\bar{\tau}_{\mathrm{ult}}$	Standard Deviation	Variability
Air	3.57 MPa	0.62 MPa	17.4 %
Argon	12.6 MPa	1.93 MPa	15.2 %

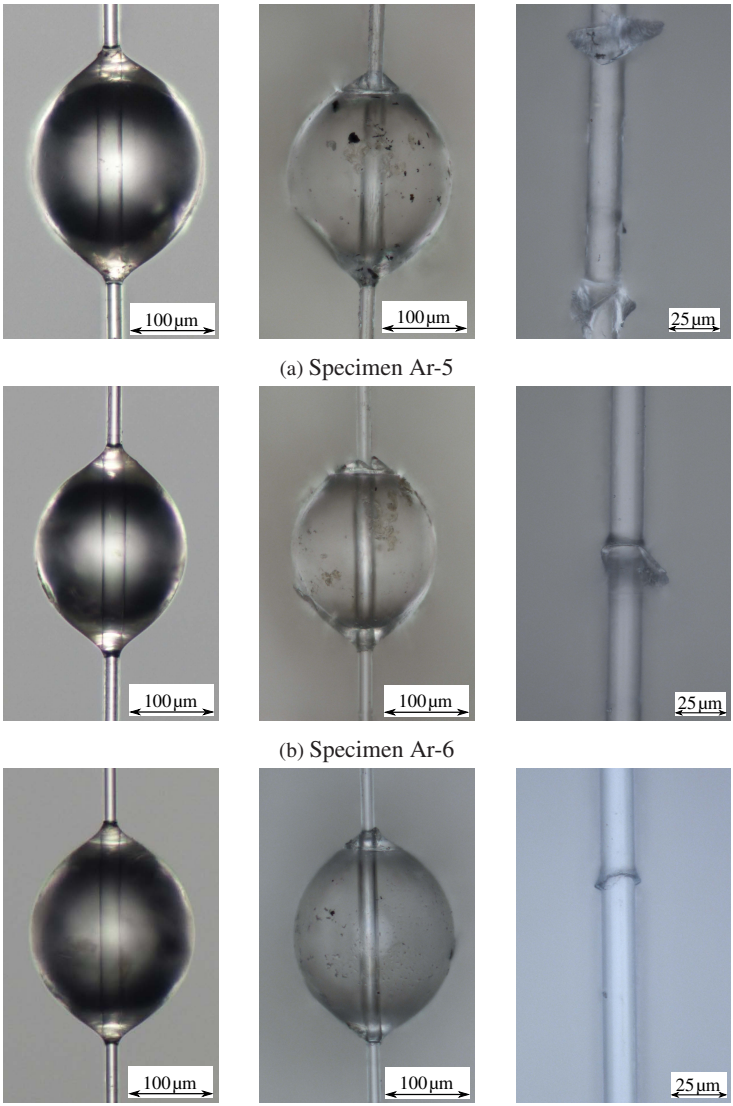

(a) Specimen Ar-5

(b) Specimen Ar-6

(c) Specimen Ar-7

Figure 3.20: Microbond specimens prepared with argon: (left) droplet prior to testing, (middle) droplet after testing, (right) debonded zone after testing

The specimens Ar-5, Ar-6, and Ar-7 have been chosen to be further analyzed as they show a large initial stress plateau, no plateau and an intermediate plateau, respectively. For better distinction, these specimens are plotted green in Figure 3.19b instead of red. Figure 3.20 shows these three specimens in three different stages, each: prior to testing (left), droplet after testing (middle), and the debonded zone of the fiber after testing (right). In all images, the applied force on the droplet is directed downwards. In general, all specimens show almost blank fiber surfaces between the meniscus regions indicating that the specimen failure is governed by the fiber-matrix interface. The droplet of the specimen Ar-5 is considerably asymmetric with respect to the fiber, which is visible both before and after testing. The specimens Ar-6 and Ar-7 show also asymmetric droplets, yet in a lower degree than Ar-5. Comparing each droplet before and after testing, a zone of plastic deformation and damage exists in the upper droplet end, where it was pressed onto the perforated steel sheet. This zone is significantly smaller in Ar-7 compared to the other specimens. Furthermore, an imprint of the sharp steel edge into the polymer is clearly visible in all droplets. In Ar-6, this imprint is horizontal, while its considerably tilted in Ar-5 and slightly tilted in Ar-7. The size of the damaged zone in the droplet corresponds with the amount of polymer residue on the glass fiber, which is almost completely blank in Ar-7. Here, only a small residue of the upper meniscus is detectable. In contrast, Ar-6 and especially Ar-5 show a significant amount of polymer residue of the upper meniscus and of both menisci, respectively. Comparing the stress-displacement curves with the droplets, the imprint angle seem to correlate with initial stress plateau: Ar-6 shows a horizontal imprint and no plateau, Ar-7 a slightly tilted imprint and a short plateau and Ar-5 shows a considerably tilted imprint and an extended plateau. Furthermore, the specimen Ar-7 with the smallest damage zone in the droplet yields the highest

shear strength with 13.8 MPa, compared to 11.1 MPa (Ar-5) and 10.4 MPa (Ar-6).

3.2.2 Multi-Fiber Tensile Test[2]

The main focus regarding the multi-fiber tensile test results lies on the fracture behavior of the individual specimens. However, the results of the additional experiments analyzing the mechanical behavior of the neat UPPH dovetail tensile tests are presented at first.

Neat UPPH Test

The dovetail tensile tests of the neat UPPH plaque result in a stress-strain response with insignificant variation. The stress-strain curves are plotted in Figure 3.8 and the resulting mechanical parameters are listed in Table 3.2. The results of the individual specimens are listed in Table A.3 in Appendix A.2. After an initial setting of the specimens, the stresses in the eleven investigated specimens rise in a narrow corridor as the strain increases, resulting in a Young's modulus of 3171 MPa with a slight scatter of $\pm 1.6\,\%$. Non-linear deformation starts at a total strain of approximately 1 % and increases steadily. The stresses increase constantly until the tensile strength with an average of 78.3 MPa is reached. Final failure occurs in a brittle mode

Table 3.2: Summary of neat UPPH dovetail tensile test results

	Mean Value	Standard Deviation	Variability
Young's Modulus	3171 MPa	51 MPa	1.6 %
Tensile Strength	78.3 MPa	3.5 MPa	4.4 %

[2] The presented results have been obtained within the scope of the Master's Thesis by Dittmann (2018) supervised by the author

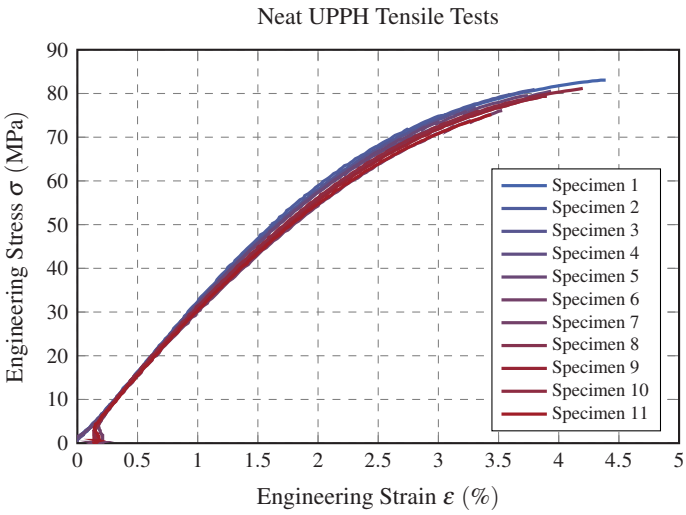

Figure 3.21: Dovetail tensile test results of neat UPPH

transversely to the loading direction when the tensile strength is reached. There is no local necking occurring prior to final failure. Figure 3.22 shows the failure mode of selected specimens (3, 4, 10, and 11).

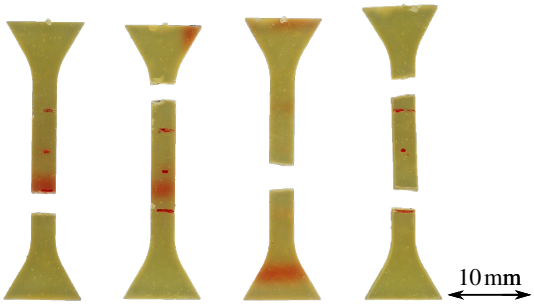

Figure 3.22: Fracture modes dovetail specimens (specimen numbers 3, 4, 10, and 11)

Multi-Fiber Test

The results of the multi-fiber tensile tests are presented for four selected specimens (GF-3, GF-5, GF-6, GF-14) representing the broad variation of the SMC microstructure. Since the specimen thickness cannot directly be adjusted in the polishing procedure, it considerably scatters with thicknesses between 77.6 µm and 129.6 µm. The CNC-machining of the specimen contour, on the other hand, results in much lower scatter, with specimen widths between 291.2 µm and 299.7 µm. The fiber volume fraction V_f of the specimen's gauge lengths – computed by means of μCT measurement – varies between 5.8 % in specimen GF-6 and 26.7 % in GF-3. Typically for SMC materials, the microstructures consist of various fiber bundles, which differ in their size, position, and orientation. Details on the specimens and the corresponding test results are summarized in Table 3.3. The corresponding force-strain curves are plotted in Figure 3.23. None of the curves feature an initially constant force increase. Instead, the force growth decreases with increasing strain. The fracture and thus the further development of the

Table 3.3: Summary of multi-fiber test results

Specimen	Width[1]	Thickness	V_f[2]	E[3]	F_{max}
GF-3	291.39 µm	86.17 µm	26.7 %	25 100 MPa	2.42 N
GF-5	291.24 µm	77.6 µm	18.6 %	12 224 MPa	2.55 N
GF-6	299.72 µm	129.64 µm	5.8 %	5343 MPa	3.22 N
GF-14	292.33 µm	117.34 µm	17.4 %	14 591 MPa	2.05 N

[1] Narrowest specimen width
[2] Fiber volume fraction in the measurement length (approx. 1 mm) measured by μCT scanning
[3] Young's modulus computed with respect to the narrowest specimen width

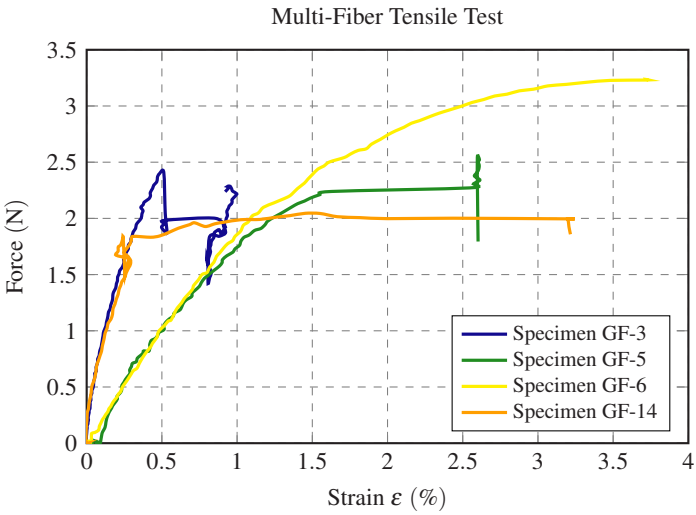

Figure 3.23: Force-strain curves of the multi-fiber tensile tests

force-strain curves strongly depends on the specimen's microstructure and is thoroughly described in the following paragraphs.

The fracture process of the specimen GF-3 is illustrated in Figure 3.24. Here, the strain measurement by the virtual strain gauge is not completely successful, since the fracture crosses the right hand gauge area and thus falsifies the results. For this reason, the fracture is analyzed with respect to the test time instead to the current strain. The pre-load of 1 mN at the beginning of the test at $t = 0\,\text{sec}$ reveals a small micro-crack on the lower specimen edge, which meanders three to four fibers. This micro-crack has propagated and become clearer visible after $t = 89\,\text{sec}$, when it has completely crossed a fiber bundle and stopped at the boundary to the next fiber bundle, which is oriented slightly more longitudinally. Slowly, the crack propagates through this bundle and arrests at a bundle in the middle of the specimen with a strong

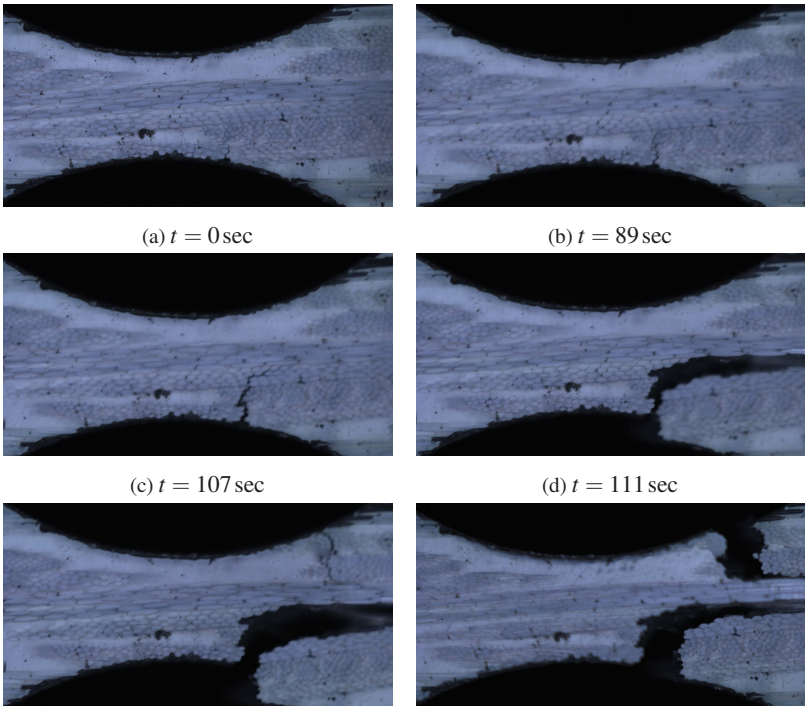

(a) $t = 0\,\text{sec}$ (b) $t = 89\,\text{sec}$

(c) $t = 107\,\text{sec}$ (d) $t = 111\,\text{sec}$

(e) $t = 151\,\text{sec}$ (f) $t = 154\,\text{sec}$

Figure 3.24: Fracture behavior of the specimen GF-3 during testing

longitudinal orientation. At $t = 111\,\text{sec}$, a rapid fracture event takes place when the crack propagates along the longitudinally oriented fiber bundle without penetrating it. This fracture event goes along with a drop of the applied force and divides the strain gauge area. From this point on, the virtual strain gauge does not give correct results any longer. Afterwards, a secondary crack develops opposite to the cracked region in a fiber bundle at the upper specimen edge and propagates via another fiber bundle towards the

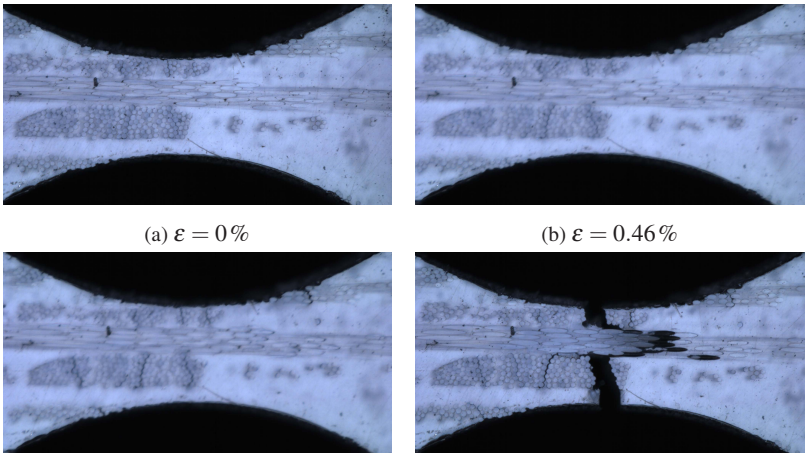

(a) $\varepsilon = 0\,\%$ (b) $\varepsilon = 0.46\,\%$

(c) $\varepsilon = 1.45\,\%$ (d) $\varepsilon = 2.6\,\%$

Figure 3.25: Fracture behavior of the specimen GF-5 during testing

central longitudinally oriented bundle ($t = 151\,\text{sec}$). After $t = 154\,\text{sec}$, final failure occurs in a second rapid fracture event, when the secondary crack propagates around the longitudinal bundle and merges with the first crack.

Specimen GF-5 illustrated in Figure 3.25 is composed similarly to GF-3, with a more longitudinally oriented fiber bundle in the specimen center and bundles oriented completely transversely surrounding it. Multiple cracks initiate in the out-of-plane bundles, both within the specimen and at the specimen edge ($\varepsilon = 1.45\,\%$ and $\varepsilon = 1.45\,\%$). The cracks slowly propagate towards the central, longitudinal bundle. At a strain of $\varepsilon = 1.45\,\%$, two of the initiated cracks merge by propagating around the central, longitudinal bundle, leading to a sudden increase of the measured strain. However, single fibers still bridge the crack surfaces, allowing for a final increase of the applied force before the specimen finally fails. Comparing the cracked bundles at

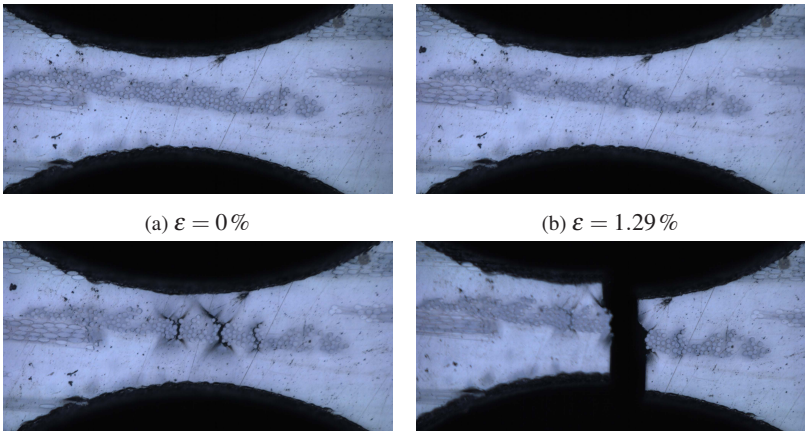

(a) $\varepsilon = 0\,\%$ (b) $\varepsilon = 1.29\,\%$

(c) $\varepsilon = 3.7\,\%$ (d) $\varepsilon = 3.7\,\%$

Figure 3.26: Fracture behavior of the specimen GF-6 during testing

$\varepsilon = 1.45\,\%$ to their initial appearance at $\varepsilon = 0\,\%$, however, most cracks in the finally failed specimen already exist at the beginning of the experiment.

Specimen GF-6 has the smallest fiber volume fraction of the investigated specimens. Here, only a single long fiber bundle is spread diagonally throughout the specimen, in which a first micro-crack develops at a total strain of $\varepsilon = 1.29\,\%$ and arrests at the interface of the bundle with the neat matrix area. In the course of the experiment, secondary cracks initiate next to the first crack. Shear bands emerge into the matrix at an angle of 45° surrounding the micro-cracks. The specimen suddenly fails when the matrix ruptures at the largest bundle crack. Although pronounced shear bands have already developed, the polymer breaks in brittle mode transversely to the load direction.

Specimen GF-14 features a wide, densely packed fiber bundle at the lower specimen edge with a pronounced longitudinal orientation, which

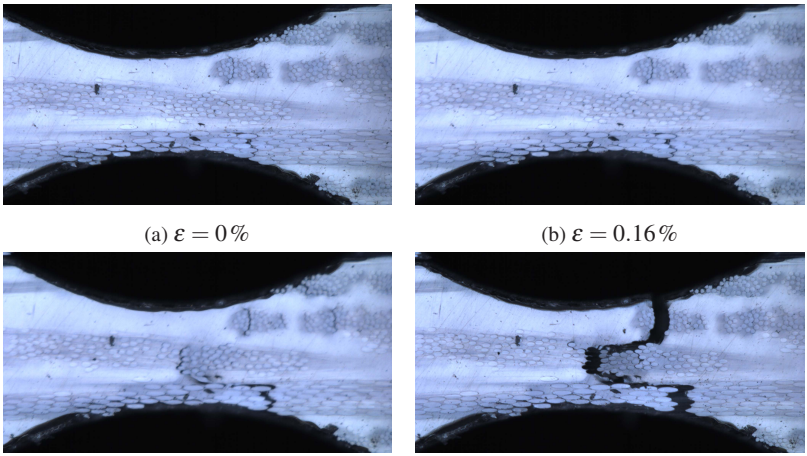

(a) $\varepsilon = 0\,\%$ (b) $\varepsilon = 0.16\,\%$

(c) $\varepsilon = 1.26\,\%$ (d) $\varepsilon = 3.2\,\%$

Figure 3.27: Fracture behavior of the specimen GF-14 during testing

causes a rough edge with exposed fibers. Pre-loading the specimen at $\varepsilon = 0\,\%$ reveals a small crack in a very dense region of that bundle. Furthermore, another pre-crack is visible in an out-of-plane bundle on the opposite specimen side, yet not reaching the specimen edge. In the course of the experiment, further micro-cracks develop in densely packed fiber bundles. Another crack is formed at the boundary of a slightly longitudinally oriented bundle in the center of the specimen. The crack in the longitudinally aligned bundle propagates through the bundle and subsequently along the bundle and merges with crack in the specimen center ($\varepsilon = 1.26\,\%$). This crack merger leads to a sudden increase of the measured strain. At this point, the right side of the specimen starts tilting, since the load carrying part of the specimen became severely asymmetric. The specimen finally fails when the crack in

the specimen center merges with the second crack, which has – to this point – not further propagated.

Some specimens contain cracks which were not detected prior to testing. Nevertheless and including these cracks, all specimens' fractures initiate in a single or in multiple densely packed fiber bundles. The subsequent crack propagation depends on the orientation of the initiating bundle and the orientation of the surrounding fiber bundles. In general, however, the cracks propagate mainly along fiber-matrix interfaces, both within fiber bundles and along fiber bundle boundaries. Final failure is mainly caused by a cascade of merging micro-cracks, which goes along with local matrix failure. In general, the polymer fails only in regions where cracks have already developed, within, or at the boundary of fiber bundles. Although shear bands might develop under 45° to the load direction, the matrix always fails in a brittle mode transversely to the loading direction.

3.2.3 Interlaminar Fracture Toughness Test

The interlaminar fracture toughness investigation is sub-divided in the basic characterization of the materials elastic properties required for the subsequent numerical simulation, the fracture toughness tests, and the analysis of the material's microstructure and fracture initiation schemes.

Basic Characterization

The basic characterization by means of tensile tests in fiber direction and transverse to the fiber direction and V-notched rail shear tests is evaluated in terms of the corresponding Young's moduli E_{11} and E_{22} and the in-plane shear modulus G_{12}, respectively. The Young's moduli are plotted in Figure 3.28 in dependence on the consolidation parameters. The fiber dominated stiffness in fiber direction in Figure 3.28a shows a comparatively homoge-

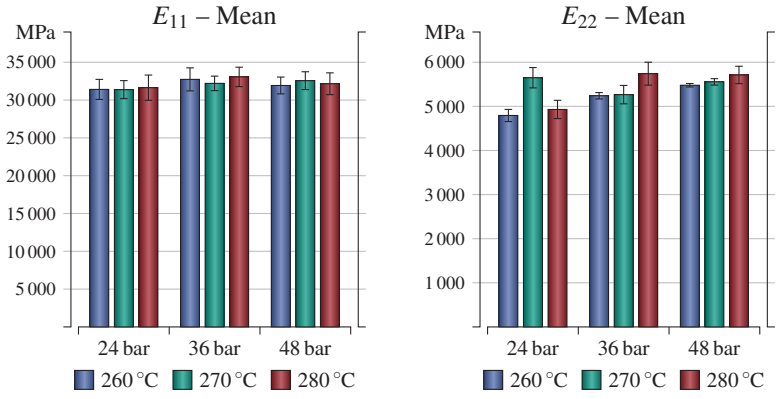

Figure 3.28: Tensile test results with respect to the consolidation parameters: (a) E_{11} in fiber direction, (b) E_{22} transverse to the fiber direction

neous Young's modulus with a mean value of 32 120 MPa and a variability of 4.1 %. The average moduli for all process parameters lie in the same scatter band and therefore can be assumed independent from the process.

The transverse Young's modulus E_{22} presented in Figure 3.28b exhibits a light dependence on the process parameters with slightly increasing values for increasing temperature and increasing pressure. However, an outlier at 24 bar and 260 °C contradicts this tendency. The overall average of E_{22} is 5367 MPa with a variability of 6.9 %.

The material's in-plane shear modulus G_{12} presented in Figure 3.29 exhibits a process parameter dependence similar to E_{22}. The mean values tend to increase with increasing consolidation pressure and increasing consolidation temperature. However, the shear modulus considerably scatters and the corresponding scatter bands partly overlap. The average of G_{12} is

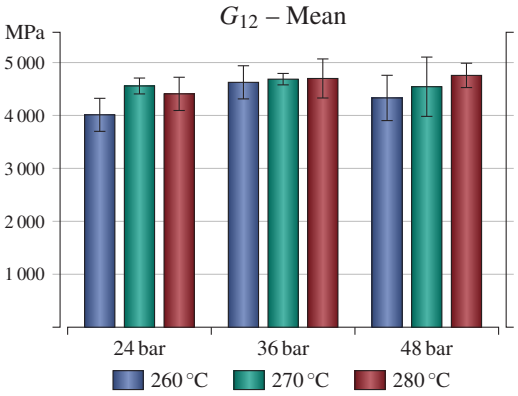

Figure 3.29: V-notched rail shear test results with respect to the consolidation parameters

4509 MPa with a variability of 8.1 %. The averaged summary is listed in Table 3.4 while detailed results are listed in the appendix in Tables A.4, A.5, and A.6, respectively.

Table 3.4: Overall summary of the basic characterization

	Mean Value	Deviation	Rel. Deviation
Young's Modulus E_{11}	32 120 MPa	1316 MPa	4.1 %
Young's Modulus E_{22}	5367 MPa	369 MPa	6.9 %
Shear Modulus G_{12}	4509 MPa	365 MPa	8.1 %

Fracture Toughness Characterization

The results of the double cantilever beam tests (DCB) are presented in Figure 3.30a in terms of the critical energy release rate $\mathcal{G}_{Ic}$ as defined in Equation 3.4. Within each specimen, the computed fracture toughness changes significantly

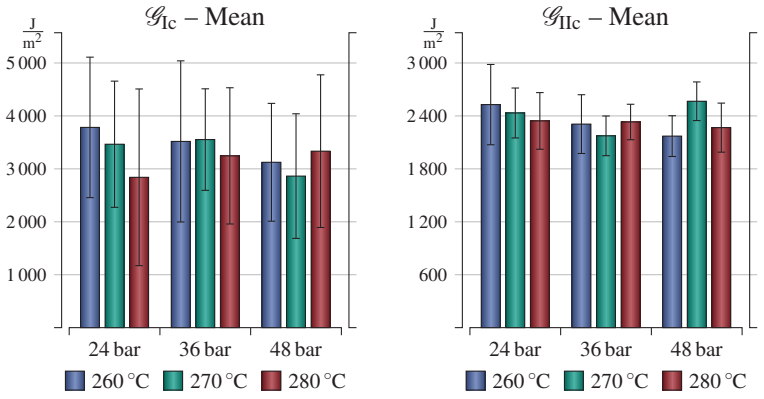

Figure 3.30: Fracture toughness test results: (a) DCB test results in mode I, (b) ENF test results in mode II

between the individual evaluations of Equation 3.4. This leads to an enormous scatter in the fracture toughness of the examined plaques. The scatter bands for the different process parameter sets overlap in wide ranges. Thus, making tendencies of process parameter are difficult to be identified. Even though the mean values change slightly when the evaluation scheme is switched to the MBT, the CC, or the MCC method (as described in Section 2.2.2), the scatter remains on the same level. The overall averaged mode I fracture toughness is $3300\,\mathrm{J\,m^{-2}}$ with a variability of 40 %.

Similar effect are observed for the mode II end notched flexure test (ENF), yet less pronounced than in the DCB results. However, the differences of the mean values with respect to the process parameters also vanish to a large extent in the overall scatter. The average mode II fracture toughness is

2350 J m^{-2} and significantly lower than the mode I fracture toughness. The variability lies on a more moderate level with 13 %.

Several striking characteristics can be observed when the fracture behavior during a mode I fracture toughness test is examined. Figure 3.31a shows a DCB specimen during testing, which features a large amount of fiber bridging from one crack surface to the other. Fibers which are properly embedded in both specimen sides can still carry loads and hence are also subject to fracture. Fiber bridging occurs when the fibers are not aligned completely horizontally or when the crack does not propagate ideally between two laminae. In Figure 3.31a, the two beams of the specimen exhibit unequal thicknesses, indicating that the crack crosses plies while propagating and thus promotes the formation of fiber bridges. Moreover, the initiation of secondary cracks is visible on the specimen edge, which can further promote fiber bridging. Some of these cracks propagate parallel to each other until they merge with the main crack, other cracks run out while the main crack is propagating further. In any case, the secondary cracks and the load carrying

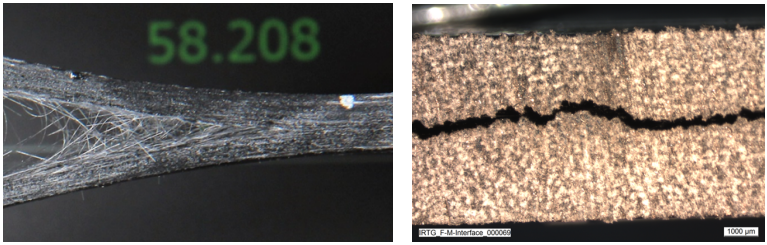

(a) (b)

Figure 3.31: Mode I fracture behavior in a DCB test: (a) longitudinal behavior with an large amount of fibers bridging the crack surfaces, asymmetric crack propagation and initiation of multiple secondary cracks, (b) transverse crack path after testing

fiber bridges create a fracture state which is hard to evaluate solely on the specimen edge.

Figure 3.31b shows the cross-section of a DCB specimen after testing. Instead of a plane crack with parallel crack surfaces, the specimen fractured in a rather rough transverse crack path with a roughness of approximately 0.5 mm. This rough crack surface indicates a rather inhomogeneous fracture propagation, not only at the specimen edge, but also within the specimen.

Microstructure Characterization

The material's microstructure and the fracture surface is analyzed further by means of optical as well as scanning electron microscopy (SEM). Micrographs of materials manufactured with three process parameter sets (24 bar-260 °C, 36 bar-270 °C, and 48 bar-280 °C) are shown in Figure 3.32. The original stacking sequence of the tape lay-up is directed vertically in all micrographs. The plaque consolidated at the lowest temperature and the lowest pressure exhibits a high amount of large voids. The fibers appear

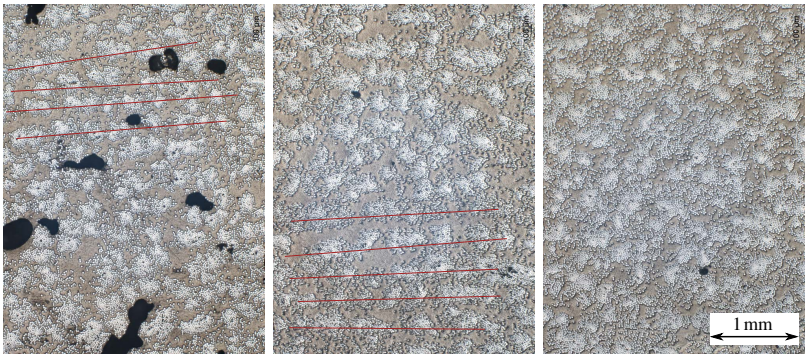

Figure 3.32: Micrographs illustrating consolidation effects – red lines indicating residual layer structure

in densely packed fiber bundles, which are surrounded by large matrix-rich areas. A long-range order can be observed in some areas featuring fiber bundles aligned next to each other, hinted by red lines. This long-range order is roughly horizontal, indicating the original stacking sequence. The plaque manufactured with 36 bar and 270 °C has a much smaller fraction of voids. Moreover, the voids are much smaller than the ones observed in the one consolidated at 24 bar and 260 °C. Again, the fibers are packed in dense bundles, which show a similar long-range order in certain areas. The plaque manufactured with 48 bar and 280 °C has the most homogeneous microstructure, the void content is minimal and the fibers are dispersed in smaller bundles. However, they are packed equally dense compared to the 36 bar-270 °C plaque. A long-range order of the fiber bundles cannot be detected. Although the micrographs shown in Figure 3.32 represent the extreme process parameter sets, an analysis of the remaining plaques exhibit similar effects on the microstructure.

Fractography

An example for a crack surface is shown in Figure 3.33 captured by SEM. The micrographs show groups of fibers aligned close to each other. The fiber sections which are not embedded in the matrix any longer show almost blank fiber surfaces. Only minor polymer residue can be detected. Between the fiber groups, areas of large plastic flow of the polymer matrix with extended waviness and large deformations can be seen, which are often shaped as former fiber beds. Between the fiber beds, thin but largely extended polymer stripes rise up the surface. Furthermore, the fracture surface contains a high amount of ruptured fibers with many fiber fragments dispersed over the surface, resulting from failed fiber bridges. Further magnification on the polymeric fiber beds reveal randomly dispersed micro-voids on the fiber-

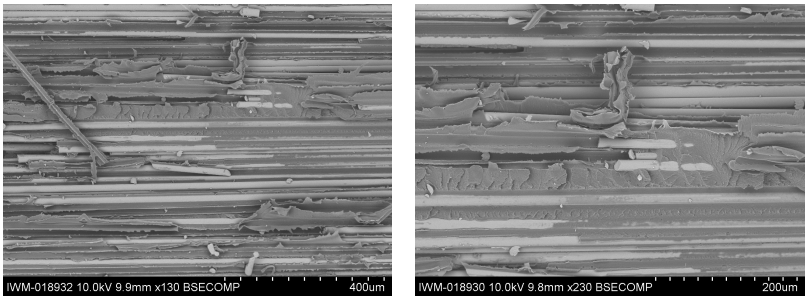

(a) (b)

Figure 3.33: SEM micrograph of a crack surface after conducted fracture toughness experiments in two magnifications

matrix interface, which cannot be detected in cross-sectional micro-graphs. In general, the fracture surface appears to be rough, especially in areas where individual fibers or fiber bundles ruptured. Moreover, the fracture surfaces of the 24 bar-260 °C-plaque revealed that also voids with small cross-sections exceed a length of 1 mm in longitudinal fiber direction.

Cross-sectional micrographs of fracture toughness specimens captured by SEM are shown in the Figures 3.34 and 3.35. The cross-sections are located in front of the macroscopic crack front and give an insight in the material's fracture initiation. Independent cracks develop within the densely packed fiber bundles. They branch out and propagate perpendicular to the specimen axis in the bundles via the fiber-matrix interfaces until they arrest at the boundaries of the fiber bundles with the polymer-rich area. The subsequent propagation is again driven by the fiber-matrix interfaces. The cracks in two fiber bundles merge along a path which mainly consists of fiber-matrix interfaces and only little amounts of matrix cracking. First, a designated crack path is created along fibers located next to each other by failing interfaces or polymer failure around the interface, as shown in the

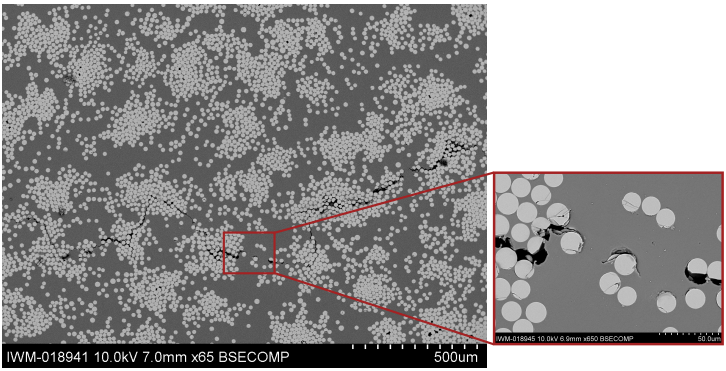

Figure 3.34: Cross-sectional glssem-micrograph capturing the fracture initiation within fiber bundles and its propagation via fiber-matrix interfaces

close-ups of both Figures 3.34 and 3.35. When the necessary crack opening is reached, the matrix connecting the cracked bundles fails and thus the micro-cracks merge. This fracture initiation and propagation scheme results in a

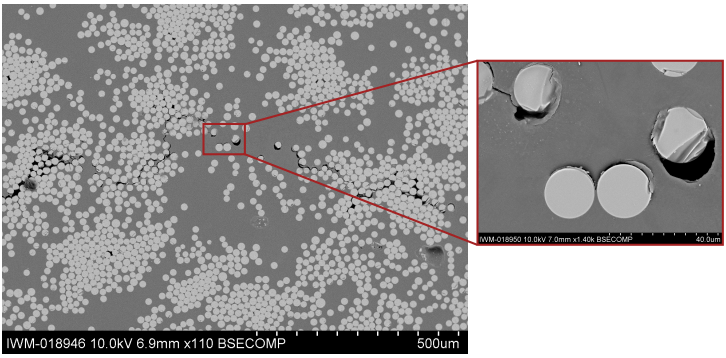

Figure 3.35: Fracture initiation and crack branching within fiber bundles; failing fiber-matrix interfaces

rough fracture surface with a ragged crack path with branched out secondary cracks.

As mentioned above, secondary cracks can occur parallel to the main crack. Figure 3.36 shows the initiation of such a secondary crack apart from the main crack, captured by SEM. Similar to the initiating cracks in Figures 3.34 and 3.35, the secondary crack initiates within a densely packed fiber bundle. The crack meanders and branches along the interfaces of contacting fibers. Individual failed interfaces which are not part of the crack indicate, that the crack is initiated by individual fiber-matrix interface fractures, which merge due to their propagation. The polymer itself shows only microscopic fracture in the middle of the bundle. The surrounding matrix, however, does not exhibit any damage.

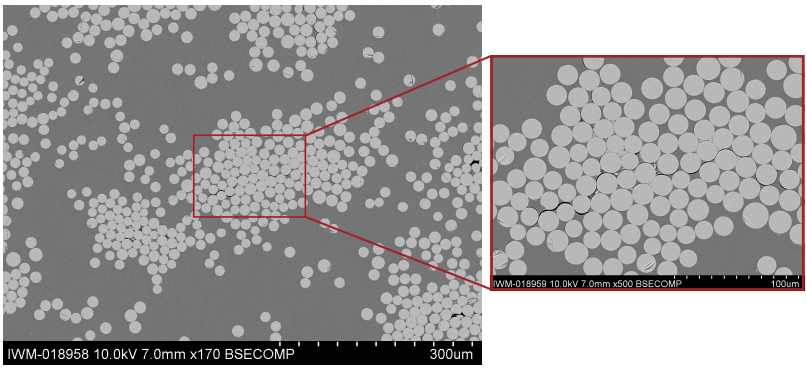

Figure 3.36: Initiation and branching of secondary cracks in a fiber bundle distant from the main crack

4 Numerical Assessment of the Physical Experiments

The physical experiments described in Chapter 3 are assessed by numerical simulations using finite element analyses (FEA). For this purpose, the composites are individually modeled on the three investigated scales. The following sections are divided in the material models for the constituents, the numerical modeling of the physical experiments, and the corresponding results.

4.1 Modeling FRP Constituents

The FE models basically consist of three constituents: (i) the reinforcing fiber, (ii) the embedding matrix, and (iii) the interface connecting the each individual fiber to the matrix surrounding it. Since all experiments have been conducted with e-glass fibers, a single fiber material model is used for all numerical simulations. In an ideal scenario, the fibers are not subject to failure during the experiments. For this reason, the glass fiber model considers pure linear-elastic material behavior with a Young's modulus of $E_f = 73\,000\,\text{MPa}$ and a Poisson's ratio of $\nu = 0.22$. The modeling of the three different polymers and the formulation of the cohesive zones in the interfaces are described in the following sections.

4.1.1 Matrix Modeling

The parameters of the material models for the neat polymers are fitted to experimental data by means of a tensile test numerically simulated. Regarding the UPPH characterization, the dovetail test according to Section 3.1.2 is modeled. For the PP and the PA6, material data is taken from the literature and the corresponding tensile test according to ISO 527 is modeled. In order to reduce the computational effort, each of the models is reduced to a half specimen considering their symmetry. The geometric models of the specimens are shown in Figure 4.1.

All three polymers are modeled assuming linear-elasticity combined with plasticity. Based on the results of Fliegener (2015) and Fliegener et al. (2017), this approach is considered sufficient for proportional loading up to failure. Subsequently, the plastic behavior is described by the von-Mises-plasticity model with isotropic, piecewise linear hardening. Material damage initiates when the equivalent plastic strain reaches a threshold. The evolving

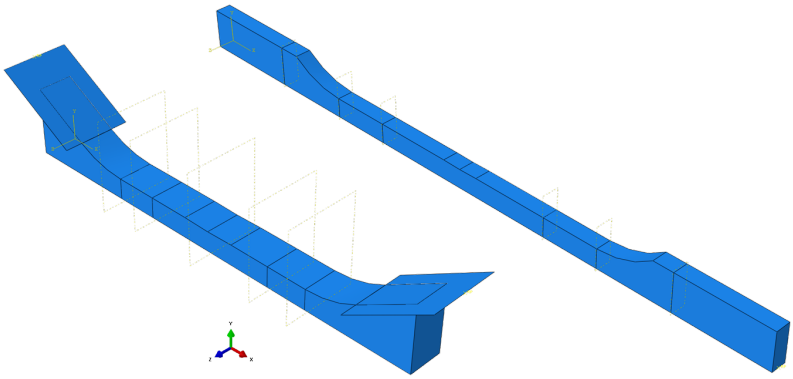

Figure 4.1: Geometries of the numerical tensile test specimens: (left) dovetail specimen, (right) specimen according to ISO 527

damage scales the material's stiffness down linearly, which is based on the damage energy (Abaqus, 2018).

Polypropylene – SABIC PP 579S

Since experiments on neat PP specimens could not be conducted, the numerical model is generated by experimental data from the literature. The material model is based on the experimental results by Amundsen (2014). Here, sample plaques were injection molded with SABIC PP 579S granulates and characterized by means of tensile tests with DIC strain measurement at angles of 0°, 45°, and 90° to the flow direction. The tests were evaluated regarding the true stress – true strain relationship. The results of the test series are plotted in Figure 4.2 with respect to the test directions 0°, 45°, and 90°, respectively.

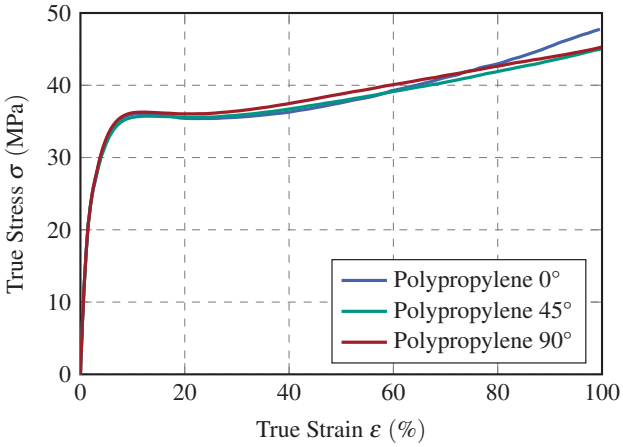

Figure 4.2: Stress-strain-curves of SABIC PP 579S by Amundsen (2014)

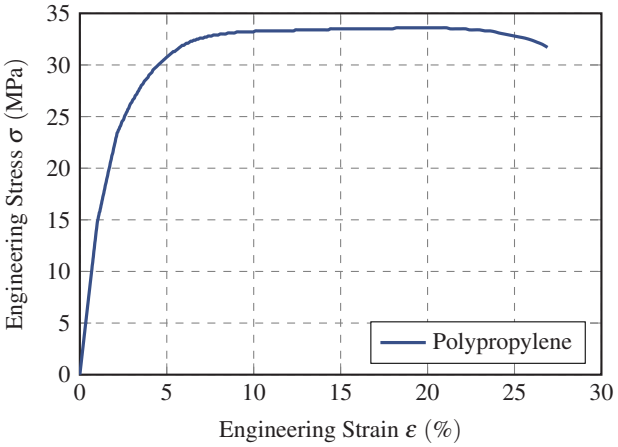

Figure 4.3: Resulting stress-strain behavior of polypropylene in a simulated ISO 527 tensile test

The test results of the 0° specimen is used to describe the hardening curve. Together with the tensile strength obtained from the official SABIC data sheet, the elastic-plastic material model is derived. The model features a Young's modulus of 1480 MPa and a Poisson's ratio of 0.42. The plastic flow initiates at approximately 15 MPa at 1 % total strain and dominates the the evolution of the stress-strain curve from 5 % onwards. The model reaches a tensile strength of 34 MPa with an elongation at break of approximately 26 %. The resulting stress-strain behavior of the PP-model in an ISO 527 tensile test is plotted in Figure 4.3.

Unsaturated polyester polyurethane hybrid resin – Aliancys Daron ZW 014142

The small dovetail tensile test described in Section 3.1.2 is numerically modeled to fit the UPPH parameters to the experimental test results. The model

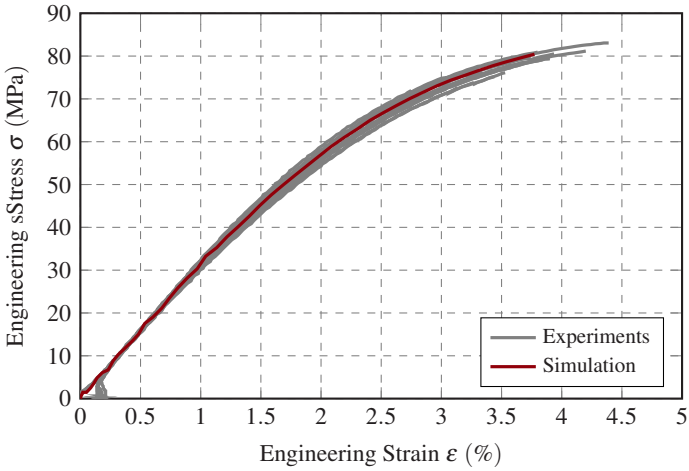

Figure 4.4: Comparison between experimental and numerical UPPH tensile test results

features a Young's modulus of 3186 MPa. Since the polymer's transverse strains cannot be measured with the accessible test set-up, the Poisson's ratio cannot be computed. Hence, an assumed the Poisson's ratio value of 0.3 is chosen for the numerical model. The plastic flow initiates at approximately 34 MPa at 1 % total strain and increases slowly. The material reaches a tensile strength of approximately 81 MPa at 3.8 % total strain, which is concurrently the point of rupture. The model suits the experimental results well and represents a rough average of the experiments in terms of the obtained tensile strength and elongation at break. The plotted stress-strain curves of the experiments and the numerical model is shown in Figure 4.4.

Polyamide-6 – BASF Ultramid B3K

The polymer used in the continuous fiber reinforced thermoplastic tape is the polyamide-6 by BASF with the brand name Ultramid B3K. Tensile test

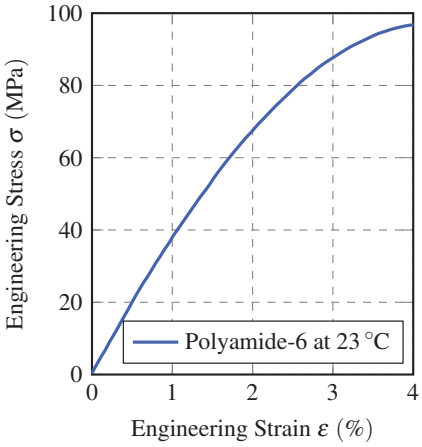

Figure 4.5: Stress strain behavior of polyamide-6 as provided by the manufacturer

data provided by the manufacturer are shown in Figure 4.5. Here, stress-strain curves obtained by tensile tests are plotted with respect to the test temperature and in the range between 0 % and 4 % total strain. Since the official data sheet specifies the rupture strain in dry conditions at 23 °C with approximately 25 %, however, the tensile test data is incomplete.

The numerical model for the polyamide-6 is derived from the data provided by BASF regarding the initial behavior and is extended to represent the further plastic flow and the corresponding strain at failure. The material features a Young's modulus of 3216 MPa and a Poisson's ratio of 0.39. The plastic flow initiates at 52 MPa at approximately 1.7 % total strain and dominates the total strain growth from approximately 5 % onwards, which leads to a nearly ideal elastic-plastic behavior, as presented in Figure 4.6. The numerical PA6 reaches a tensile strength of 93 MPa at a total strain of 24 %.

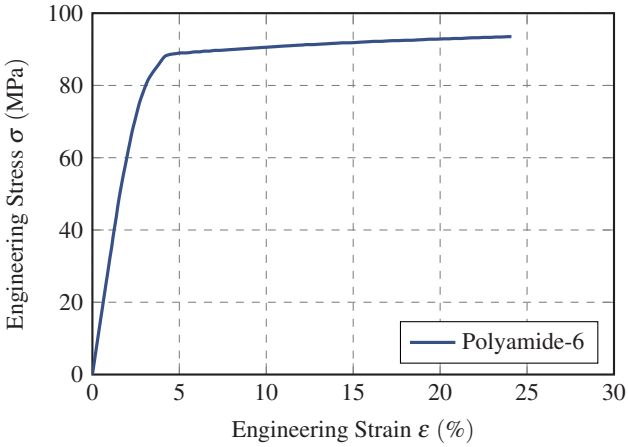

Figure 4.6: Resulting stress-strain behavior of polyamide-6 in a simulated ISO 527 tensile test

4.1.2 Cohesive Interface Formulation

All interfaces – whether fiber-matrix interfaces or lamina interfaces – are modeled by surface-based cohesive zone formulations. Here, the surface interaction between two solids – specifically the relative surface separations and the transferred loads – is described by the cohesive zone and a corresponding damage model. For failed cohesive zones, a contact formulation is used to prevent overclosure.

The cohesive stiffness implemented in the interface behavior excludes inter-mode coupling, hence $K_{ij} = 0$ for $i \neq j$. For simplicity, the cohesive stiffness of the lamina interface is considered isotropic, hence $K_{nn} = K_{ss} = K_{tt}$. Regarding the fiber-matrix interfaces, the mode II and mode III shear effects are considered equal, since none of the physical experiments described in Section 2.1 can be used to examine the mode III properties of the fiber-matrix

interface. This leads to the cohesive stiffness matrix $\boldsymbol{K}$ for the fiber-matrix interfaces:

$$\boldsymbol{K} = \begin{pmatrix} K_{nn} & 0 & 0 \\ & K_{ss} & 0 \\ \text{sym.} & & K_{ss} \end{pmatrix}. \tag{4.1}$$

Interface damage initiates according to the quadratic traction criterion. Similar to the cohesive stiffness, the interface strengths (including lamina interfaces) are equivalent regarding the first and second shear modes, making $t_t^{\mathrm{c}} = t_s^{\mathrm{c}}$. Thus, damage initiates when the following equation (see also Equation 2.4) is fulfilled (Abaqus, 2018):

$$\left(\frac{\langle t_n \rangle}{t_n^{\mathrm{c}}}\right)^2 + \left(\frac{t_s}{t_s^{\mathrm{c}}}\right)^2 + \left(\frac{t_t}{t_s^{\mathrm{c}}}\right)^2 = 1. \tag{4.2}$$

The damage evolution is specified based on the critical fracture energy Γ^{c}, whereas its dependence on the mode mix is defined by the power law fracture criterion. Therefor, the critical fracture energies for each fracture mode is specified with Γ_n^{c}, Γ_s^{c}, and Γ_t^{c}. Again, the first and the second shear mode are not distinguished, making $\Gamma_t^{\mathrm{c}} = \Gamma_s^{\mathrm{c}}$. Complete fracture is achieved as soon as the following equation is satisfied (Abaqus, 2018):

$$\left(\frac{\Gamma_n}{\Gamma_n^{\mathrm{c}}}\right)^2 + \left(\frac{\Gamma_s}{\Gamma_s^{\mathrm{c}}}\right)^2 + \left(\frac{\Gamma_t}{\Gamma_s^{\mathrm{c}}}\right)^2 = 1. \tag{4.3}$$

4.2 Numerical Modeling of the Physical Experiments

The experimental investigations described in Section 3.1 – namely the single-fiber microbond test, the multi-fiber tensile test, and the interlaminar fracture toughness test – are simulated numerically based on the component models described in Section 4.1. The modeling approaches of each experiment are described in the following sections, whereas the results of the numerical investigations are presented in Section 4.3.

4.2.1 Single-Fiber Microbond Test

The essential part for the numerical model of the single-fiber microbond test is a geometrically accurate model of the polymer droplet. The droplet is modeled by means of a solid of revolution in which the longitudinal axis of the fiber is used as the rotational axis. A B-spline traces one quarter of the droplet contour, which is provided by a microscope image. The procedure is illustrated in Figure 4.7a, in which the contour traced B-spline is in the upper-left quadrant. The spline is subsequently mirrored at the droplet's horizontal symmetry plane. The obtained spline fits well on the droplet contour, emphasizing the droplet's vertical symmetry, and is subsequently rotated around the rotational axis to create the droplet solid. However, mirroring the complete spline at the rotational axis does not fit well on the opposite droplet contour. Instead, an offset between the spline and the contour remains, which reveals that the polymer droplet is not rotationally symmetric. In order to avoid an over- or underestimation of the entire droplet shape, the described procedure is repeated on the opposite size of the droplet. Subsequently, an averaged spline based on the two contour splines is created and used to define the shape of the solid model of the droplet, as is shown

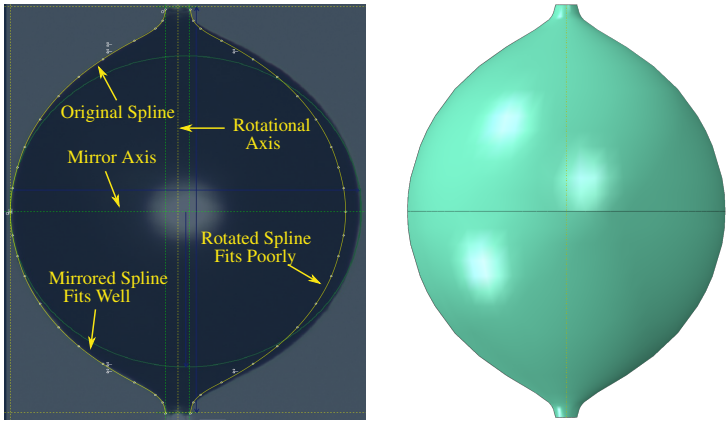

Figure 4.7: Droplet modeled in Abaqus by a solid of revolution: (a) sketch reveals horizontal symmetry of the droplet, but deviations in the rotation symmetry, (b) resulting rotational symmetric droplet model

in Figure 4.7b. The droplet geometry is assigned with the polypropylene material model according to Section 4.1.1

The fiber is modeled as a solid of rotation as well, defined by the fiber radius extracted from the microscope image. The fiber is longer than the embedded length l_e and it exceeds the droplet on both droplet ends. Both the fiber and the droplet are meshed with linear four-node tetrahedron elements with an edge length of approximately 5 µm. The perforated stainless steel sheet, which strips the droplet off the fiber, is modeled as a rigid plane which is rotated around the fiber's medial axis. All six degrees of freedom of the plane are clamped, making it neither movable nor rotatable. The contact definition between the shell and the droplet does only regard normal pressure and neglects friction. Making the model comparable to the physical experiment, the resulting reaction force and the displacement of the fiber's

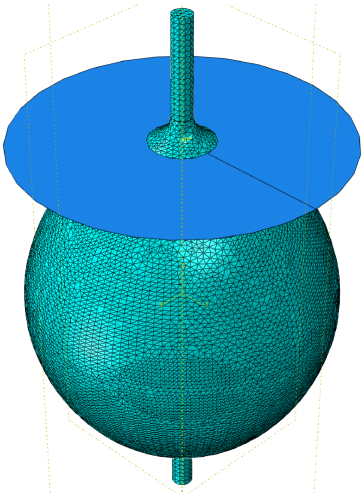

Figure 4.8: Abaqus model of the single-fiber microbond test: the perforated stainless steel sheet is modeled by a rigid shell (blue)

top nodes are recorded, while the fiber is pulled upwards until the droplet has completely debonded. The complete Abaqus model of the microbond test is shown in Figure 4.8.

4.2.2 Multi-Fiber Tensile Test

The multi-fiber tensile test specimen tested in Section 3.2.2 are modeled in detail regarding the exact dimensions of the specimens as wells as the distribution and orientation of the fibers within the specimens. For this purpose, the thickness and the width of every specimen is microscopically determined prior to testing. Furthermore, the location and orientation of each fiber is analyzed by means of an algorithm tracking the fibers' medial axes by post-processing micro-computed tomography (μCT) data. The μCT scans and the fiber tracking algorithm is provided by Pinter (2018). The tracking

algorithm generates arrayed, voxel-based coordinate points of each identified fiber.

The voxel coordinates are used as raw input data to create the specimen model. However, since the data defines the fibers by discrete coordinates, further assumptions are necessary to obtain continuous fibers within the specimen. Since the ratio between the fiber diameter and the specimen dimensions is sufficiently large, it is assumed that the fiber curvature within the specimen can be neglected, hence a straight fiber is assumed. Based on this assumption, a three-dimensional, linear regression of each fiber data set is computed. In other words, the coordinates of each fiber are analyzed regarding the fiber's geometrical center and its orientation. While the former is achieved by the simple mean values of the fibers' Cartesian coordinates x, y, and z, the fiber's direction vector is computed using the Singular Value Decomposition (Yu et al., 2011). The fibers' Cartesian direction vectors are converted to the angles ϑ and φ in the spherical coordination system, as shown in Figure 4.9.

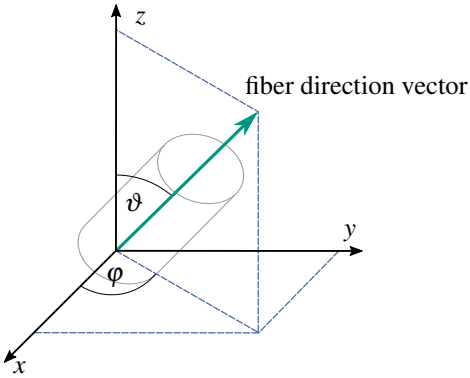

Figure 4.9: Conversion of the fiber direction vector to the spherical angles ϑ and φ

However, the obtained data also include apparent fibers which consist of very few coordinate points. In order to avoid such artifacts with random orientations, data sets consisting of less than five coordinates for a single fiber are considered fragments caused by μCT noise and are neglected in the model definition. The remaining fiber data sets are considered valid and are used to generate the FE model. For each data set, a single fiber model is created, moved according to its designated position of its geometrical center, and rotated by the computed angles ϑ and φ. After all fibers have been generated and positioned, they are cut to suit the specimen dimensions. An example for the resulting distribution of fibers is shown in Figure 4.10.

To model the matrix geometry, a solid model based on the specimen dimensions is created, cut at the designated fiber locations, and assigned with the UPPH material model according to Section 4.1.1. All fiber-matrix interfaces are modeled according to the surface-based cohesive zone formulation described in Section 4.1.2. In order to avoid probable stress concentrations in the loading areas, additional load transmission elements are created and attached to the multi-fiber specimen's front surfaces via tie constraints. Displacement controlled boundary conditions are applied on the front surfaces

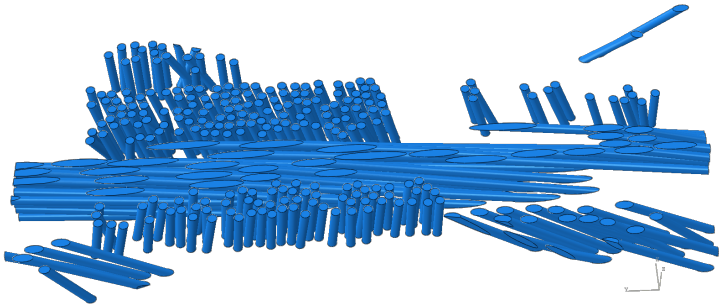

Figure 4.10: Fibers positioned and oriented according to the μCT tracking data

of the transmission elements, hence one side is clamped and the other side is displaced. The model is meshed with linear four-node tetrahedron elements with an edge length of approximately 5 µm or smaller where necessary to adequately mesh the model geometry. To simplify the meshing, the geometry is not further partitioned to create node sets in the virtual strain gauge regions. Instead, the displacements are measured at the tie constraints between the specimen and the load transmission elements. An example for the model created with the fiber set illustrated in Figure 4.10 is shown in Figure 4.11.

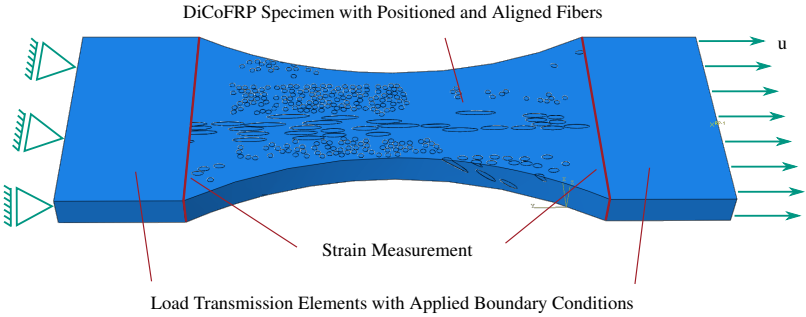

Figure 4.11: Multi-fiber tensile test specimen, consisting of the fiber distribution based on μCT tracking, embedding matrix, an load transmission elements on which the boundary conditions are applied

Since the multi-fiber tensile test models feature several fiber orientations in a single specimen, the test method is suitable to analyze the influence of unequal interface strengths in normal and shear direction. Therefore, the ratio between the critical traction components initiating damage in the cohesive zone in normal and shear direction t_n^c/t_t^c is varied. The corresponding experimental ratio σ_{ult}/τ_{ult} was obtained by Tandon et al. (2002) with approximately $\sigma_{ult}/\tau_{ult} \approx 1.22$ regarding SiC fiber reinforced epoxy and by Ogihara and Koyanagi (2010) with a range of $\sigma_{ult}/\tau_{ult} = 1.3$ to 1.8 regarding glass fiber reinforced epoxy. Both experimental series were conducted using cruciform

specimens. With a single-lap shear test of two planar e-glass sheets bonded by epoxy, Swentek (2014) measured $\sigma_{ult}/\tau_{ult} \approx 1.6$. The critical traction ratio t_n^c/t_s^c is therefore varied according to the the referred literature. Furthermore, the ratio of critical fracture energies Γ_n^c/Γ_s^c is varied likewise to increase the impact of the interface anisotropy and to decrease the computational effort ($t_n^c/t_s^c = \Gamma_n^c/\Gamma_s^c = \{1.0, 1.2, 1.4, 1.6, 1.8\}$).

The friction occurring between a fiber and the matrix after debonding is considered to influence the debonding and the global failure process (Greisel et al., 2014; Fliegener, 2015). The possible effects of such post-failure friction are analyzed using a friction formulation based on a penalty formulation. This formulation assumes a constant friction coefficient μ regarding the tangential slip of two surfaces in contact.

4.2.3 Interlaminar Fracture Toughness Test

The interlaminar fracture toughness of the consolidated PA6 tapes is analyzed regarding its fracture behavior in the double cantilever beam test (DCB). The material model parameters are obtained from the basic characterization described in Section 3.1.3 – specifically the longitudinal and the transverse Young's moduli E_{11} and E_{22} and the in-plane shear modulus G_{12}. Missing parameters such as the Poisson's ratios ν_{12} and ν_{21} and the out-of-plane shear modulus G_{23} are computed based on the mechanics of unidirectional laminae provided by Schürmann (2007), which assume a transversely isotropic material behavior.

The modeling approach covers the three hierarchical scales for the mechanical behavior of a composite structure: the macroscale with the entire DCB specimen, the mesoscale on which the fiber agglomeration is considered, and the microscale with single fibers distributed in the polymer

matrix. With this multi-scale examination, all effects leading to the fracture behavior observed in Section 3.2.3 shall be considered.

The DCB specimen is modeled with a cohesive zone in the designated, planar crack path, whereas linear-elastic material behavior is assumed. The model parameters are the averaged results of the basic material characterization and the mode I fracture toughness characterization, respectively, as described in Section 3.2.3. The GF-PA6 mesostructure consists of fiber-rich and matrix-rich regions, which can be unified in clusters depending on the fiber volume fraction, as illustrated in Figure 4.12 and indicated by red lines. These clusters are modeled as homogeneous solids without distinction between fibers and matrix, but based on the fiber volume fraction, and included into the macroscopic DCB model using a sub-modeling technique. The linear-elastic parameters of the cluster models are computed based on the mechanics of unidirectional laminae, thus transversely isotropic material properties are assumed. The fracture behavior of the cluster cells is modeled by numerous cohesive zones within each cell. The corresponding fracture parameters are obtained by microscopic fracture models, consisting of var-

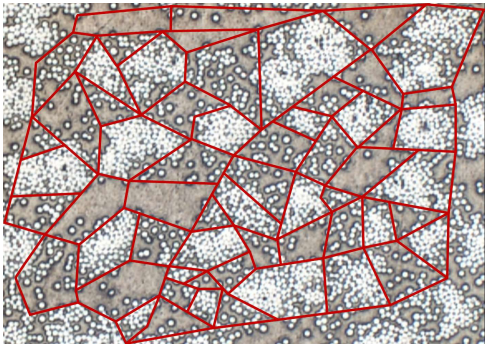

Figure 4.12: Fiber- and matrix-rich clusters in GF-PA6 mesostructure

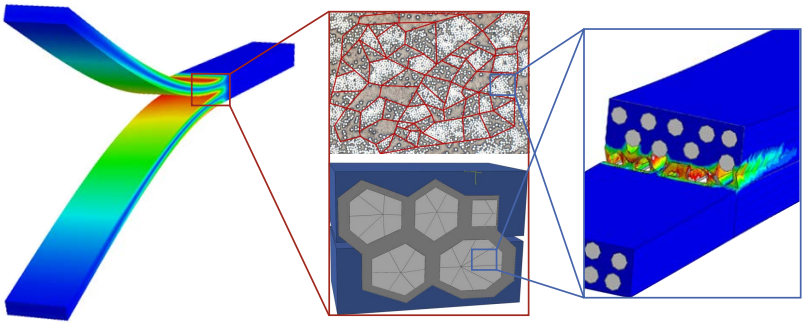

Figure 4.13: Modeling approach considering three scales: (left) the macroscopic specimen behavior, (middle) the fiber agglomerations on the meso-scale, and (right) the fracture behavior on the microscale, including fiber-matrix interface failure

ious single fibers embedded in a matrix. This microscale model includes plastic flow and damage of the matrix as well as fiber-matrix interface failure. Herewith, the microscopic crack propagation is analyzed and mapped onto the cohesive zones in the mesoscopic cluster models. The schematic approach including the three hierarchal scales is illustrated in Figure 4.13. The generation of the mesostructure and the analysis of the microstructure is thoroughly described in the following sections.

Mesostructure Model Generation

The cluster scheme of the GF-PA6 mesostructure shown in Figure 4.12 resembles a Voronoi tessellation. In order to simplify the modeling procedure, the mesostructure clusters are not modeled exactly, but by means of an artificial Voronoi tessellation. A tessellation tool provided by Hardenacke and Hohe (2009) is used to create the cell boundaries based on the δ-Voronoi procedure and the Voronoi tessellation in Laguerre geometry. Details on the different procedures and their resulting tessellations are provided by

Hardenacke and Hohe (2010). An example for a δ-Voronoi cell structure is shown in Figure 4.14a. Based on this tessellation, solid cell models are extruded in Abaqus, assembled according to the original tessellation, and embedded in a homogeneous material block, hereinafter referred to as embedment (Figure 4.14b). This embedment connects the cell structure to the global DCB model and is plotted in blue in Figures 4.14b and 4.14c. In the region where the global DCB crack divides the submodel, the embedment is divided in two halves such that a small gap remains between them for unambiguous assignment of the boundary conditions. Each cell is subdivided into an inner cell, which represents a densely packed fiber bundle and is plotted light-gray in Figure 4.14c, and a surrounding cell, which represents a pure matrix region surrounding the fiber agglomerations (plotted in dark gray in Figure 4.14c). While all surrounding cells are merged to a single solid, cohesive zones are implemented in and around the fiber bundle cells. Amount and orientation of the cohesive zones depend on the amount and orientation of the Voronoi cell edges.

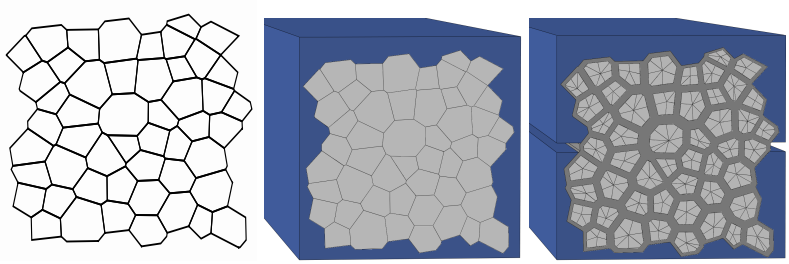

Figure 4.14: Mesostructure model generation: (a) artificial Voronoi tessellation in Laguerre geometry, (b) created Voronoi structure, (c) Voronoi sub-model with fiber-rich clusters (light-gray), surrounding matrix regions (dark grey) and a homogeneous embedment connecting the sub-model to the global DCB model (blue)

The displacements resulting from the global DCB model are mapped onto the surfaces of the homogeneous Voronoi embedment. Specifically, the displacements of the upper DCB-beam are mapped on the upper half of the embedment and the displacements of the lower DCB-beam are mapped on the lower half of the embedment. The surrounding (dark gray) cell structure is connected to the embedment (blue) via tie-constraints and to the inner (light-gray) cells via cohesive surfaces and features the PA6 material model including damage, as described in Section 4.1.1. Neither the embedment nor the inner cells are subject to failure. Consequently, a crack has to propagate along the cohesive zones and needs to spread throughout the whole Voronoi width via the pure matrix regions. However, the exact crack path is not pre-defined, since any cohesive zone is able to fail.

Microscopic Analysis of the Crack Propagation

The crack propagation on fiber and matrix level is analyzed by means of a model which considers both matrix damage and fiber-matrix interface failure. The model consists of a small number of fibers with a length of 1 mm which are unidirectionally aligned and embedded into the matrix. The fiber-matrix-model is 0.1 mm thick and 0.2 mm wide and 1 mm long. The model features a sharp pre-crack, which is 0.5 mm long and originates in the model center. The crack propagation scheme is analyzed by loading the model in mode I. For this purpose, a mode I crack tip opening displacement (CTOD) field is applied to the model. A circular load transmission block is tied on the top and on the bottom surfaces of the fiber-matrix-model. The shape of this block is defined by the radius $r = \sqrt{0.5^2 + 0.05^2}$ mm, which originates in the crack tip. This creates the disk-like model composition shown in Figure 4.15. The force transmission block features the fiber-matrix-model's effective, transversely isotropic material behavior.

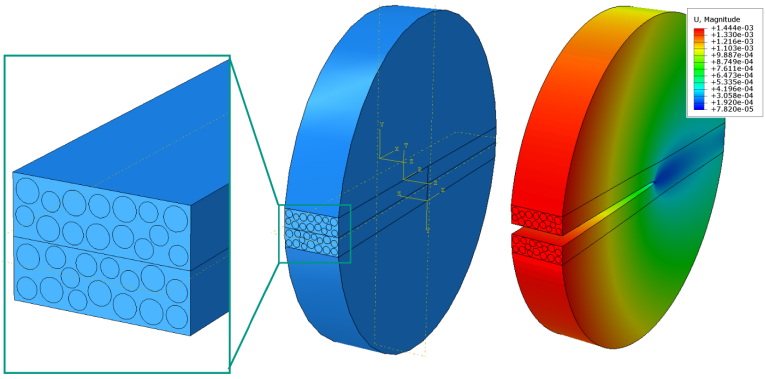

Figure 4.15: Microscale model consisting of disordered fiber-matrix-model featuring a pre-crack; boundary conditions are applied via force transmission elements according to the mode I crack tip opening displacements for orthotropic materials

As a matter of simplification, the resulting model is assumed to feature a plane strain state and linear elasticity. Hence, harmonic boundary conditions can be applied on the disk's front and back surfaces. Since a plane state is assumed, a two-dimensional mode I CTOD field (with the displacement u in fiber direction and the displacement v transverse to the fiber direction) can be applied on the disk's curved surfaces. Applying the CTOD derived for orthotropic materials is assumed to be an acceptable simplification for this purpose. The corresponding boundary conditions are obtained from Groß and Seelig (2018) and are described by

$$u(r,\varphi) = K_I \sqrt{\frac{2r}{\pi}}\,\mathrm{Re}\left\{\frac{1}{\mu_1-\mu_2}\left[\mu_1 p_2 \sqrt{\cos\varphi+\mu_2\sin\varphi}\right.\right. \\ \left.\left. -\,\mu_2 p_1 \sqrt{\cos\varphi+\mu_1\sin\varphi}\right]\right\}, \quad (4.4)$$

in fiber direction and

$$v(r,\varphi) = K_I \sqrt{\frac{2r}{\pi}}\,\mathrm{Re}\left\{ \frac{1}{\mu_1-\mu_2}\left[\mu_1 q_2 \sqrt{\cos\varphi+\mu_2\sin\varphi} - \mu_2 q_1 \sqrt{\cos\varphi+\mu_1\sin\varphi}\right]\right\}, \quad (4.5)$$

transverse to the fiber direction. Here, the displacements are given with respect to the polar coordinate system $\{e_r, e_\varphi\}$ which originates in the original crack tip. Hence, the radius r is equivalent to the radius of the load transmission blocks. Furthermore, K_I is not considered in its original meaning – the stress intensity factor – but only as a parameter to ramp up the boundary condition in the numerical simulation. The constants μ_1 and μ_2 are obtained by the bi-quadratic characteristic polynomial of the plain strain state and are related to the elastic material parameters:

$$\mu_{1,2} = \frac{i}{2}\left\{ \left[\frac{E_{11}}{G_{12}} - 2\nu_{12} + 2\left(\frac{E_{11}}{E_{22}}\right)^{\frac{1}{2}}\right]^{\frac{1}{2}} \pm \left[\frac{E_{11}}{G_{12}} - 2\nu_{12} - 2\left(\frac{E_{11}}{E_{22}}\right)^{\frac{1}{2}}\right]^{\frac{1}{2}}\right\}. \quad (4.6)$$

The constants p_1 and p_2 in Equation 4.4 and the constants q_1 and q_2 in Equation 4.5 are abbreviations for (Groß and Seelig, 2018; Kachanov et al., 2003):

$$p_k = \frac{1}{E_{11}}\mu_k^2 - \frac{\nu_{12}}{E_{11}}, \qquad q_k = -\frac{\nu_{12}}{E_{11}}\mu_k + \frac{1}{E_{22}}\mu_k^{-1}. \quad (4.7)$$

The influence of the fiber-matrix interfaces on the fracture behavior of the microscale model is analyzed by varying the parameters of the cohesive zones representing the interfaces. Subsequently, the microscale model is homogenized by means of a homogeneous solid containing a planar, horizontal cohesive zone. While the homogeneous solid features the fiber-matrix-model's effective elastic, transversely isotropic material properties, the cohesive zone is fitted to represent the fracture of the heterogeneous fiber-matrix-model. The obtained cohesive zone parameters are used in the mesoscale model described in Section 4.2.3, in which the cohesive zones model the crack initiation and propagation within the fiber bundles.

4.3 Results of the Numerical Assessment

In analogy to the experimental investigation described in Chapter 3, the results of the three sets of numerical simulations are presented separately in the following sections.

4.3.1 Single-Fiber Microbond Test

The single-fiber microbond test is modeled according to the physical experiments with specimens prepared in argon atmosphere, according to Sections 3.1.1 and 3.2.1. Damage initiation of the cohesive zone is set to a critical traction of $t^{\mathrm{c}} = 13\,\mathrm{MPa}$ for all loading modes. The cohesive zone's damage evolution by means of its separation energy is varied from $\Gamma^{\mathrm{c}} = 10\,\mathrm{J\,m^{-2}}$ to $\Gamma^{\mathrm{c}} = 50\,\mathrm{J\,m^{-2}}$, defining both normal and shear damage. The simulations are evaluated by means of the mean interfacial shear stress (computed by Equation 3.1) plotted against the displacement, in analogy to the physical experiments. Furthermore, the corresponding debonding propagation is analyzed.

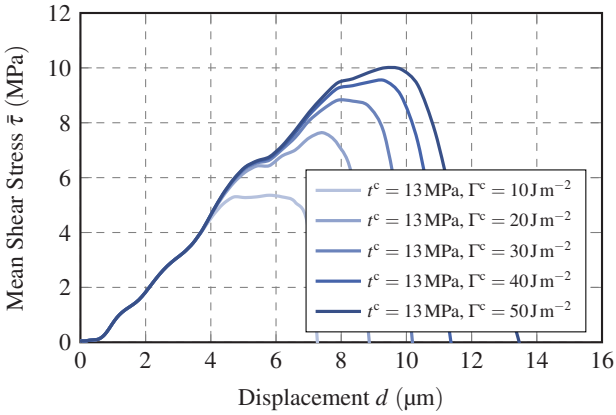

Figure 4.16: Numerical Microbond-test: fracture toughness variation ($\Gamma_n^c = \Gamma_s^c = 10\,\mathrm{J\,m^{-2}}$ to $50\,\mathrm{J\,m^{-2}}$) with constant damage initiation $t_n^c = t_s^c = 13\,\mathrm{MPa}$

The resulting shear stress-displacement curves of the numerical microbond tests are plotted in Figure 4.16. However, the fiber displacement at the loading position does not correspond to the recorded crosshead displacement mentioned in Section 3.2.2, since the free fiber length in the simulation is short compared to the physical experiment.

The curves show the same initial behavior with a linear relation between the fiber displacement and the applied force, neglecting the numerically induced waviness of the curves due to the employed explicit time integration scheme. Damage initiates at a fiber displacement of approximately $d \approx 4\,\mu\mathrm{m}$, where the simulation with the lowest separation energy starts to deviate from the linear force-displacement curve and shows a saturation behavior of the interfacial shear stress, which is characterized by a plateau at its ultimate interfacial shear stress $\bar{\tau}_{ult} = 5.4\,\mathrm{MPa}$. With increasing separation energy, this saturation behavior initiates at higher displacements and thus shear stresses and becomes less pronounced. Furthermore, the increase of

$\bar{\tau}_{\mathrm{ult}}$ due to an increase of the separation energy Γ^{c} decreases with higher Γ^{c}: whereas $\bar{\tau}_{\mathrm{ult}}$ increases from 5.4 MPa to 7.8 MPa when Γ^{c} is increased from $10\,\mathrm{J\,m^{-2}}$ to $20\,\mathrm{J\,m^{-2}}$, $\bar{\tau}_{\mathrm{ult}}$ increases merely from 9.7 MPa to 10.1 MPa when Γ^{c} is increased from $40\,\mathrm{J\,m^{-2}}$ to $50\,\mathrm{J\,m^{-2}}$. Hence, a saturation of the mean interfacial shear stress $\bar{\tau}_{\mathrm{ult}}$ with respect to the cohesive zone's separation energy Γ^{c} is observed.

Figure 4.17 shows the debonding propagation for the separation energies $\Gamma^{\mathrm{c}} = 10\,\mathrm{J\,m^{-2}}$ (Figure 4.17a), $\Gamma^{\mathrm{c}} = 30\,\mathrm{J\,m^{-2}}$ (Figure 4.17b), and $\Gamma^{\mathrm{c}} = 50\,\mathrm{J\,m^{-2}}$ (Figure 4.17c) by means of image sequences of several, equivalent fiber displacements between $d = 3.2\,\mu\mathrm{m}$ (onset of debonding)

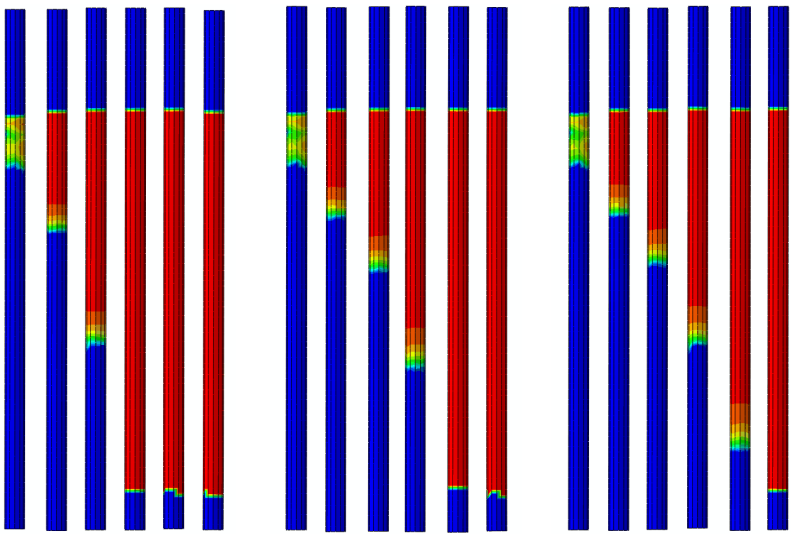

Figure 4.17: Droplet debonding propagation with respect to the fiber displacement at $d = 3.2\,\mu\mathrm{m}$, $4.4\,\mu\mathrm{m}$, $5.8\,\mu\mathrm{m}$, $7.4\,\mu\mathrm{m}$, $9.3\,\mu\mathrm{m}$, $11.4\,\mu\mathrm{m}$: (a) $t^{\mathrm{c}} = 13\,\mathrm{MPa}$, $\Gamma^{\mathrm{c}} = 10\,\mathrm{J\,m^{-2}}$, (b) $t^{\mathrm{c}} = 13\,\mathrm{MPa}$, $\Gamma^{\mathrm{c}} = 30\,\mathrm{J\,m^{-2}}$, (c) $t^{\mathrm{c}} = 13\,\mathrm{MPa}$, $\Gamma^{\mathrm{c}} = 50\,\mathrm{J\,m^{-2}}$

and $d = 11.4\,\mu\text{m}$ (completely debonded droplet). Here, the surface of the complete fiber is shown and colored with respect to the interface damage from blue (not damaged at all) to red (complete failure). However, since the droplet does not cover the entire fiber, the upper and the lower part of the surface remains blue, since no fiber-matrix debonding takes place. During the simulation, the fiber is pulled upwards, hence the droplet is stripped off downwards.

All simulations show a concurrent debonding onset at the top end of the droplet at a fiber displacement of $d = 3.2\,\mu\text{m}$. With further displacement of the fiber, the debonding propagates steadily downwards until the droplet end is reached. In doing so, the region between the completely intact and the completely damaged interface (plotted in a color range from green to orange) stays short during the debonding progress. The dimensions of this region do not significantly change with the increasing separation energy. The three simulation results shown in Figure 4.17 do not differ in the propagation scheme, but only in the propagation velocity: while the $\Gamma^{\text{c}} = 10\,\text{J}\,\text{m}^{-2}$ -interface has completely failed at a fiber displacement of $d = 7.4\,\mu\text{m}$, approximately 40 % of the $\Gamma^{\text{c}} = 50\,\text{J}\,\text{m}^{-2}$ -interface is still unharmed. It is noticeable, however, that the maximum force is reached after the major part of the interface has already failed. With $\Gamma^{\text{c}} = 50\,\text{J}\,\text{m}^{-2}$, for instance, the maximum force is reached at $d = 9.3\,\mu\text{m}$, where 80 % of the interface has already completely failed and only 10 % is still unharmed.

Figure 4.18 shows the interfacial shear stress-displacement plot of a microbond test with an increased critical traction of $t^{\text{c}} = 25\,\text{MPa}$ and the separation energy of $\Gamma^{\text{c}} = 30\,\text{J}\,\text{m}^{-2}$ and – for comparison – the plots of the simulations $t^{\text{c}} = 13\,\text{MPa}$ – $\Gamma^{\text{c}} = 30\,\text{J}\,\text{m}^{-2}$ and $t^{\text{c}} = 13\,\text{MPa}$ – $\Gamma^{\text{c}} = 50\,\text{J}\,\text{m}^{-2}$. Again, the initial behavior before damage initiation is identical. However, the $t^{\text{c}} = 25\,\text{MPa}$ – $\Gamma^{\text{c}} = 30\,\text{J}\,\text{m}^{-2}$ simulation retains its initial stiffness longer and reaches a higher mean ultimate shear stress of $\bar{\tau}_{\text{ult}} \approx 10.6\,\text{MPa}$ while its

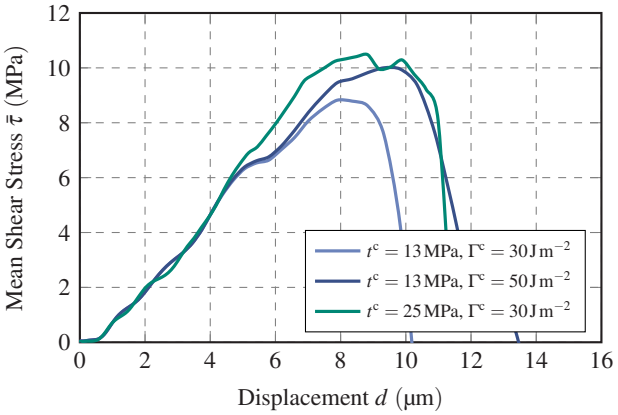

Figure 4.18: Numerical Microbond-test: similar simulation results in spite of widely varied damage initiation and fracture toughness

displacement to complete interfacial failure is comparable to the $t^c = 13\,\mathrm{MPa}$ – $\Gamma^c = 50\,\mathrm{J\,m^{-2}}$ simulation. Nevertheless, the resulting ultimate interfacial shear strength $\bar{\tau}_{ult}$ is 10.5 MPa and thus only slightly higher than 8.8 MPa and 10.0 MPa obtained from the parameter sets $t^c = 13\,\mathrm{MPa}$ – $\Gamma^c = 30\,\mathrm{J\,m^{-2}}$ and $t^c = 13\,\mathrm{MPa}$ – $\Gamma^c = 50\,\mathrm{J\,m^{-2}}$, respectively.

Figure 4.19 shows the debonding propagation in the $t^c = 25\,\mathrm{MPa}$ – $\Gamma^c = 30\,\mathrm{J\,m^{-2}}$ model similar to Figure 4.17, however, at slightly different fiber displacements d. A noticeably initiated damage at the top end of the droplet is reached at $d = 5.7\,\mu\mathrm{m}$, which evolves to a completely debonded droplet top end ($d = 6.9\,\mu\mathrm{m}$) and subsequently propagates along the interface with a narrow damage evolution region. Although the interfacial damage initiates later compared to the previous simulations, complete interface failure is reached after $d = 11.0\,\mu\mathrm{m}$, which is comparable to the $t^c = 13\,\mathrm{MPa}$ – $\Gamma^c = 50\,\mathrm{J\,m^{-2}}$ simulation.

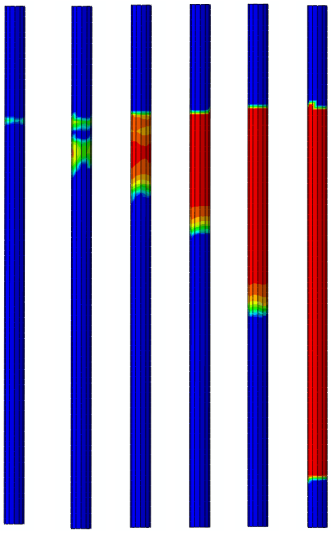

Figure 4.19: Droplet debonding propagation with respect to the fiber displacement at $d = 4.7\,\mu\text{m}, 5.7\,\mu\text{m}, 6.9\,\mu\text{m}, 8.2\,\mu\text{m}, 9.5\,\mu\text{m}, 11.0\,\mu\text{m}$: $t^{\text{c}} = 25\,\text{MPa}$, $\Gamma^{\text{c}} = 30\,\text{J}\,\text{m}^{-2}$

4.3.2 Multi-Fiber Tensile Test[3]

The numerical models of the multi-fiber tensile test specimens are generated based on the μCT fiber-tracking data provided by Pinter (2018). However, the generated models reveal the limits of this algorithm regarding the identification of individual fibers in densely packed fiber bundles. The models created with the data feature a large amount of intersecting and overlapping fibers, shown in Figure 4.20a. Furthermore, the actual amount of tracked fibers is not correct, since some fibers are erroneously merged or divided into two or three fibers. Since the model generation algorithm assumes continuous

[3] The optimization of the fiber configuration as well as the execution and evaluation of the simulations has been done in the scope of the Master's Thesis by Dittmann (2018) supervised by the author

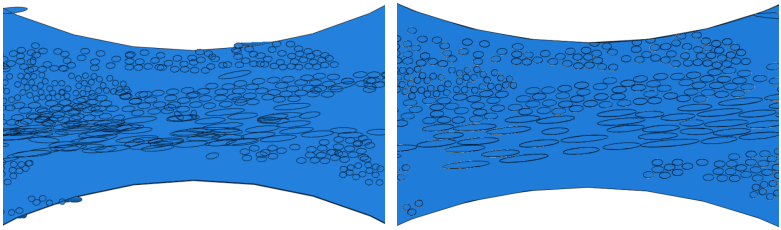

(a) (b)

Figure 4.20: Model section of specimen GF-3 generated with μCT data: (a) based on raw data, (b) after manual post-processing

fibers within the specimen, fibers which were divided during the tracking process lead to multiple fibers on almost the same location in the model. In order to obtain an executable FE model, the generated models need to be post-processed manually by removing and relocating incorrect fibers. An example is shown in Figure 4.20b.

In the following sections, the multi-fiber tensile test specimens GF-3, GF-5, and GF-6 from Section 3.2.2 are modeled and analyzed with different parameters of the cohesive zones between the fibers and the matrix.

General Variation of the Interface Parameters

The critical traction t^c and the critical separation energy Γ^c are varied in order to represent the maximum forces and fracture patterns observed in the physical experiments. Regarding specimen GF-3, the critical traction is varied from $t^c = 100\,\mathrm{MPa}$ to $300\,\mathrm{MPa}$ and the critical separation energy is varied from $\Gamma^c = 50\,\mathrm{J\,m^{-2}}$ to $200\,\mathrm{J\,m^{-2}}$. The resulting force-strain curves as well as the experimental force-strain curve are plotted in Figure 4.21. The resulting maximum forces prior to failure increase with increasing critical traction as well as with increasing critical separation energy. Only the simulations

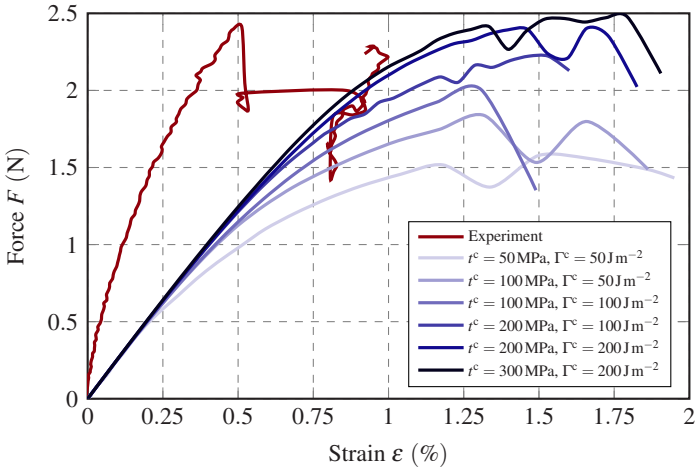

Figure 4.21: Force-strain curves of the physical and numerical tests of specimen GF-3

featuring the highest values of the varied parameters, namely $\Gamma^c = 200\,\mathrm{J\,m^{-2}}$ and $t^c = 200\,\mathrm{MPa}$ and $300\,\mathrm{MPa}$, respectively, reach the maximum force obtained by the physical experiment. Regardless of the cohesive parameters, all simulation results show a much larger strain and hence a much lower stiffness than the physical experiment.

Figure 4.22 shows the fracture pattern obtained by selected parameter sets. Here, the stiffness degradations of the polymer (a-d) and of the fiber-matrix interfaces (e-h) are plotted from blue (no damage) to red (complete failure). The figures show that the location of final fracture depends on the critical traction, but also on the critical separation energy when the critical traction is kept constant. With increasing values of the cohesive zone parameters, matrix failure predominates the failure of the interfaces, which remain intact to a higher amount. In general, most failed interfaces are located within fiber bundles and especially in regions where the fiber

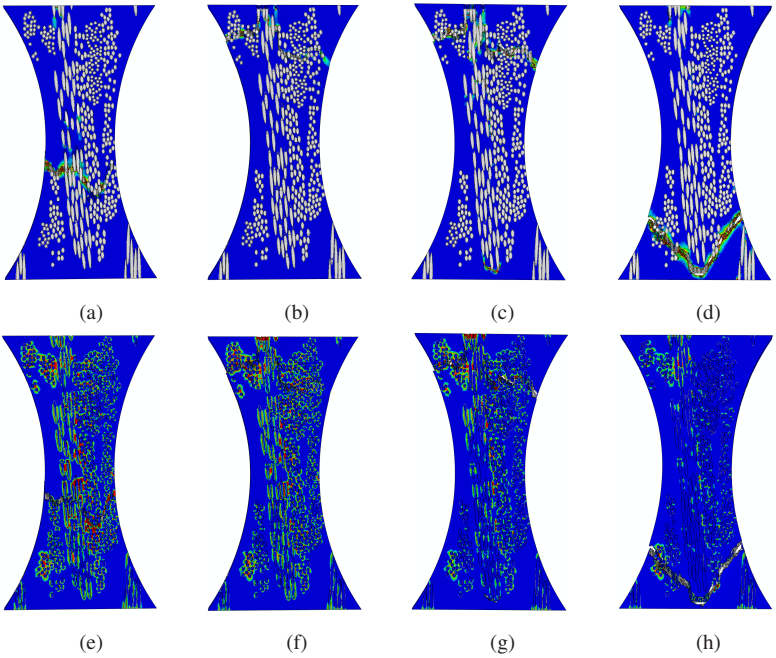

Figure 4.22: Stiffness degradation of the matrix (top) and of the interface (bottom) in GF-3: (a,e) $t^c = 100\,\mathrm{MPa}$, $\Gamma^c = 50\,\mathrm{J\,m^{-2}}$, (b,f) $t^c = 100\,\mathrm{MPa}$, $\Gamma^c = 100\,\mathrm{J\,m^{-2}}$, (c,g) $t^c = 200\,\mathrm{MPa}$, $\Gamma^c = 100\,\mathrm{J\,m^{-2}}$, (d,h) $t^c = 300\,\mathrm{MPa}$, $\Gamma^c = 200\,\mathrm{J\,m^{-2}}$

orientation changes significantly between two neighboring fibers. Regarding individual fibers, interface regions subject to shear loading exhibit damage more often than interface regions subject to normal loading.

Specimen GF-5 is investigated by varying the critical traction from $t^c = 50\,\mathrm{MPa}$ to $200\,\mathrm{MPa}$ and the critical separation energy from $\Gamma^c = 50\,\mathrm{J\,m^{-2}}$ to $200\,\mathrm{J\,m^{-2}}$. The obtained results as well as the corresponding experimental result are plotted in Figure 4.23. Here, both the maximum force and strain at fracture increase with increasing values of the varied parameters. In contrast

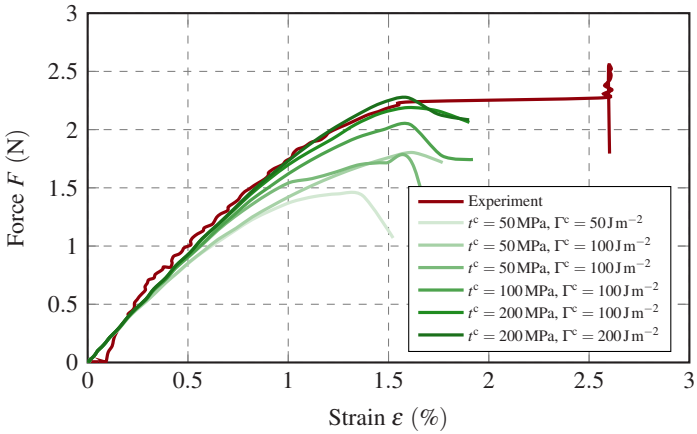

Figure 4.23: Force-strain curves of the physical and numerical tests of specimen GF-5

to GF-3, the initial stiffnesses of the GF-5 simulations suit much better to the experiment. Especially the simulation results with the largest critical traction $t^c = 200\,\mathrm{MPa}$ are close to the experiment, although the separation energy increase from $100\,\mathrm{J\,m^{-2}}$ to $200\,\mathrm{J\,m^{-2}}$ has only minor effect on the resulting force-strain curve.

Figure 4.24 shows the fractured GF-5 models for similar parameter sets as for the GF-3 models. Similar as for GF-3, the location of the final fracture depends on both cohesive zone parameters. Except for regions close to the model boundaries, the matrix damage is concentrated in the regions of final fracture. The degradation of the interfaces show a similar behavior as for GF-3. Especially with a low critical traction of $t^c = 50\,\mathrm{MPa}$, the interface is damaged further the closer the fiber is located to the adjacent ones. However, the sensitivity to a change of fiber orientation is less pronounced than in GF-3. Also, the interfaces' sensitivity to shear loading compared to normal loading

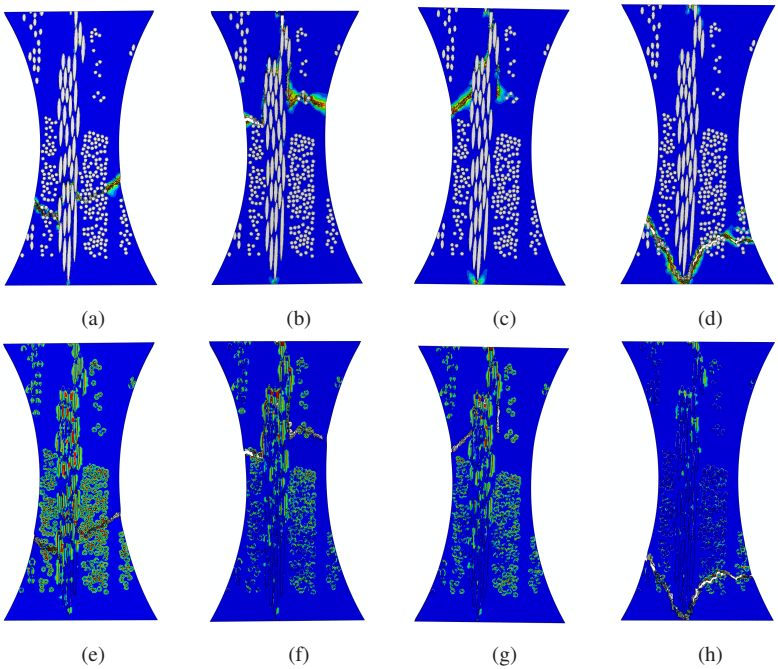

Figure 4.24: Stiffness degradation of the matrix (top) and of the interface (bottom) in GF-5: (a,e) $t^c = 50\,\mathrm{MPa}$, $\Gamma^c = 50\,\mathrm{J\,m^{-2}}$, (b,f) $t^c = 100\,\mathrm{MPa}$, $\Gamma^c = 50\,\mathrm{J\,m^{-2}}$, (c,g) $t^c = 100\,\mathrm{MPa}$, $\Gamma^c = 100\,\mathrm{J\,m^{-2}}$, (d,h) $t^c = 200\,\mathrm{MPa}$, $\Gamma^c = 100\,\mathrm{J\,m^{-2}}$

is less pronounced in GF-5, or at least exceeded by the fiber agglomeration effects on the interface damage behavior.

The specimen GF-6 is analyzed accordingly with varied critical tractions from $t^c = 50\,\mathrm{MPa}$ to $200\,\mathrm{MPa}$ and varied critical separation energies from $\Gamma^c = 50\,\mathrm{J\,m^{-2}}$ to $200\,\mathrm{J\,m^{-2}}$. Since this specimen features the lowest fiber volume fraction of all tested specimens, the interface variation has a smaller effect on the obtained force-strain curves plotted in Figure 4.25, where all curves lie in a narrow range close to the experiment. However, the effect of

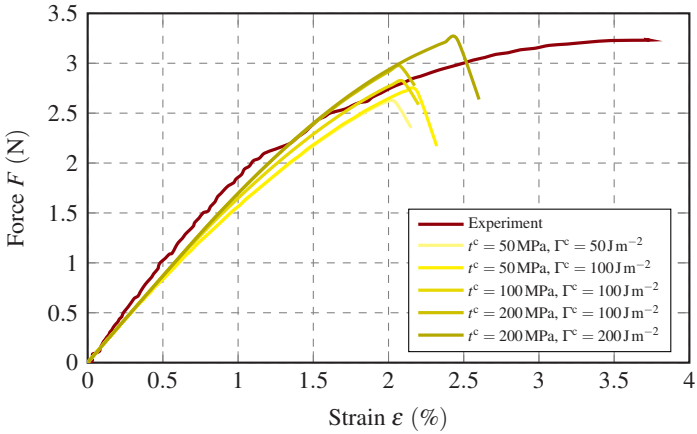

Figure 4.25: Force-strain curves of the physical and numerical tests of specimen GF-6

the separation energy increased at constant critical traction is well visible, as is postpones the final fracture by extending the force-strain curve. The specimens finally fail in a very narrow strain range between 2.05 % and 2.2 %, only exceeded by the parameter paring $t^c = 200\,\mathrm{MPa}$ and $\Gamma^c = 200\,\mathrm{J\,m^{-2}}$, which fails at almost 2.5 % total strain.

In line with the force-strain curves, the fractured specimen show only little variation in the crack paths and the interface damages. All models fracture in the specimen center. The damage initiates in the fiber bundle and propagates to the specimen edges via the polymer matrix. This fracture path, however, is not completely perpendicular to the loading direction – as observed in the physical experiment in Figure 3.26 –, but significantly skewed. Especially regarding the parameter set $t^c = 200\,\mathrm{MPa}$ and $\Gamma^c = 200\,\mathrm{J\,m^{-2}}$ (Figure 4.26d), but also clearly visible in $t^c = 50\,\mathrm{MPa}$ and $\Gamma^c = 50\,\mathrm{J\,m^{-2}}$ (Figure 4.26a), the polymer is concurrently damaged in two directions, shaping an X-like fracture region.

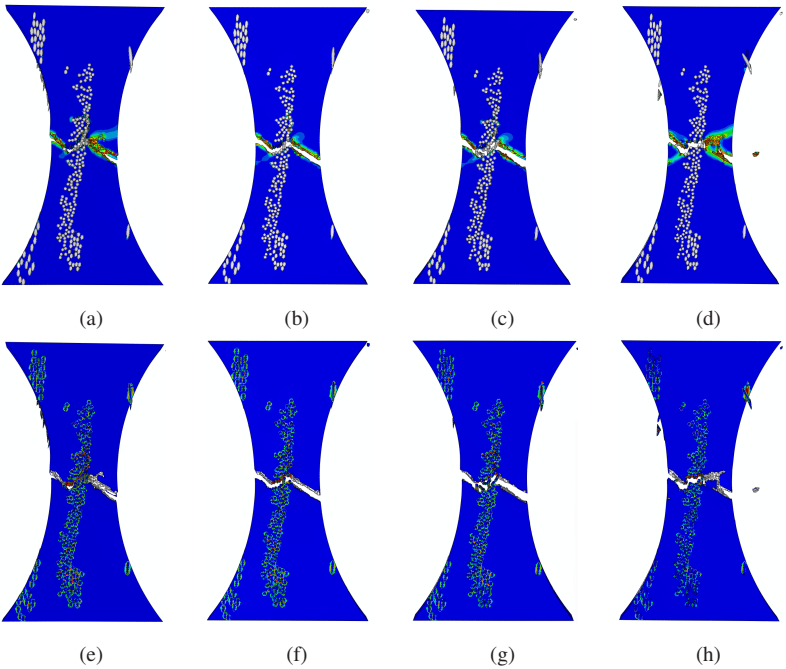

Figure 4.26: Stiffness degradation of the matrix (top) and of the interface (bottom) in GF-6: (a,e) $t^c = 50\,\mathrm{MPa}$, $\Gamma^c = 50\,\mathrm{J\,m^{-2}}$, (b,f) $t^c = 50\,\mathrm{MPa}$, $\Gamma^c = 100\,\mathrm{J\,m^{-2}}$, (c,g) $t^c = 100\,\mathrm{MPa}$, $\Gamma^c = 100\,\mathrm{J\,m^{-2}}$, (d,h) $t^c = 200\,\mathrm{MPa}$, $\Gamma^c = 100\,\mathrm{J\,m^{-2}}$

The degradation of the interface stiffness shows only minor differences between the simulations. In fact, except for the parameter set $t^c = 200\,\mathrm{MPa}$ and $\Gamma^c = 200\,\mathrm{J\,m^{-2}}$ where the interface damage is generally smaller, the simulations are hardly distinguishable in terms of interfacial damage, which is only critical directly in the fracture region.

Variation of the t_n^c/t_s^c -ratio

In order to analyze the influence of the interface sensitivity to the loading mode, the ratio between the critical traction in normal and in shear direction t_n^c/t_s^c is varied. Simultaneously, the ratio of the corresponding sepa-

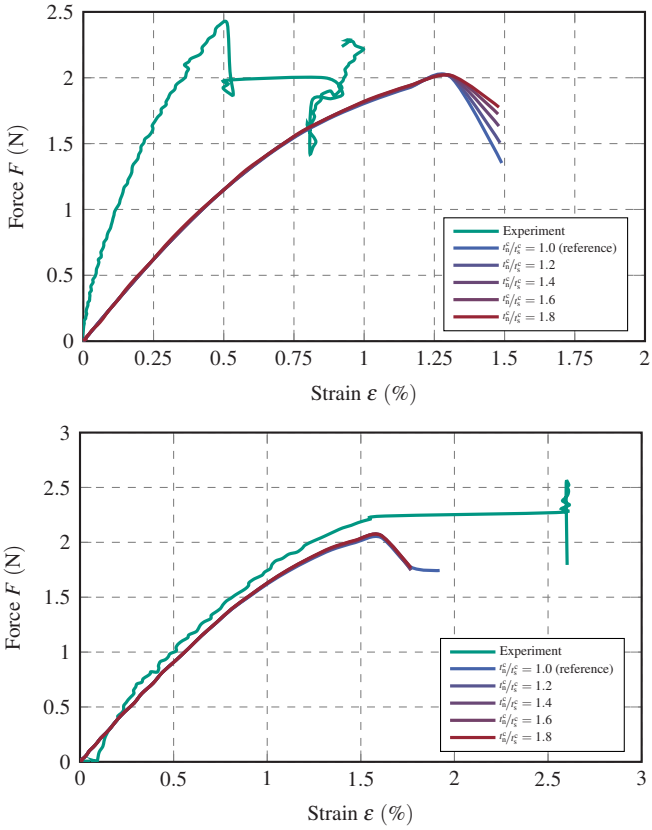

Figure 4.27: Simulation results of GF-3 (top) and GF-5 (bottom) with varied t_n^c/t_s^c -ratios

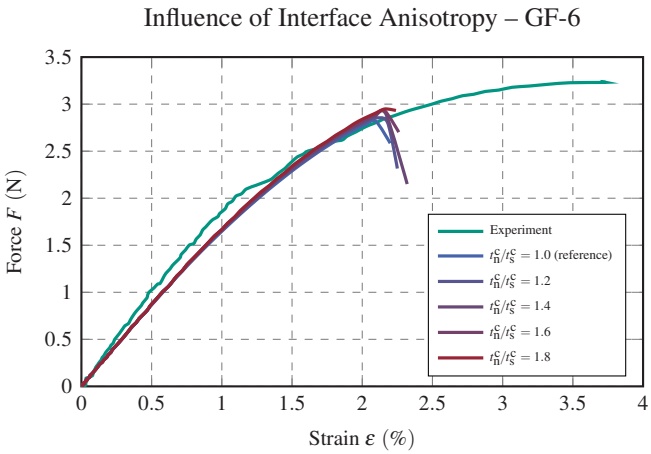

Figure 4.28: Simulation results of GF-6 with varied t_n^c/t_s^c -ratios

ration energies Γ_n^c/Γ_s^c is varied in the same range. Based on the parameter set $t^c = 100\,\mathrm{MPa}$ and $\Gamma^c = 100\,\mathrm{J\,m^{-2}}$, the ratios $t_n^c/t_s^c = \{1.2\}, \{1.4\}, \{1.6\}, \{1.8\}$ are analyzed. The resulting force-strain curves are plotted in Figures 4.27 and 4.28.

None of the investigated parameter sets results in a force-strain curve which deviates noticeably from the original cohesive formulation. Solely the extent of the post-failure force decrease shows a slight variation by a smaller decrease with an increasing mode ratio. Similar results are shown by the fractured models, as plotted in Figures 4.29 and 4.30. Neither the degradation of the polymer matrix nor the degradation of the interface stiffness show a substantial sensitivity to the mode distinction.

Influence of post-failure friction between fibers and matrix

The effect of post-failure friction between the fibers and the matrix is analyzed by means of the model GF-3 assuming a constant friction coefficient of $\mu = 0.5$. The results are plotted in Figure 4.31 with dashed lines and in comparison to its frictionless counterparts plotted with continuous lines. The additional friction causes slightly higher maximum forces regarding the parameter sets $t^c = 200\,\mathrm{MPa}$ and $\Gamma^c = 50\,\mathrm{J\,m^{-2}}$ and $t^c = 200\,\mathrm{MPa}$ and $\Gamma^c = 100\,\mathrm{J\,m^{-2}}$, for which the fractured models in Figure 4.22 indicate interface failure.

Considerations of Pre-Cracks

Since the physical specimens GF-3 and GF-5 contained micro-cracks prior to testing which became part of the final crack path in the course of the experiment, a discrepancy between the physical and the numerical fracture behavior is probable. Therefore, a first attempt to model these pre-cracks is undertaken: since the physical pre-cracks are mainly located along fiber-

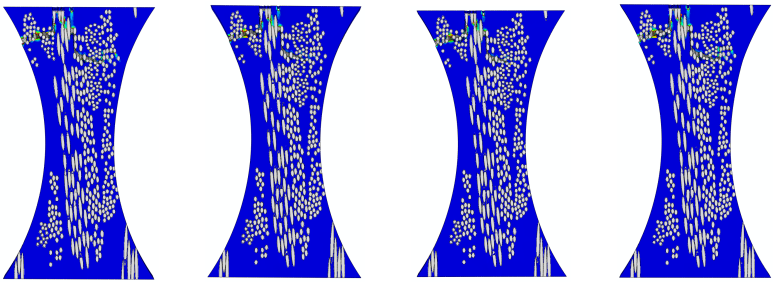

(a) (b) (c) (d)

Figure 4.29: Matrix stiffness degradation in GF-3: (a) $t_n^c/t_s^c = 1.2$, (b) $t_n^c/t_s^c = 1.4$, (c) $t_n^c/t_s^c = 1.6$, (d) $t_n^c/t_s^c = 1.8$

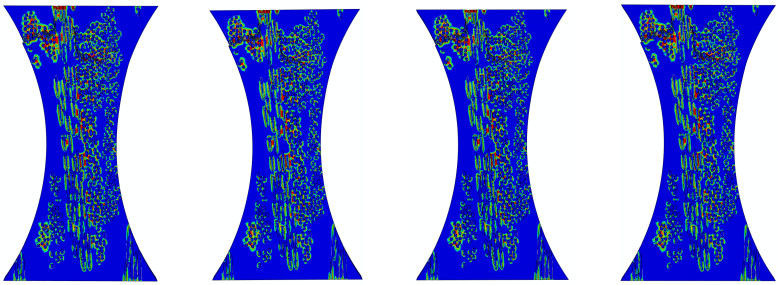

(a) (b) (c) (d)

Figure 4.30: Interface stiffness degradation in GF-3: (a) $t_n^c/t_s^c = 1.2$, (b) $t_n^c/t_s^c = 1.4$, (c) $t_n^c/t_s^c = 1.6$, (d) $t_n^c/t_s^c = 1.8$

matrix interfaces, the cohesive zones in the numerical model are excluded on the corresponding numerical fiber-matrix interfaces. Thus, load transmission is disabled in these regions, which resembles a pre-crack. This approach neglects matrix-cracking prior to testing. The resulting force-strain curves are plotted in the Figure 4.32 with dashed lines regarding both GF-3 and GF-5. For comparison, their unharmed counterparts are also plotted in the figures with continuous lines.

The effect of the disabled fiber-matrix interfaces on the resulting force-strain curves is very limited for both models GF-3 and GF-5. Only the parameter pair $t^c = 100\,\mathrm{MPa}$ and $\Gamma^c = 100\,\mathrm{J\,m^{-2}}$ in GF-3 (Figure 4.32 top) shows a small decrease of the applied force after the initiation of damage. In a similar way, the fracture patterns show only minor differences between the pre-cracked and the intact specimens.

4.3.3 Interlaminar Fracture Toughness Test

The microscale fracture propagation is analyzed with different cohesive zone parameters for the fiber-matrix interfaces. Using identical parameters for

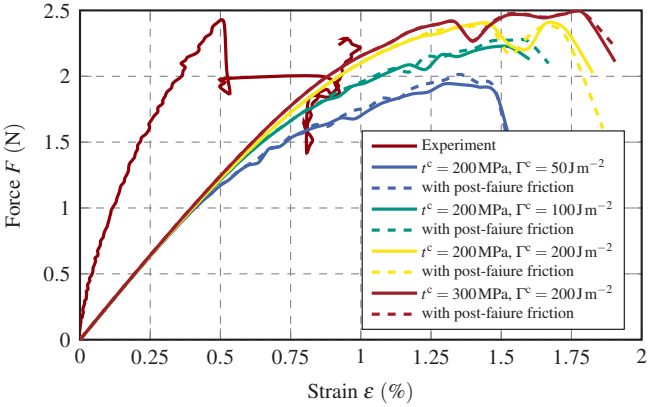

Figure 4.31: Consideration of post-failure friction between the fibers and the matrix in GF-3

the normal and the shear direction of the cohesive zones, the critical traction is varied from t^c =20 MPa to 150 MPa and the critical separation energy is varied from Γ^c =20 J m^{-2} to 150 J m^{-2}. Furthermore, the effect of post-failure friction is analyzed by means of the parameter set $t^c = 50$ MPa and $\Gamma^c = 70\,\mathrm{J\,m^{-2}}$. The influence of the interface parameters on the fracture behavior is evaluated by the external work under the displacement boundary condition and by the energy dissipated due to plastic flow as well as material and interface damage, both with respect to the maximum normal displacement. Additionally, the visual fracture behavior of the model is taken into account.

The results of the parameter variation are plotted in Figure 4.33 with respect to the external work carried out by the displacement boundary condition and the energy dissipated due to damage and plastic flow of the matrix. The external work as well as the dissipated energy increase with increasing critical traction. An increase of a low separation energy has an increasing

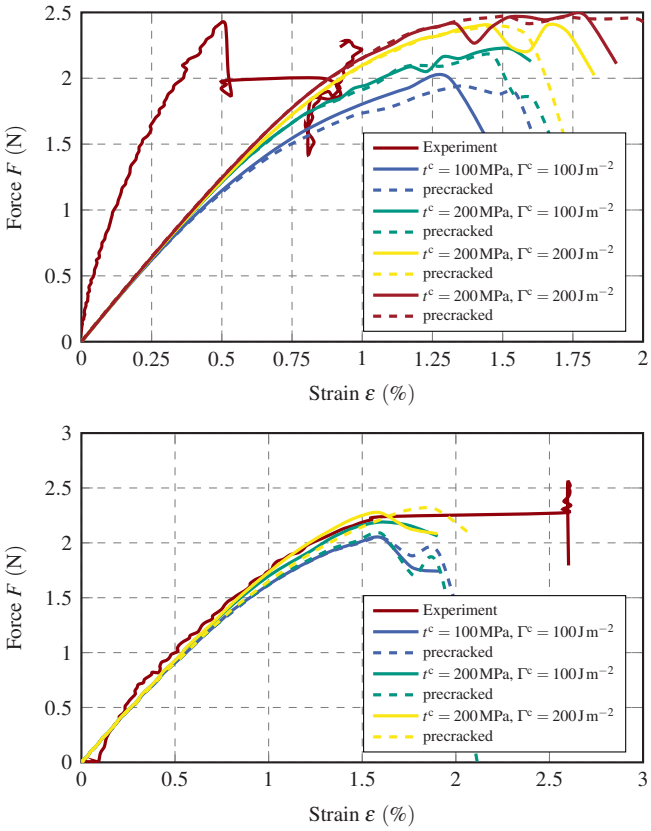

Figure 4.32: Consideration of existing pre-cracks in GF-3 (top) and GF-5 (bottom)

effect on the external work and on the dissipated energy; however, this effect is inversed regarding the analyzed parameter sets with a high critical traction of $t^c = 150\,\mathrm{MPa}$. The beginning of energy dissipation due to plastic flow and fracture is related to the critical traction of the cohesive zones, whereas a higher critical traction leads to a later onset of energy dissipation. Post-failure

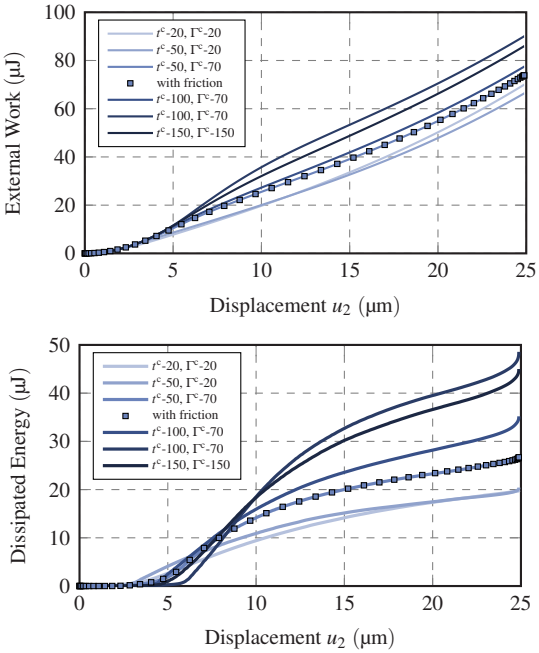

Figure 4.33: Parameter variation of the cohesive zones representing fiber-matrix interfaces with respect to the normal displacement of the applied boundary condition: (top) external work of the displacement boundary condition and (bottom) dissipated energy due to fracture and plastic flow

friction between the fibers and the matrix does neither contribute to the external work nor to the dissipated energy of the considered model. Instead, the results are equivalent to the results of the corresponding frictionless model, indicating that no longitudinal fiber displacement relative to the matrix (such as fiber pull-out) take place.

The fracture behavior for the parameter set $t^c = 50\,\mathrm{MPa}$ and $\Gamma^c = 70\,\mathrm{J\,m^{-2}}$ is visually shown in Figure 4.34. Here, the model is cut slightly behind the

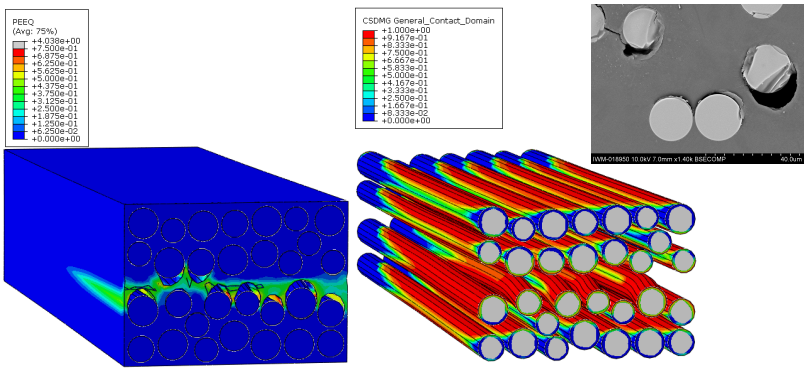

Figure 4.34: Microscale model with the cohesive zone parameters $t^c = 50\,\mathrm{MPa}$ and $\Gamma^c = 70\,\mathrm{J\,m^{-2}}$, showing plastic flow of the fiber surrounding matrix (left) and fiber-matrix debonding (middle) and a comparable SEM image

modeled pre-crack tip which illustrates the state just before the macroscopic crack front. Specifically, the plastic flow of the matrix is plotted on the left and the stiffness degradation of the fiber-matrix interfaces is plotted on the right. The plots show how the fiber-matrix interface failure precedes the matrix failure. The numerical fracture behavior is similar to the fracture behavior of the actual fracture toughness specimen, as observed by SEM imaging. However, the interfaces in the numerical model seem to have failed to a large extent than the interfaces shown in the SEM image. The simulation shows failed fiber-matrix interfaces not only in the region of the horizontal crack, but also further away from the crack. Furthermore, not only the fiber sides facing the pre-crack are damaged, but also the sides facing in the opposite direction are damaged.

A plane cohesive zone in the microscale model shall represent the obtained mixed-interface-matrix failure behavior in order to be used as the cohesive zone formulation of the cell-structured mesoscale model. There-

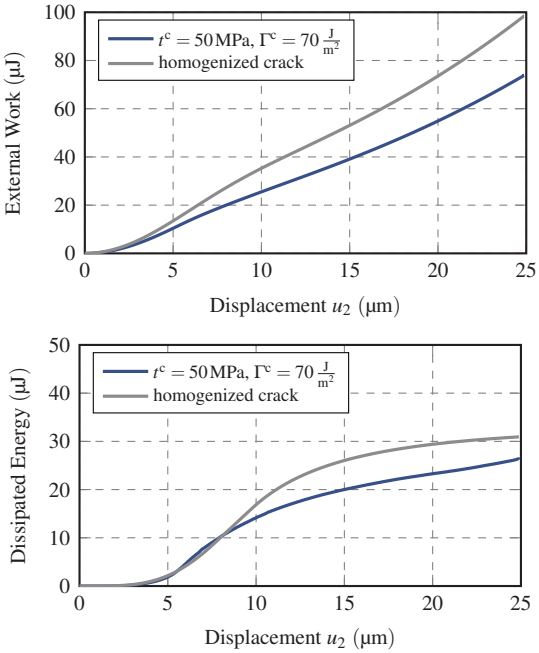

Figure 4.35: Homogenization by a single, plane cohesive zone representing the mixed-interface-matrix failure behavior, compared to the $t^c = 50\,\mathrm{MPa}$ and $\Gamma^c = 70\,\mathrm{J\,m^{-2}}$ fiber-matrix model regarding (top) the external work and (bottom) the dissipated energy

fore, the cohesive zone parameters suiting the external work and the energy dissipation of the micro-scale fiber-matrix model are identified. Figure 4.35 shows a comparison of the fitted single cohesive zone to the results of the $t^c = 50\,\mathrm{MPa}$ and $\Gamma^c = 70\,\mathrm{J\,m^{-2}}$ fiber-matrix model. The single cohesive zone results in higher external work, which indicates a larger model stiffness than the fiber-matrix model. Furthermore, the overall dissipated energy is higher although its initial evolution fits well to the fiber-matrix model.

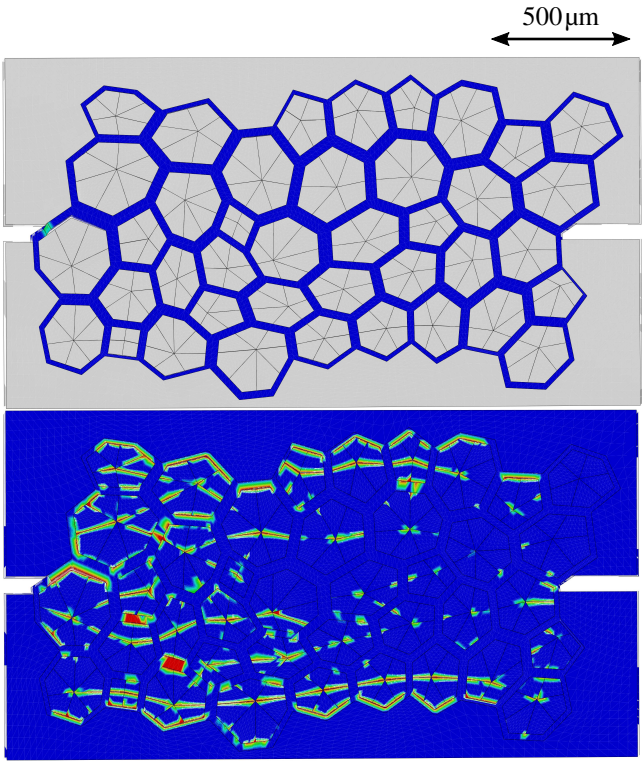

Figure 4.36: Fracture of the mesoscale sub-model: initiated damage in the cell surrounding matrix (top) and propagated damage in the cohesive zones of the mesoscale sub-model (blue: no damage, red: complete failure)

The cohesive zone formulation representing the mixed-interface-matrix failure of the microscale model subsequently is transferred into the cell-structured mesoscale sub-model, on which the displacement boundary conditions according to the macroscale crack propagation of the DCB test are applied. An example sub-model consisting of 40 Voronoi cells on a width of 2 mm and a height of 1 mm is shown in Figure 4.36 at the initiation of

fracture, where the top image illustrates the damage of the polymer surrounding the bundle and the bottom image illustrates the damage of the cohesive zones within the bundles. Again, damage is plotted from blue, indicating no damage, to red, indicating complete failure. Only minor damage effect are observed within the cell surrounding polymer matrix, that is near the left hand gap region of the embedment. In contrast, damage concurrently initiates in multiple cohesive surfaces both within individual cells and along the border of individual cells. The majority of the damaged cohesive zones are oriented approximately horizontally. An emerging crack can be detected almost through the entire cell row towards the bottom of the Voronoi range. The topmost cell row shows a similar emerging crack, yet less pronounced. Between those to widely spread emerging cracks, several cohesive zones showing initiated damage indicating small emerging cracks near the midplane of the cell structure. In general, no relationship between the size of a bundle and its fracture initiation is observed.

As the global crack propagates further and the model is further pulled apart, both polymer damage and cohesive damage further propagates (Figure 4.37). The general distribution of damage over the 40 cells does not significantly change. Hence, the damage pattern of the cell structure remains approximately constant once damage has initiated, while the near horizontally oriented cohesive zones dominate the damage of the structure. The structure finally fractures due to polymer failure between the bundles and cohesive failure – both through individual cells and along cell boundaries – in the bottommost cell row. Hence, the crack path is significantly deflected in the cell structure. The final crack path branches out, especially where it changes its direction significantly. However, these branches arrest when they reach the polymer rich area between the fiber bundles. Furthermore, secondary cracks consisting of completely failed cohesive zones as well as failed polymer areas are also observable – for instance from the left gap

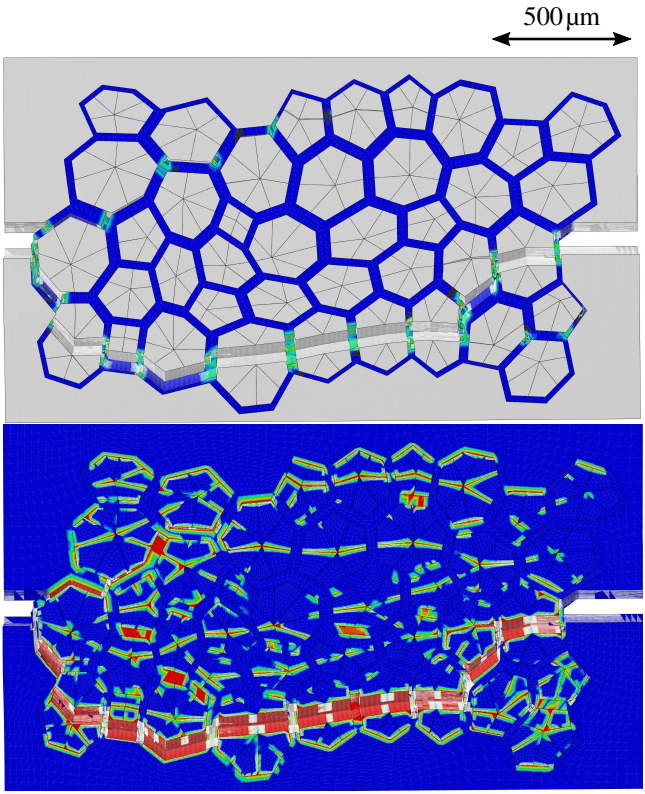

Figure 4.37: Ultimate fracture of the mesoscale sub-model in the cell surrounding matrix (top) and in the cohesive zones (bottom; blue: no damage, red: complete failure)

region of the embedment via cell boundaries and through the polymer to the next cell. However, all of these secondary cracks arrest somewhere in the pure polymer. The polymer is only damaged in some regions, especially along the final crack path and along few secondary crack paths. Most of the pure polymer between the bundles, however, remains undamaged. Since the amount of the damaged cohesive zones has not significantly changed from

Figure 4.36 to Figure 4.37, but the regions of damaged polymer has increased significantly, the occurring fracture has not propagated from one cell to the neighboring cell. Instead, cohesive damage initiates within an individual cell independently from other cells. Fractured cells contribute to the final fracture path only when the polymer region between these cells fails as well. Otherwise, the damage arrests at the polymer and creates a secondary or branched crack.

5 Discussion

The following sections discuss the results of the experimental and numerical investigations described in the Chapters 3 and 4 with respect to the state of research discussed in Chapter 2. The three considered material scales are discussed separately, whereas the discovered connections between the different experimental approaches is concluded in the Chapter 6.

5.1 Single-Fiber Microbond Test

In the physical microbond tests, all specimens show a steady and linear force increase with respect to the crosshead displacement and the droplets debond abruptly without prior decline of the specimen stiffness, as observed in Figure 3.19. Hence, a nucleating interfacial crack propagates immediately in an unstable manner. The theoretical force-displacement curve as shown in Figure 2.6a, on the other hand, investigates the propagation of the interface debonding. For this reason, a direct comparison of the obtained experimental curves to the theoretical curve as well as the theoretical evaluation scheme is not possible.

The reason for the deviation of the obtained force-displacement curve from the theoretical curve is the loading situation of the specimens within the used test set-up. In order to minimize fiber misalignments and offsets between the fiber fixation and the perforated sheet stripping off the polymer droplet, the test set-up requires a sufficient free fiber length between its

fixation and the droplet. Hence, the applied load has to be transfered into the droplet by a fiber which is several magnitudes longer than the droplet size. The elastic energy stored in the fiber thus is large in relation to the energy dissipated by the debonding propagation. Consequently, the elastic energy released at the onset of debonding leads to an unstable debonding propagation and thus to the observed sudden interface failure. The amount of the elastic energy stored in the loaded fiber is emphasized in the moment of debonding by the fiber springing back far beyond its initial position (Section 3.2.1). Even though this behavior was only observed in experiments on specimens prepared in inert gas, it is very likely that this procedure also applies to the experiments on specimens prepared in air. Since much lower maximum forces were achieved here, the spring-back effect might just not be as clearly visible as during the experiments on specimens prepared in argon. As a consequence of the back-springing fibers and the impossibility to directly observe the debonding droplet, any recorded post-failure forces cannot be linked to fiber-matrix interface properties, since the forces' root causes cannot be identified – hence the assumption the perforated sheet displacing the droplet along the fiber causes the forces cannot be proved.

Since the polymer was heat treated three times to prepare the microbond specimen – melt spinning, fiber stretching, and droplet formation – possible polymer degradation must be considered. The discoloration of the droplets observed in any experiments indicates that the polymer degraded to a certain extent throughout the preparation procedure. Especially the severe discoloration of the specimens prepared in air as well as their low mean interfacial shear strength $\bar{\tau}_{ult}$ obtained indicate that the polymer has degraded noticeably. However, also the specimens prepared with flushed argon are slightly discolored. Since a noticeable oxygen residue remained in the oven while being flushed with argon, the polymer degradation cannot be solely related to the pretreatments melt spinning and fiber stretching. To the authors knowledge,

none of the available literature on microbond experiments specifically analyzes the effect of the actual atmosphere composition during the specimen preparation. Hence, the possibility that literature experiments conducted with oxygen residues comparable to the atmosphere described in this thesis cannot be ruled out and the validity of the obtained interface strength results remains unclear.

Regardless of the influence of polymer degradation on the test results, the derivation of cohesive zone parameters for numerical simulations is ambiguous for several reasons. First, using the experimentally obtained mean interfacial shear strength $\bar{\tau}_{\mathrm{ult}}$ for the damage initiation criterion of the numerical simulation results in lower ultimate forces. In other words, the numerically obtained mean interfacial shear strength $\bar{\tau}_{\mathrm{ult}}$ is lower than the experimentally obtained one. Secondly, the maximum force in the experiments can be obtained numerically by a wide range of parameter sets. Hence, a further distinction between the interfacial shear strength on the one hand and the interfacial crack initiation and propagation on the other hand is necessary, if the proper determination of model parameters is the reason for the experimental investigation. However, this is not possible with the test configuration used for this thesis. Even a cyclic loading-unloading test procedure – such as the procedure described for push-out tests by Mueller et al. (2013) – would not contribute to a further distinction between the strength and the fracture initiation and toughness of the interface, since the specimen displacements at the perforated sheet remain unknown. Furthermore, the numerical simulations use material properties for the polymer obtained by macroscopic experiments, usually by means of injection molded tensile test specimens. Thus, the material model does not necessarily represent the material properties of the microscopic droplet due to its much smaller scale and its unique preparation process. Especially when the polymer is assumed to degrade during the specimen preparation, the validity of the fitted cohesive

zone formulation becomes questionable. For these reasons, it appears that the single-fiber microbond test is an inappropriate method to characterize interfacial debonding and to derive model parameters for numerical simulations and that other test methods are preferable.

5.2 Multi-Fiber Tensile Test

The multi-fiber tensile tests reveal the microscopic fracture behavior of the investigated, discontinuous fiber reinforced material due to transverse loading. The analyzed specimens – each with a unique microstructure – fracture under tensile loading in unique modes depending on the specimens' fiber distributions and fiber orientations. However, common principles governing the fracture behavior exist in all investigated specimens: first, cracks initiate in densely packed fiber bundles with out-of-plane orientation; cracks reaching through a whole bundle arrest at pure-matrix regions or fiber bundles with a significantly different orientation; fiber bundles oriented towards the loading direction do not fracture but deflect the crack path; ultimate fracture occurs when multiple cracks merge by rupturing through the polymer regions. Although some specimens feature cracks in dense fiber bundles prior to testing – presumably caused by incautious handling during the μCT scanning process – the basic fracture principles remain. In fact, precracked specimens emphasize the importance of the matrix behavior in preventing the crack propagation: pre-damaged fiber bundles show a crack opening during loading, yet the crack length does not increase until it suddenly merges with another crack. Beyond that, polymer-rich specimens show another interesting behavior of the used UPPH resin: with increasing strain, shear bands arise at cracked fiber bundles in 45° to the loading direction; however, ultimate failure occurs by brittle fracture perpendicular to the loading direction.

The numerical modeling of the specimens reveals the limitations of the applied fiber tracking algorithm for μCT data. The algorithm partially fails in the distinction of fibers in densely packed bundles, which requires manual pre-processing of the models created based on the tracked fiber data. Hence, the numerical models slightly deviate from their physical counterparts in terms of the amount and the exact location and orientation of the contained fibers.

To reach the maximum forces comparable to the physical experiments, the cohesive zones representing the fiber-matrix interfaces in the numerical model have to be set to high strength and toughness values, which even exceed the strength of the pure polymer. Consequently, the extent of failing interfaces decreases with increasing strength and toughness values, while the extent of polymer failure increases. Furthermore, the paths of the final fracture change significantly as the dominating failure type changes from interface to matrix failure. However, the fracture paths of the numerical models do not exactly match their physical counterparts. The difference between the numerical and the physical fracture paths increases with the fiber volume fraction V_f of the corresponding specimen. Nonetheless, the common principles governing the fracture behavior observed in the experimental investigation – fracture is driven by the interfaces; cracks initiate within fiber bundles and arrest at pure-matrix regions; final fracture due to polymer rupture – are generally represented by the numerical simulations. Since the numerical models lack fibers in densely packed regions, the fiber paths through or alongside densely packed fiber bundles differ from the paths observed in the physical specimens. The crack paths most similar to the physical specimens are obtained by models featuring the critical traction $t^\mathrm{c} = 100\,\mathrm{MPa}$ and the critical separation energy $\Gamma^\mathrm{c} = 100\,\mathrm{J\,m^{-2}}$. However, these models underestimate the ultimate force-to-failure.

A possible reason why the reaction force of the simulation does not represent the physical experiment might be found in the material model implemented for the UPPH resin. The general importance of the matrix is well shown by the so-called "precracked" models, which shall represent the specimens damaged prior to testing: here, the fiber-matrix interactions related to the pre-crack are deactivated, yet the matrix is kept intact. The such adapted models result in almost identical force-strain curves and fracture patterns. Hence, the deactivated fiber-matrix interactions are practically completely compensated by the surrounding matrix. In general, the plastic flow of the polymer is properly modeled regarding the dovetail tensile test as well as regarding the multi-fiber tensile test, which is illustrated by the arising shear bands in pure matrix regions (Figures 3.26 and 4.26). However, the following brittle fracture of the polymer perpendicular to the loading direction is not reproduced by the model. Instead, the model fractures in the direction of the shear bands. However, it is not apparent if the force deviation from the physical experiment is caused by an insufficient model composition or by diverging material properties of the neat UPPH resin used for the matrix characterization, which was adapted to be processable without fibers.

5.3 Interlaminar Fracture Toughness Test

The highly scattering results of the interlaminar fracture toughness investigations can most probably be explained by the combination of the materials microstructure and the fundamental hypothesis of the conducted experiments. The double cantilever beam test as a characterization method for CoFRP, for example, was originally defined by transferring the fundamentals of test methods for adhesively bonded metallic sheets (Grellmann and Seidler, 2013). Since the adhesive layer is compliant and weak compared to metal,

the crack is constrained to propagate between the two metallic sheets, leading to a plane, smooth crack path. The experiments conducted in this thesis, however, shall characterize the lamina interfaces of thermoplastic tapes. Within such tapes, the fibers appear in densely packed fiber bundles, which results from their manufacturing process impregnating spread fiber rovings with a thermoplastic matrix. Since the thermoplastic matrix is melted and thus flowable during the consolidation process, the lamina interfaces vanish and the fiber bundles are relocated as they follow the paths of least resistance. Consequently, the resulting microstructure features an irregular distribution of the fiber bundles rather than an ordered stacking sequence of the tapes. Correspondingly, the crack does not propagate along a planar and smooth path, but follows a rough and ragged path through the microstructure.

Scanning electron microscopy images of cross-sections in front of the macroscopic crack front show, that the fracture concurrently initiates within several densely packed fiber bundles. These micro-cracks merge via fiber-matrix interfaces, following a path which is not the shortest, but features a high amount of interfaces and only few small regions of pure matrix. Hence, the driving factor of the fracture propagation is the fiber-matrix interface. This fracture behavior results in a very rough fracture surface. Furthermore, the fiber bundles are not aligned perfectly horizontally, which can cause a deflection of the crack path and consequently fiber bridging. In case such fiber bridges carry load, the obtained fracture toughness is strongly affected. Although this fracture behavior complicates the quantification of the fracture toughness, it certainly leads to an increased toughness and hence to a favorable failure behavior compared to a smooth and planar crack propagation.

The numerical multi-scale modeling of the experiment is able reproduce the general fracture behavior, which was determined based on fractographic SEM images. On the microscale, this includes fiber-matrix interfaces failing

long before the embedding polymer fails. The cell-structured mesoscale sub-model shows a fracture behavior which is qualitatively similar to the observed experimental fracture behavior: microcracks initiate within fiber bundles and merge to a meso- or macrocrack by failing pure-polymer regions, leading to a rough crack path which does not follow the structures mid-plane. Similarly to the SEM observations, damage initiates almost simultaneously in many cells. The number of damaged cells which do not contribute to the ultimate fracture path appears to be larger than the number of secondary or branched cracks observed in the fractographic images. Furthermore, the cell boundaries appear to be damaged to a higher extent than the fiber bundle borders in the physical experiment. However, the microstructure of the specimen may contain more secondary or branched cracks within or around the fiber bundles than SEM can visualize. Provided that the numerical simulation overestimates the number of secondary cracks, a possible explanation for this deviation from the physical experiment may lie in the equal cohesive zone formulation used for inner-cell damage and surrounding cell damage due to a lack of data. Moreover, the statistical variance of the material behavior – regarding elastic as well as fracture properties – is so far not taken into account by the model and can lead to the almost simultaneous fracture in the cohesive zones. Nevertheless, with the high amount of damaged cells, the polymer model shows its ability to reproduce the polymer's crack arresting characteristics observed in the physical experiment.

A general source of error, independent from the model composition, must be assumed in the material model of the neat polymer. Since this model is only derived from a limited data spectrum and without specific experimental microscale characterization, the model definition is equivocal. The polymer model, however, has a large impact not only on the pure polymer region of the mesoscale model, but also on the fracture behavior of the microscale model and therewith on the cohesive zone formulation used in

the mesoscale model. Hence, the deviation of the numerical model to the observed experimental fracture behavior may also be caused – among the reasons described above – by an in some extent insufficiently defined polymer model.

6 Summary and Outlook

Experimental investigations on interfaces in fiber reinforced polymers (FRP) have been conducted on three different scales using three different material compositions: on the microscale, analyzing the fiber-matrix interface in a glass fiber reinforced polypropylene (PP) by means of the single-fiber microbond test; on the mesoscale, analyzing the fiber-matrix interfaces in a discontinuous glass fiber reinforced unsaturated polyester polyurethane hybrid (UPPH) resin by means of the multi-fiber tensile test; and on the macroscale, analyzing the lamina interfaces in continuous glass fiber reinforced polyamide-6 (PA6) tapes by means of interlaminar fracture toughness tests. Each test has been evaluated by means of finite element analyses (FEA).

The experimental investigations conducted reveal major effects of the fiber-matrix interfaces and also of the fiber agglomerations on the fracture behavior of a fiber reinforced composite structure. Modeling the bonding of individual laminae of a thermoplastic multilayer composite as a sharp, plane interface represents the complex interlaminar fracture behavior of such materials in an insufficient manner. The quantification of the strength and toughness of the actual microscopic interface to be used in further mesoscopic and macroscopic numerical simulations of a composite structure is shown to be difficult. Further, the numerical model approaches showed that an adequate material model for the polymer which is valid on the microscale is crucial for a reliable replication of the fracture behavior of fiber-polymer

composites. Polymer material models derived exclusively from macroscopic tensile tests conducted on the pure polymer may not describe the polymer properties in the composite sufficiently and may therefore not be capable of replicating the actual, physical composite material.

This restriction raises the question as to what extent the results of single-fiber microbond tests are transferable into the simulations of macroscopic composite structures. On the one hand, the microbond test is well suitable for a comparative investigation of the fiber-matrix interface, for instance for the development and optimization of fiber sizings. On the other hand, the unique specimen preparation inevitably leads to a material composition which differs from the composition of real composite structures. The magnitude of this difference is dominated by the considered polymer. For polymers requiring elevated pressure and elevated temperature for curing, which applies to most thermosetting resins for structural applications and also to the UPPH resin, the microbond specimens cannot be prepared at all. Furthermore, the investigations reveal the limitations of the microbond test set-up used in this thesis, especially the requirement of a long distance between the droplet and the fiber fixation and the missing opportunity to observe the droplet debonding.

In case the microbond test is not suitable, the multi-fiber tensile test can be an alternative method to characterize the properties of the fiber-matrix interfaces, since it is conducted on specimens extracted from real structures. With this test, the basic principles governing the material's fracture behavior on the mesoscale can be observed in-situ. However, the investigations reveal difficulties arising when densely packed fiber bundles occur in the composite. on the one hand, fiber bundles make the specimen fragile and increase the risk of damage prior to testing. On the other hand, fiber bundles reduce the accuracy of the micro-computed tomography (μCT) based fiber tracking algorithm and thus of the numerical models used to evaluate the experiment.

In the numerical simulations, the models show a fracture behavior similar to their physical counterparts. However, the numerical simulations do not exactly represent the final fracture path, which is caused by inaccurate model geometries. Furthermore, the simulations show their sensitivity to improper material models. Consequently, the accurate evaluation of the multi-fiber tensile test requires thorough understanding of the constituents' microscale characteristics.

The interlaminar fracture toughness has been analyzed in mode I by means of the double cantilever beam test (DCB) and in mode II by means of the end notched flexure test (ENF). The investigation shows that individual layers merge in the consolidation process. Hence, the resulting fracture behavior consists of plastic flow and fracture of the matrix, fiber-matrix interface debonding, and also fiber rupture. The conducted experiments as well as their underlying models, however, do not consider any effects which arise from the tape stacking sequence. Since the rough crack path and the fiber bridging effects are assumed to depend on the realignment of the fiber bundles during the consolidation process, multiaxial tape stacks as well as the amount of layers may affect the fracture behavior by constraining the fiber realignment. As a final consequence of this assumption, however, application-near lay-ups with a thickness of 2 mm or less could not be characterized regarding their interlaminar fracture toughness solely by physical experiments, since a minimum thickness is necessary to ensure sufficiently stiff specimens. Instead, such lay-ups would require further numerical analyzes which takes the actual fiber alignment of the material into account.

A multi-scale approach to analyze such materials is proposed. It models the bundled fiber-matrix composition of the material by means of a Voronoi tessellation as a sub-model of a DCB specimen. This sub-model accounts for a great variety of possible crack paths by incorporated cohesive zones, which

are fitted to the fracture behavior of a numerical fiber-matrix model on the micro-scale. It is able to reproduce the rough crack path and the secondary cracks observed in the physical specimens. However, it does not account for the statistical variation of the fiber density and thus of the variation of the fracture characteristics of the individual fiber bundles, which is a possible field of future work.

In order to enable the existing numerical models to reliably replicate and analyze the material properties, enhanced material models are necessary which allow to predict the polymers' behaviors on the microscale. In case of the UPPH model, changing the fracture criterion from a ductile to a brittle criterion may be a first trial to improve the model. However, since the UPPH model well replicates the initial stiffness as well as the plastic flow observed in the macroscopic experiment, its deviation to the actual behavior on the microscale could not be traced back to either the general model approach or the adaption of the resin composition for the experimental investigation. In order to improve the model and verify it on the microscale, a nano-indentation test conducted experimentally as well as numerically could be an initial approach.

The multi-fiber tensile test on micro tensile specimens was successfully applied to analyze the material's fracture behavior within fiber bundles. Consequently, this test method – combined with the corresponding numerical simulations – is presumably a well working tool to obtain model parameters of homogenized fiber bundles. Analyzing the consolidated tape material in such a way may result in trustworthy parameters for the cell-structured meso-scale model and thus enabling it to further analyze the material properties leading to the highly scattering fracture toughness results.

The limitations of the microbond test set-up – the droplet to load point distance and the missing in-situ observation – could be solved by adapting the multi-fiber tensile test set-up to be used for the microbond test. Due

to its accurate displacement control, the fiber could be clamped close to a knife edge stripping-off the droplet. A magnifying camera system is already attached to the set-up, hence in-situ observation is natively provided. Such a set-up may even provide the opportunity to investigate the interfacial fracture toughness by applying a cyclic loading procedure.

A Experiment Result Data

A.1 Microbond Test Results

Table A.1: Droplet sizes and test results of microbond specimens prepared in air

Specimen	Diameter D_d	Length l_e	τ_{ult}	F_{max}
Air-1	172.3 µm	236.9 µm	3.02 MPa	38.5 mN
Air-2	188.0 µm	254.0 µm	4.37 MPa	58.9 mN
Air-3	160.5 µm	231.7 µm	3.21 MPa	43.2 mN
Air-4	170.1 µm	237.7 µm	4.10 MPa	51.0 mN
Air-5	156.2 µm	228.0 µm	3.14 MPa	36.7 mN
Mean Value	169.4 µm	237.7 µm	3.57 MPa	45.7 mN
Variability	7.3 %	4.2 %	17.4 %	20.2 %

Table A.2: Droplet sizes and test results of microbond specimens prepared with argon

Specimen	Diameter D_d	Length l_e	τ_{ult}	F_{max}
Ar-1	191.2 µm	259.9 µm	10.4 MPa	158.9 mN
Ar-2	174.1 µm	236.2 µm	14.1 MPa	190.1 mN
Ar-3	237.0 µm	306.0 µm	14.8 MPa	268.4 mN
Ar-4	189.1 µm	246.6 µm	13.8 MPa	181.4 mN
Ar-5	194.9 µm	264.4 µm	11.1 MPa	164.7 mN
Ar-6	177.4 µm	247.3 µm	10.4 MPa	147.2 mN
Ar-7	197.6 µm	265.1 µm	13.8 MPa	169.1 mN
Mean Value	194.9 µm	260.8 µm	12.6 MPa	182.9 mN
Variability	10.6 %	8.7 %	15.2 %	22.0 %

A.2 Neat UPPH Test

Table A.3: Cross sections and test results of neat UPPH dovetail tensile test specimens

Specimen	Cross Section	Young's Modulus	Tensile Strength
1	6.45 mm^2	3234 MPa	83.2 MPa
2	6.36 mm^2	3215 MPa	81.0 MPa
3	6.46 mm^2	3184 MPa	77.2 MPa
4	6.48 mm^2	3142 MPa	72.5 MPa
5	6.49 mm^2	3161 MPa	80.5 MPa
6	6.52 mm^2	3081 MPa	76.3 MPa
7	6.35 mm^2	3214 MPa	73.8 MPa
8	6.27 mm^2	3167 MPa	80.5 MPa
9	6.35 mm^2	3182 MPa	79.4 MPa
10	6.28 mm^2	3215 MPa	81.3 MPa
11	6.45 mm^2	3090 MPa	75.2 MPa
Mean Value	6.41 mm^2	3171 MPa	78.3 MPa
Variability	1.4 %	1.6 %	4.4 %

A.3 Interlaminar Fracture Toughness Test Results

Table A.4: Young's Modulus E_{11} 0° to the fiber direction

	24 bar		36 bar		48 bar	
	mean	variab.	mean	variab.	mean	variab.
	MPa	MPa	MPa	MPa	MPa	MPa
260 °C	31 410	1 327	32 735	1 522	31 929	1 113
270 °C	31 379	1 192	32 207	959	32 565	1 177
280 °C	31 639	1 669	33 062	1 177	32 158	1 442

Table A.5: Young's Modulus E_{22} 90° to the fiber direction

	24 bar		36 bar		48 bar	
	mean	variab.	mean	variab.	mean	variab.
	MPa	MPa	MPa	MPa	MPa	MPa
260 °C	4 794	137.5	5 240	71.8	5 479	39.7
270 °C	5 649	230.4	5 266	208.6	5 555	72.5
280 °C	4 930	207.3	5 741	260.0	5 712	197.5

Table A.6: Shear Modulus G_{12}

	24 bar		36 bar		48 bar	
	mean	variab.	mean	variab.	mean	variab.
	MPa	MPa	MPa	MPa	MPa	MPa
260 °C	4 012	279.2	4 626	285.5	4 331	382.5
270 °C	4 557	133.9	4 686	96.9	4 543	457.3
280 °C	4 408	280.4	4 860	85.5	4 965	199.4

Table A.7: Interlaminar Fracture Toughness in mode I $\mathcal{G}_{Ic}$

	24 bar		36 bar		48 bar	
	mean	variab.	mean	variab.	mean	variab.
	$J\,m^{-2}$	$J\,m^{-2}$	$J\,m^{-2}$	$J\,m^{-2}$	$J\,m^{-2}$	$J\,m^{-2}$
260 °C	3 783	1 671	3 518	968	3 124	1 092
270 °C	3 465	1 007	3 553	1 065	2 863	860
280 °C	2 840	1 074	3 245	952	3 334	1 273

Table A.8: Interlaminar Fracture Toughness in mode II $\mathcal{G}_{IIc}$

	24 bar		36 bar		48 bar	
	mean	variab.	mean	variab.	mean	variab.
	$J\,m^{-2}$	$J\,m^{-2}$	$J\,m^{-2}$	$J\,m^{-2}$	$J\,m^{-2}$	$J\,m^{-2}$
260 °C	2 528	455	2 307	333	2 171	231
270 °C	2 433	283	2 174	225	2 566	219
280 °C	2 343	321	2 332	201	2 267	278

Bibliography

Abaqus (2018). *Abaqus 2018 Analysis User's Guide*. Dassault Systèmes, Providence, RI, USA.

Achternbosch, M., Bräutigam, K.-R., Kupsch, C., Reßler, B., and Sardemann, G. (2003). Analyse der Umweltauswirkungen bei der Herstellung, dem Einsatz und der Entsorgung von CFK- bzw. Aluminiumrumpfkomponenten. Wissenschaftliche Berichte FZKA 6879, Forschungszentrum Karlsruhe in der Helmholtz-Gemeinschaft, Karlsruhe.

Ageorges, C., Friedrich, K., Schüller, T., and Lauke, B. (1999). Single fibre broutman test: fibre matrix interface transverse debonding. *Composites Part A: Applied Science and Manufacturing*, 30(12):1423 – 1434.

Amundsen, A. H. (2014). Behaviour and Modelling of Fibre-Reinforced Polymers. Master's thesis, Norwegian University of Science and Technology, Trondheim.

Awal, A., Cescutti, G., Ghosh, S., and Müssig, J. (2011). Interfacial studies of natural fibre/polypropylene composites using single fibre fragmentation test (sfft). *Composites Part A: Applied Science and Manufacturing*, 42(1):50–56.

Berry, J. P. (1963). Determination of fracture surface energies by the cleavage technique. *Journal of Applied Physics*, 34(1):62–68.

Bheemreddy, V., Chandrashekhara, K., Dharani, L., and Hilmas, G. (2013). Modeling of fiber pull-out in continuous fiber reinforced ceramic composites using finite element method and artificial neural networks. *Computational Materials Science*, 79:663 – 673.

Borowski, E., Soliman, E., Kandil, U. F., and Taha, M. R. (2015). Interlaminar fracture toughness of cfrp laminates incorporating multi-walled carbon nanotubes. *Polymers*, 7(6):1020–1045.

Braess, H.-H. and Seiffert, U., editors (2013). *Vieweg Handbuch Kraftfahrzeugtechnik*. ATZ/MTZ-Fachbuch. Springer Vieweg, Wiesbaden, 7. edition.

Bruce, T. P. (2011). *Mechanistic Mixed-Mode Failure Criterion for Continuous Fiber-Polymer Composites*. PhD thesis, The University of Western Ontario, London, ON.

Brylka, B., Fritzen, F., Böhlke, T., and Weidenmann, K. A. (2011). Influence of micro-structure on fibre push-out tests. *Proceedings in Applied Mathematics and Mechanics*, 11(1):141–142.

Bücheler, D. (2018). *Locally Continuous-fiber Reinforced Sheet Molding Compound*. PhD thesis, Karlsruhe Institute of Technology (KIT), Karlsruhe.

Chandra, N. and Ananth, C. (1995). Analysis of interfacial behavior in MMCs and IMCs by the use of thin-slice push-out tests. *Composites Science and Technology*, 54(1):87–100.

Chandra, N. and Ghonem, H. (2001). Interfacial mechanics of push-out tests: theory and experiments. *Composites Part A: Applied Science and Manufacturing*, 32(3):575–584.

Copponnex, T. (1996). Analysis and evaluation of the single-fibre fragmentation test. *Composites Science and Technology*, 56(8):893–909.

Curtis, P. T., Bader, M. G., and Bailey, J. E. (1978). The stiffness and strength of a polyamide thermoplastic reinforced with glass and carbon fibres. *Journal of Materials Science*, 13(2):377–390.

Dittmann, K. (2018). Experimental-numerical characterization of the fiber-matrix interfaces in smc structures (working title). Master's thesis, Karlsruhe Institute of Technology (KIT), Karlsruhe.

Ehrenstein, G. W. (2006). *Faserverbund-Kunststoffe: Werkstoffe – Verarbeitung – Eigenschaften*. Carl Hanser Verlag, München, 2. edition.

Feih, S., Wonsyld, K., Minzari, D., Westermann, P., and Lilholt, H. (2004). Testing procedure for the single fiber fragmentation test. Technical report, Risø National Laboratory, Roskilde, Denmark.

Fliegener, S. (2015). *Micromechanical Finite Element Modeling of Long Fiber Reinforced Thermoplastics*. PhD thesis, Karlsruhe Institute of Technology (KIT), Karlsruhe.

Fliegener, S., Kennerknecht, T., and Kabel, M. (2017). Investigations into the damage mechanisms of glass fiber reinforced polypropylene based on micro specimens and precise models of their microstructure. *Composites Part B: Engineering*, 112:327 – 343.

Fowkes, F. (1981). Acid-base interactions in polymer adhesion. In Georges, J., editor, *Microscopic Aspects of Adhesion and Lubrication*, volume 7 of *Tribology Series*, pages 119 – 137. Elsevier, Paris.

Friedrich, H. E. (2013). *Leichtbau in der Fahrzeugtechnik*. ATZ/MTZ-Fachbuch. Springer Vieweg, Wiesbaden.

Geiger, O., Henning, F., Eyerer, P., Brüssel, R., and Ernst, H. (2006). LFT-D: materials tailored for new applications. *Reinforced Plastics*, 50(1):30–35.

Goda, K., Park, J., and Netravali, A. (1995). A new theory to obtain weibull fibre strength parameters from a single-fibre composite test. *Journal of Materials Science*, 30(10):2722–2728.

Godara, A., Gorbatikh, L., Kalinka, G., Warrier, A., Rochez, O., Mezzo, L., Luizi, F., Van Vuure, A., Lomov, S., and Verpoest, I. (2010). Interfacial shear strength of a glass fiber/epoxy bonding in composites modified with carbon nanotubes. *Composites Science and Technology*, 70(9):1346–1352.

Graf, M. (2016). Verfahrenskombination für verschnittarmes UD-Tapelegen. *Lightweight Design*, 9(1):34–39.

Greenfield, M., Pedicini, A., and Penn, L. (2000). Development of a single fiber fragmentation test for high strain rates. *International Journal of Adhesion and Adhesives*, 20(5):403–407.

Greisel, M., Jäger, J., Moosburger-Will, J., Sause, M., Mueller, W., and Horn, S. (2014). Influence of residual thermal stress in carbon fiber-reinforced thermoplastic composites on interfacial fracture toughness evaluated by cyclic single-fiber push-out tests. *Composites Part A: Applied Science and Manufacturing*, 66:117 – 127.

Grellmann, W. and Seidler, S. (2013). *Polymer Testing*. Carl Hanser Verlag, München.

Groß, D. and Seelig, T. (2018). *Fracture Mechanics : With an Introduction to Micromechanics*. Mechanical Engineering Series. Springer, Cham, Switzerland, 3rd edition.

Hardenacke, V. and Hohe, J. (2009). Local probabilistic homogenization of two-dimensional model foams accounting for micro structural disorder. *International Journal of Solids and Structures*, 46(5):989–1006.

Hardenacke, V. and Hohe, J. (2010). Assessment of space division strategies for generation of adequate computational models for solid foams. *Journal of Mechanical Sciences*, 52(12):1772–1782.

Haspel, B. (2014). *Werkstoffanalytische Betrachtung der Eigenschaften von mittels neuartiger RTM–Fertigungsprozesse hergestellten glasfaserverstärkten Polymerverbunden*. PhD thesis, Karlsruhe Institute of Technology (KIT), Karlsruhe.

He, Y. and Makeev, A. (2014). Nonlinear shear behavior and interlaminar shear strength of unidirectional polymer matrix composites: A numerical study. *International Journal of Solids and Structures*, 51(6):1263–1273.

Henning, F., Ernst, H., and Brüssel, R. (2005). LFTs for Automotive Applications. *Reinforced Plastics*, 49(2):24 – 33.

Henning, F. and Moeller, E. (2011). *Handbuch Leichtbau - Methoden, Werkstoffe, Fertigung*. Carl Hanser Verlag, München.

Heuss, R., Müller, N., van Sintern, W., Starke, A., and Tschiesner, A. (2012). Lightweight, heavy impact – how carbon fiber and other lightweight materials will develop across industries and specifically in automotive. Study, McKinsey & Company, Berlin.

Hodgkinson, J. M. (2000). *Mechanical Testing of Advanced Fibre Composites*. Woodhead Publishing Limited, Cambridge, England, 1st edition.

Hohe, J., Fliegener, S., and Beckmann, C. (2016). Microstructural uncertainties in composites – challenges for homogenization and simulation. In carhs, editor, *Automotive CAE Grand Challenge 2016*, Hanau, Germany.

Hu, P., Shi, Z., Wang, X., Li, W., Zhou, S., and Han, X. (2015). Strength degradation of adhesively bonded single-lap joints in a cyclic-temperature environment using a cohesive zone model. *The Journal of Adhesion*, 91(8):587–603.

Jousset, P. and Rachik, M. (2014). Comparison and evaluation of two types of cohesive zone models for the finite element analysis of fracture propagation in industrial bonded structures. *Engineering Fracture Mechanics*, 132:48–69.

Kachanov, M., Shafiro, B., and Tsukrov, I. (2003). *Handbook of Elasticity Solutions*. Kluwer, Dordrecht [u.a.].

Kalinka, G., Leistner, A., and Hampe, A. (1997). Characterisation of the fibre/matrix interface in reinforced polymers by the push-in technique. *Composites Science and Technology*, 57(8):845–851.

Kallas, M., Koss, D., Hahn, H., and Hellmann, J. (1992). Interfacial stress state present in a "thin-slice" fibre push-out test. *Journal of Materials Science*, 27(14):3821–3826.

Kärger, L., Bölke, T., Weidenmann, K. A., Seelig, T., and Henning, F. (2016). Integrated engineering of continuous-discontinuous long fiber reinforced polymer (CoDiCoFRP) structures in the framework of the International Research Training Group GRK 2078. In Virtual Dimension Center Fellbach, editor, *5. Fachkongress Composite Simulation*, Hamburg.

Kelly, A. and Tyson, W. R. (1965). Tensile properties of fibre-reinforced metals: Copper/tungsten and copper/molybdenum. *Journal of the Mechanics and Physics of Solids*, 13(6):329 – 350.

Kennerknecht, T. (2014). *Fatigue of Micro Molded Materials - Aluminum Bronze and Yttria Stabilized Zirconia*. PhD thesis, Karlsruhe Institute of Technology (KIT), Karlsruhe.

Kerans, R. J. and Parthasarathy, T. A. (1991). Theoretical analysis of the fiber pullout and pushout tests. *Journal of the American Ceramic Society*, 74(7):1585–1596.

Kim, B. W. and Nairn, J. A. (2002). Observations of fiber fracture and interfacial debonding phenomena using the fragmentation test in single fiber composites. *Journal of Composite Materials*, 36(15):1825–1858.

Kim, J. H., Hettenhouser, J. W., Moon, C. K., and Holmes, G. A. (2009). A fiber placement device and methodology for preparing 2-d and 3-d combinatorial microcomposites. *Journal of Materials Science*, 44(14):3626–3632.

Kim, J.-K. and Mai, Y.-W. (1998). *Engineered Interfaces in Fiber Reinforced Composites*. Elsevier, Amsterdam.

Koyanagi, J., Nakatani, H., and Ogihara, S. (2012). Comparison of glass–epoxy interface strengths examined by cruciform specimen and single-fiber pull-out tests under combined stress state. *Composites Part A: Applied Science and Manufacturing*, 43(11):1819–1827.

Krause, W., Geiger, O., Henning, F., and Eyerer, P. (2005). Development of a Technology for Large Scale Production of Continuous Fiber Reinforced Thermoplastic Composites. In of Plastic Engineers, S., editor, *SPE-Conference ANTEC 2005*, Boston, USA.

Krause, W., Henning, F., Tröster, S., Geiger, O., and Eyerer, P. (2003). LFT-D – a process technology for large scale production of fiber reinforced thermoplastic components. *Journal of Thermoplastic Composite Materials*, 16(4):289–302.

Kuboki, T., Hilvo, T., and Jar, P.-Y. (2002). Detection of interlaminar cracks in fiber-reinforced polymers (frp). *Journal of Materials Science Letters*, 21(22):1789–1791.

Kuboki, T., Jar, P.-Y., and Forest, T. (2003). Influence of interlaminar fracture toughness on impact resistance of glass fibre reinforced polymers. *Composites Science and Technology*, 63(7):943–953.

Kuna, M. (2008). *Numerische Beanspruchungsanalyse von Rissen*. Springer, Wiesbaden.

Lässig, R., Eisenhut, M., Mathias, A., Schulte, R., Peters, F., Kühmann, T., Waldmann, T., and Begemann, W. (2012). Serienproduktion von hochfesten Faserverbundbauteilen - Perspektiven für den deutschen Maschinen- und Anlagenbau. Studie, Roland Berger Strategy Consultants, VDMA, München.

Li, S., Thouless, M., Waas, A., Schroeder, J., and Zavattieri, P. (2005). Use of a cohesive-zone model to analyze the fracture of a fiber-reinforced polymer–matrix composite. *Composites Science and Technology*, 65(3-4):537–549.

Li, Z.-F., Grubb, D. T., and Phoenix, S. L. (1995). Fiber interactions in the multi-fiber composite fragmentation test. *Composites Science and Technology*, 54(3):251–266.

Madhukar, M. S. and Drzal, L. T. (1991a). Fiber-matrix adhesion and its effect on composite mechanical properties: I. inplane and interlaminar shear

behavior of graphite/epoxy composites. *Journal of Composite Materials*, 25(8):932–957.

Madhukar, M. S. and Drzal, L. T. (1991b). Fiber-matrix adhesion and its effect on composite mechanical properties: II. Longitudinal (0°) and transverse (90°) tensile and flexure behavior of graphite/epoxy composites. *Journal of Composite Materials*, 25(8):958–991.

Mallick, P. K. (2007). *Fiber-Reinforced Composites – Materials, Manufacturing, and Design*. CRC Press, Boca Raton, FL, 3rd edition.

Marshall, D. B. (1984). An Indentation Method for Measuring Matrix-Fiber Frictional Stresses in Ceramic Composites. *Journal of the American Ceramic Society*, 67(12):259–260.

McCarthy, E. D., Kim, J. H., Heckert, N. A., Leigh, S. D., Gilman, J. W., and Holmes, G. A. (2015). The fiber break evolution process in a 2-d epoxy/glass multi-fiber array. *Composites Science and Technology*, 121:73–81.

Mishnaevsky Jr, L. and Brøndsted, P. (2009). Micromechanical modeling of damage and fracture of unidirectional fiber reinforced composites: A review. *Computational Materials Science*, 44(4):1351–1359.

Mueller, W., Moosburger-Will, J., Sause, M., Greisel, M., and Horn, S. (2015). Quantification of crack area in ceramic matrix composites at single-fiber push-out testing and influence of pyrocarbon fiber coating thickness on interfacial fracture toughness. *Journal of the European Ceramic Society*, 35(11):2981–2989.

Mueller, W., Moosburger-Will, J., Sause, M., and Horn, S. (2013). Microscopic analysis of single-fiber push-out tests on ceramic matrix composites performed with berkovich and flat-end indenter and evaluation of

interfacial fracture toughness. *Journal of the European Ceramic Society*, 33(2):441 – 451.

Naya, F., Lopes, C. S., and González, C. (2016). Computational Micromechanics on Polymer Matrix Composites under different Environments: Longitudinal, Transverse and Shear Ply Properties. In European Society for Composite Materials, editor, *ECCM17 – 17th European Conference on Composite Materials*, Munich, Germany.

Nishikawa, M., Okabe, T., and Takeda, N. (2007). Mechanics of fiber fragmentation in single-fiber composite. In International Committee on Composite Materials, editor, *16th International Conference on Composite Materials ICCM*, Kyoto, Japan.

Nishikawa, M., Okabe, T., and Takeda, N. (2008). Determination of interface properties from experiments on the fragmentation process in single-fiber composites. *Materials Science and Engineering: A*, 480(1-2):549–557.

Ogihara, S. and Koyanagi, J. (2010). Investigation of combined stress state failure criterion for glass fiber/epoxy interface by the cruciform specimen method. *Composites Science and Technology*, 70(1):143–150.

Piggott, M. (1995). A new model for interface failure in fibre-reinforced polymers. *Composites Science and Technology*, 55(3):269 – 276.

Piggott, M. (1997a). Why interface testing by single-fibre methods can be misleading. *Composites Science and Technology*, 57(8):965 – 974.

Piggott, M. (1997b). Why the fibre/polymer interface can appear to be stronger than the polymer matrix. *Composites Science and Technology*, 57(8):853 – 857.

Piggott, M. and Xiong, Y. J. (1994). Visualization of debonding of fully and partially embedded glass fibres in epoxy resins. *Composites Science and Technology*, 52(4):535–540.

Pinter, P. (2018). *Microstructure characterization of continuous-discontinuous fibre reinforced Polymers based on volumetric images*. PhD thesis, Karlsruhe Institute of Technology (KIT), Karlsruhe.

Pisanova, E., Zhandarov, S., and Mäder, E. (2001a). How can adhesion be determined from micromechanical tests? *Composites Part A: Applied Science and Manufacturing*, 32(3):425 – 434.

Pisanova, E., Zhandarov, S., Mäder, E., Ahmad, I., and Young, R. (2001b). Three techniques of interfacial bond strength estimation from direct observation of crack initiation and propagation in polymer fibre systems. *Composites Part A Applied Science and Manufacturing*, 32(3):435 – 443.

Puck, A. and Schürmann, H. (2002). Failure analysis of FRP laminates by means of physically based phenomenological models. *Composites Science and Technology*, 62(12):1633 – 1662.

Puppo, A. and Evensen, H. (1970). Interlaminar shear in laminated composites under generalized plane stress. *Journal of Composite Materials*, 4(2):204–220.

Ramirez, F., Carlsson, L., and Acha, B. (2009). A method to measure fracture toughness of the fiber/matrix interface using the single-fiber fragmentation test. *Composites Part A: Applied Science and Manufacturing*, 40(6-7):679–686.

Rao, V., Herrera-Franco, P., Ozzello, A., and Drzal, L. (1991). A direct comparison of the fragmentation test and the microbond pull-out test

for determining the interfacial shear strength. *The Journal of Adhesion*, 34(1-4):65–77.

Ridha, M., Wang, C., Chen, B., and Tay, T. (2014). Modelling complex progressive failure in notched composite laminates with varying sizes and stacking sequences. *Composites Part A: Applied Science and Manufacturing*, 58:16–23.

Robinson, P. and Hodgkinson, J. M. (2000). *Mechanical Testing of Advanced Fibre Composites*, chapter Interlaminar Fracture Toughness, pages 170–210. Woodhead Publishing Limited, Cambridge, England.

Rodríguez, M., Molina-Aldareguía, J. M., González, C., and LLorca, J. (2012). A methodology to measure the interface shear strength by means of the fiber push-in test. *Composites Science and Technology*, 72(15):1924–1932.

Rösler, J., Harders, H., and Bäker, M. (2012). *Mechanisches Verhalten der Werkstoffe*. Springer Vieweg, Wiesbaden, 4. edition.

Sato, N., Kurauchi, T., Sato, S., and Kamigaito, O. (1984). Mechanism of fracture of short glass fibre-reinforced polyamide thermoplastic. *Journal of Materials Science*, 19(4):1145–1152.

Sato, N., Kurauchi, T., Sato, S., and Kamigaito, O. (1991). Microfailure behaviour of randomly dispersed short fibre reinforced thermoplastic composites obtained by direct sem observation. *Journal of Materials Science*, 26(14):3891–3898.

Scheer, R. and Nairn, J. (1995). A comparison of several fracture mechanics methods for measuring interfacial toughness with microbond tests. *The Journal of Adhesion*, 53(1-2):45–68.

Scheider, I. and Brocks, W. (2003). The effect of the traction separation law on the results of cohesive zone crack propagation analyses. *Key Engineering Materials*, 251:313–318.

Schemmann, M. (2018). *Biaxial Characterization and Mean-field Based Damage Modeling of Sheet Molding Compound Composites*. PhD thesis, Karlsruhe Institute of Technology (KIT), Karlsruhe.

Schober, M., Hohe, J., and Kuboki, T. (2017a). *Combined Macro– and Micro-Mechanical Analysis of Instable Crack Propagarion in Interlaminar Fractgure Toughness Tests*, volume 7 of *GACM Colloquium on Computational Mechanics*, chapter Combined Macro– and Micro-Mechanical Analysis of Instable Crack Propagarion in Interlaminar Fractgure Toughness Tests, pages 665–668. Institute for Structural Mechanics, University of Stuttgart, Stuttgart.

Schober, M., Kuboki, T., Ameri, E., Hohe, J., and Gumbsch, P. (2017b). Effects of Process Parameters on the Interlaminar Fracture Toughness of GF-PA6-Tapes. *Proceedings in Applied Mathematics and Mechanics*, 17(1):273–274.

Schuh, G., Korthals, K., and Arnoscht, J. (2014). Contribution of Body Lightweight Design to the Environmental Impact of Electric Vehicles. *Advanced Materials Research*, 907:329–347.

Schürmann, H. (2007). *Konstruieren mit Faser-Kunststoff-Verbunden*. Springer, Berlin, 2. edition.

Senn, M. and Eberl, C. (2018). Digital image correlation and tracking. Plug-In for Matlab 8.3, Version 2.1.0.0. `https://mathworks.com/matlabcentral/fileexchange/50994-`

digital-image-correlation-and-tracking, last accessed Aug 6, 2018.

Siebenpfeiffer, W., editor (2014). *Leichtbau-Technologien im Automobilbau: Werkstoffe - Fertigung - Konzepte*, Springer Vieweg, Wiesbaden.

Simonovski, I. and Cizelj, L. (2015). Cohesive zone modeling of intergranular cracking in polycrystalline aggregates. *Nuclear Engineering and Design*, 283:139–147.

Swentek, I. N. (2014). *On the Interfacial Fracture Mechanics of Long-fibre Reinforced Polymer Composites*. PhD thesis, The University of Western Ontario, London, ON.

Takahashi, K. and Choi, N.-S. (1991). Influence of fibre weight fraction on failure mechanisms of poly(ethylene terephthalate) reinforced by short-glass-fibres. *Journal of Materials Science*, 26(17):4648–4656.

Taketa, I., Okabe, T., and Kitano, A. (2008). A new compression-molding approach using unidirectionally arrayed chopped strands. *Composites Part A: Applied Science and Manufacturing*, 39(12):1884–1890.

Tandon, G., Kim, R., and Bechel, V. (2002). Fiber–matrix interfacial failure characterization using a cruciform-shaped specimen. *Journal of Composite Materials*, 36(23):2667–2691.

Tandon, G. and Pagano, N. (1998). Micromechanical analysis of the fiber push-out and re-push test. *Composites Science and Technology*, 58(11):1709–1725.

Thielicke, B., Soltész, U., Krenkel, W., and Morawietz, K. (1999). Creep of a C/C-SiC Composite under Interlaminar Shear Loading at High Temper-

atures. In International Committee on Composite Materials, editor, *12th International Conference on Composite Materials ICCM*, Paris, France.

Thielicke, B., Soltész, U., and Unnasch, H. (1994). The Interlaminar Shear Strength (ILSS) of a laminated Carbon/Carbon Composite at Temperatures up to 2000 C. *Proceedings of the ECCMCTS2*, pages 325–332.

Thomason, J. L. (2002). The influence of fibre length and concentration on the properties of glass fibre reinforced polypropylene: 5. Injection moulded long and short fibre PP. *Composites Part A: Applied Science and Manufacturing*, 33(12):1641 – 1652.

Thomason, J. L. (2007). The influence of fibre length and concentration on the properties of glass fibre reinforced polypropylene: 7. Interface strength and fibre strain in injection moulded long fibre PP at high fibre content. *Composites Part A: Applied Science and Manufacturing*, 38(1):210 – 216.

Thomason, J. L. and Vlug, M. A. (1996). Influence of fibre length and concentration on the properties of glass fibre-reinforced polypropylene: 1. tensile and flexural modulus. *Composites Part A: Applied Science and Manufacturing*, 27(6):477 – 484.

Thomason, J. L. and Vlug, M. A. (1997). Influence of fibre length and concentration on the properties of glass fibre-reinforced polypropylene: 4. Impact properties. *Composites Part A: Applied Science and Manufacturing*, 28(3):277 – 288.

Thomason, J. L., Vlug, M. A., Schipper, G., and Krikor, H. G. L. T. (1996). Influence of fibre length and concentration on the properties of glass fibre-reinforced polypropylene: Part 3. Strength and strain at failure. *Composites Part A: Applied Science and Manufacturing*, 27(11):1075 – 1084.

Trauth, A. (2018). *Characterisation and Modelling fo Continuous-Discontinuous Sheet Moulding Compoud Composites for Structural Applications*. PhD thesis, Kalrsruhe Institute of Technology (KIT), Karlsruhe.

Tripathi, D. and Jones, F. (1998). Single fibre fragmentation test for assessing adhesion in fibre reinforced composites. *Journal of Materials Science*, 33(1):1–16.

Yang, L. and Thomason, J. (2012). Development and application of micromechanical techniques for characterising interfacial shear strength in fibre-thermoplastic composites. *Polymer Testing*, 31(7):895–903.

Yu, F., Lu, Z., Luo, H., and Wang, P. (2011). *Three-dimensional model analysis and processing*. Springer Science & Business Media, Berlin Heidelberg.

Zhandarov, S., Gorbatkina, Y., and Mäder, E. (2006). Adhesional pressure as a criterion for interfacial failure in fibrous microcomposites and its determination using a microbond test. *Composites Science and Technology*, 66(15):2610 – 2628.

Zhandarov, S. and Mäder, E. (2005). Characterization of fiber/matrix interface strength: applicability of different tests, approaches and parameters. *Composites Science and Technology*, 65(1):149 – 160.

Zhandarov, S. and Mäder, E. (2014). An alternative method of determining the local interfacial shear strength from force-displacement curves in the pull-out and microbond tests. *International Journal of Adhesion and Adhesives*, 55:37 – 42.

Zhandarov, S. and Mäder, E. (2016). Determining the interfacial toughness from force–displacement curves in the pull-out and microbond tests using

the alternative method. *International Journal of Adhesion and Adhesives*, 65:11–18.

Zhi, C., Long, H., and Miao, M. (2017). Influence of microbond test parameters on interfacial shear strength of fiber reinforced polymer-matrix composites. *Composites Part A: Applied Science and Manufacturing*, 100:55–63.

Zinck, P., Wagner, H., Salmon, L., and Gerard, J. (2001). Are microcomposites realistic models of the fibre/matrix interface? I. Micromechanical modelling. *Polymer*, 42(12):5401–5413.

Zollo, R. F. (1997). Fiber-reinforced concrete: an overview after 30 years of development. *Cement and Concrete Composites*, 19(2):107 – 122.